SISSA ISAS

SCUOLA INTERNAZIONALE SUPERIORE DI STUDI AVANZATI
INTERNATIONAL SCHOOL FOR ADVANCED STUDIES

Electronic properties driven by strong correlation

Thesis submitted for the degree of

Doctor Philosophiæ

Candidate:
Federico Becca

Supervisor:
Prof. Sandro Sorella

October 2000

Contents

Introduction **1**

1 The strongly correlated electron systems **9**
1.1 Introduction 9
1.2 Microscopic models 12
1.2.1 Phase separation 15
1.2.2 Superconductivity 18
1.2.3 Magnetic order 19

2 Numerical methods **21**
2.1 Lanczos 21
2.2 Variational Monte Carlo 24
2.2.1 Systematic improvement by Lanczos steps 26
2.3 Green function Monte Carlo 27
2.3.1 Basic principles 27
2.3.2 Statistical implementation of the power method 28
2.3.3 Fixed-node approximation 32
2.3.4 Forward walking technique 33
2.3.5 Green function Monte Carlo with stochastic reconfiguration . . 34
2.4 Few Lanczos steps from Monte Carlo technique 39
2.4.1 Variance extrapolation 43
2.4.2 Improving the variational energy 47

3 Phase separation **51**
3.1 Introduction 51
3.2 The Hubbard Model 53
3.2.1 Variational wavefunction 53
3.2.2 Results 56

3.2.3 Conclusions 62
3.3 The $t - J$ Model 62
3.3.1 Variational wavefunction 62
3.3.2 Results 66
3.3.3 Conclusions 72

4 Superconductivity and stripes in the $t - J$ model 73
4.1 Introduction 73
4.2 Small lattice calculations 77
4.3 Superconducting order parameter 81
4.4 Charge and spin modulations 87
4.5 Conclusions 93

5 Ferromagnetism from strong local repulsion 95
5.1 Introduction 95
5.2 Results 98
5.3 Conclusions 106

Conclusions 107

Acknowledgments 111

A Implementation of symmetries in the Lanczos algorithm 113

B An efficient calculation of the single Lanczos step 115

C Variance estimate of the error on bulk correlation functions 117

D An important property of the projected BCS wavefunction 119

Bibliography 123

Introduction

The fascinating subject of superconductivity was opened over a century ago by Onnes [1], but until quite recently it was strictly a low-temperature phenomenon. The discovery of the cuprate superconductors [2] in a family of transition metal oxides, with transition temperatures up to $T_c \sim 100K$, has generated tremendous excitement for two main reasons. First, from a practical point of view, these compounds open a new temperature realm for superconducting devices which may have interesting commercial applications, and these potential benefits have attracted extraordinary attention from the whole scientific community. The second reason, relevant to those in a more abstract field, is the interest in the microscopic mechanism driving superconductivity.

The first main distinction to be made is between theories which seek to describe these new materials within the framework of standard Eliashberg approach [3] or other weak coupling approaches arising from the exchange of other bosons, e.g. excitons or plasmons, and theories which make a radical break with the past and place these materials in the category of very strong coupling systems. It has become apparent from the early years of their discovery that many properties of these materials are unusual, and a proper understanding will require developing and extending concepts from many areas of condensed matter physics.

The main characteristic of the superconducting state is the opening of a gap at the Fermi level in the electronic spectrum. The difference with the conventional superconductors, where the gap opens isotropically along the Fermi surface, is that, for high-temperature superconductors, the gap has a strong dependence on the wavevector q, having a $d_{x^2-y^2}$ symmetry. Nevertheless, the superconducting state appears to be associated with a pairing of electrons, and hence the overall superconducting behavior of these new systems is similar to the one of the conventional materials. In fact most of the familiar phenomena which are manifestations of the superconducting state (persistent current, Josephson tunneling, vortex lattice) have been established also in these materials, but, the microscopic mechanism underlying the high transition temperature is still mysterious.

2 Introduction

There are theoretical problems connected not only with the high T_c and with the microscopic mechanism of superconductivity, but also with the many unconventional electronic properties observed above T_c, in the metallic state. The usual metals are well described by the Landau theory of the normal Fermi liquid [4]. Within this theory it is possible to view much of solid-state physics in terms of certain *elementary excitations*, which interact only weakly with one another. The use of an elementary excitation to describe the complicated interrelated motion of many particles has turned out to be an extraordinarily useful device in contemporary physics.

The remarkable fact is that, although the interactions between the electrons can be very strong and long-range (i.e. through the Coulomb potential), it is possible to describe the whole system with weakly interacting *quasi-particles*, with the same quantum numbers of the non-interacting gas of electrons. The Landau theory breaks down if there is a spontaneous symmetry breaking, e.g. if the gas of quasi-particles is unstable against superconductivity, antiferromagnetism or ferromagnetism. This case has been known for many years, and it is at the basis of the mechanism leading to the ordinary low-temperature superconductivity: if the net interaction between the quasi-particles is attractive in some angular momentum channel, it drives the system towards the superconducting state. Another, more interesting, way to break the Landau theory is when the residual interactions among quasi-particles are sufficiently strong that it is not possible to use a description of weakly interacting gas. This is the case of one-dimensional systems, where interactions lead to a decoupling between charge and spin excitations at low energy. However, in two or higher dimensions, singular (i.e. diverging) interactions at the Fermi surface are needed in order to break the Landau quasi-particle description [5].

The transition metal oxides represent prototype examples of materials in which the strong electron-electron and the strong electron-phonon interactions lead to phases with a very poor conductivity or even an insulating behavior, possibly leading to a Landau theory breaking. For example, $\mathrm{Ti_2O_3}$ and $\mathrm{VO_2}$ are dimerized insulating materials, $\mathrm{Ti_4O_7}$ and $\mathrm{V_4O_7}$ are charge ordered insulators, $\mathrm{CrO_2}$ is a ferromagnetic metal, MnO and NiO are Mott insulators with antiferromagnetic order. In this context the discovery of high-temperature superconductors by Bednorz and Müller in 1986 [2] has played the role of a sounding board for a renewed interest in this class of materials, opening a new era of unconventional superconductors. The cuprate superconductors are layered materials with a complex perovskite chemical structure. Copper-oxide planes $\mathrm{CuO_2}$ are alternated with insulating block layers of rare and/or alkaline earth and Oxygen atoms (see Fig. 1). At stoichiometric composition, the cuprates are insulators with antiferromagnetic order

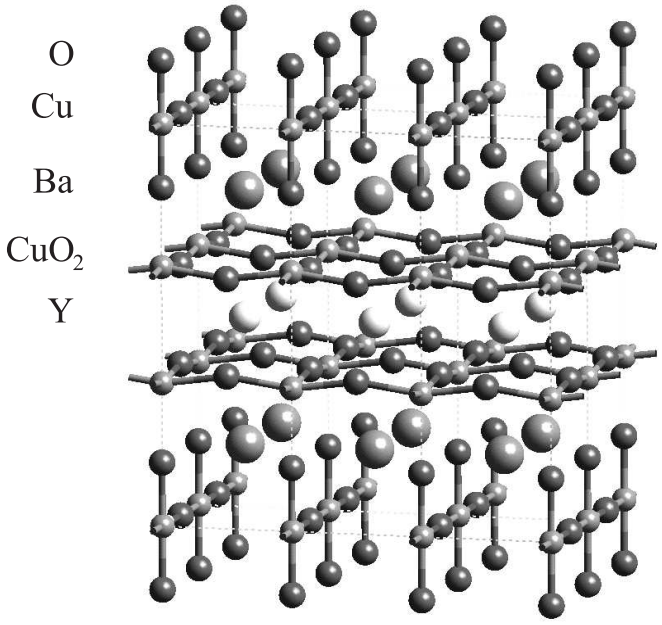

Figure 1: The structure of $\mathrm{YBa_2Cu_3O_7}$.

of the spin localized on the Copper atoms. The richness of the phase diagram of these materials depends upon the fact that the electron density can be varied by substituting the rare earths with lower valence elements or by adding Oxygen in the insulating block layers. Although the new atoms reside in between the $\mathrm{CuO_2}$ layers the free carriers are injected into the these layers. Hence, it is widely accepted that the $\mathrm{CuO_2}$ layers play a fundamental role in determining the physics of these materials. Detailed experiments reveal a strong dependence of the physical properties of the cuprates upon electron doping and temperature.

Two main features have particularly focused the attention of the scientific community in these years: the existence of a *pseudogap* phase in the underdoped region, in which the system does not have a superconducting long-range order, but there is a large anisotropic gap in the excitation spectrum [6, 7, 8], and the presence of huge charge and spin fluctuations, the so-called *stripes*, found at low temperature in many cuprates [9, 10]. One of the major challenges of high-temperature superconductors is to understand the nature of this anomalous phase above T_c and the relevance of the stripes with respect to the superconducting phase.

As suggested by Anderson in an early paper [11], strong *purely electronic* interaction combined with *low dimensionality* may entirely determine the physics of these systems. Following this suggestion, a huge amount of work has been done in order to understand and clarify how these two aspects change the usual properties of the elec-

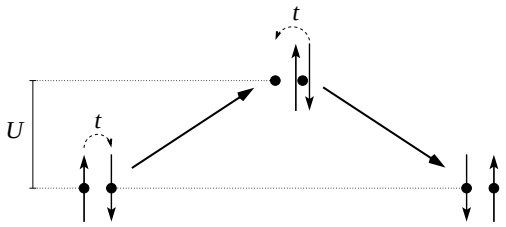

Figure 2: In second order perturbation theory in t/U, if the spins of neighboring sites are antiparallel, they gain energy by a virtual process creating a double occupation.

tron gas as predicted by simple mean-field treatments. Despite the intricate structure of the real materials, it is essential to reduce the problem as much as possible and identify the minimal features which can capture the relevant physics. In this regard, much attention has been devoted to effective low-energy models such as the Hubbard and the so-called $t-J$ model. The Hubbard model was introduced well before the discovery of high-temperature superconductors in order to describe the ferromagnetic properties of the transition metals [12]. In this simple model the complicated structure of the different bound and continuum energy levels of each ion, which corresponds to a lattice site, is reduced to a single localized orbital level. The states of the model are given by specifying the four possible configurations of each site, i.e. its level can be empty, contain one electron with either spin up or down, or be doubly occupied. The Hamiltonian contains only two terms: a diagonal term corresponding to a positive energy U times the number of doubly occupied ionic levels, and an off-diagonal term (nearest neighbor hopping) which has a non-vanishing matrix element t between those pairs of states that differ by the position of a single electron. In the strong coupling limit $U \gg t$, the low-energy states of the model belong to the subspace without doubly occupied sites. At lowest order in perturbation theory, the effective Hamiltonian, acting in the subspace without doubly occupied sites, contains, in addition to the hopping term, an antiferromagnetic coupling $J = \frac{4t^2}{U}$ between the spins of neighboring lattice sites (superexchange). Indeed, as sketched in Fig. 2, in second order perturbation theory, two opposite spins gain energy by virtual double occupation, whereas if the spins are parallel, the Pauli principle forbids this virtual process.

These simple models of strongly correlated electrons represent a training ground for studying how the charge and spin fluctuations may affect the nature of the ground-state. Indeed, it turns out that the strong interaction between electrons may drive the system towards different phases, e.g. superconducting, phase separated, stripe-like depending on the strength of the antiferromagnetic interaction and the level of doping.

Despite remarkable progress, we still lack reliable theoretical methods that work in

arbitrary dimension. In two dimensions in particular, even the seemingly simple goal of understanding the magnetic phase diagram of the Hubbard or the $t-J$ model is a challenge. Traditional mean-field techniques, slave-boson approaches [13] and dynamical mean-field theory [14] fail to give a satisfactory description of the phase diagram of strongly correlated electron systems in two dimensions. One of the main problems with these methods is the difficulty in handling the constraint of no double occupancy of the $t-J$ model.

Instead, quantum Monte Carlo techniques, allow us to overcome this difficulty and to treat exactly the constraint of the $t-J$ model. Moreover, by using quantum Monte Carlo it is possible to extract unbiased information about the ground-state properties of a generic correlated system in the whole parameter region. In its simplest formulation, the variational Monte Carlo, both the energy and the correlation functions of a given state can be calculated, by a stochastic sampling. In this case, the best representation of the true ground-state is given by the wavefunction with the lowest energy, but the results are strongly dependent on the chosen wavefunction, and therefore highly questionable. In the variational Monte Carlo scheme, the electronic configurations are sampled according to the square modulus of the given wavefunction, i.e. a positive definite quantity, which can be interpreted as a probability. This fact makes possible the usual Monte Carlo sampling, e.g. by using the Metropolis algorithm [15].

A systematic improvement of the variational Monte Carlo is given by stochastic methods which allow us to filter out, from a starting trial wavefunction, the ground-state, e.g. by the Green function Monte Carlo [16]. In this case the configurations are sampled according to the true ground-state wavefunction. Because of the antisymmetry of the many-body wavefunction, this quantity does not have a definite sign and cannot be interpreted as a probability distribution, and therefore these stochastic techniques cannot be straightforwardly applied. This is a particular case of the well-known sign problem, that affects all the quantum Monte Carlo methods for fermionic systems.

In order to overcome this difficulty, some approximate method is needed. The simplest one is the fixed-node [17], which allows us to obtain the best wavefunction in a class of states with their signs being fixed by the best variational one. This method relies on the choice of variational guess and therefore it contains an intrinsic bias. In this thesis we have also developed and made use of a recent improvement of the fixed-node approximation, the Green function with stochastic reconfiguration [18, 19], which allows us to release the fixed-node approximation in a controlled way and to obtain much more accurate estimates of the ground-state correlations.

On the other hand, whenever it is possible to improve systematically the variational

wavefunction and estimate its accuracy, the variational Monte Carlo calculation also assumes a powerful role in determining the ground-state properties of a many-body Hamiltonian. This can be done by applying a number p of Lanczos steps to a given starting wavefunction and by computing the energy and the variance of the resulting state. Since the ground-state has both the minimum energy and a zero variance, it is possible to use the p different results to estimate the exact zero-variance energy. It turns out that, whenever the variational wavefunction is a good approximation of the ground-state, few Lanczos steps are enough to determine a very accurate estimate of the ground-state energy and correlation functions. By using this method, we have shown that the projected d-wave superconducting wavefunction represents an exceptionally good variational state whenever the lattice does not break any spatial symmetry, namely for a two-dimensional square lattice, and we have obtained very accurate results for the energy and the superconducting order parameter of the $t-J$ model for $J = 0.4t$. This method gives reliable results in a large range of dopings and antiferromagnetic couplings J. Motivated by a renewed interest in the determination of the ferromagnetic stability in the $J = 0$ limit [20, 21, 22], we have found that the paramagnetic phase, stable at large hole doping δ, undergoes a second-order transition to a ferromagnetic state for $\delta \sim 0.4$.

By allowing few Lanczos steps, however, it is not possible to change drastically the nature of the wavefunction used as initial guess. For example, it is not possible to recover a charge/spin inhomogeneity, like phase separation or incommensurate charge/spin modulation, if the starting wavefunction has a homogeneous charge distribution. By contrast, within the fixed-node and the stochastic reconfiguration approaches, it is possible to change the structure of the wavefunction and recover a charge or spin modulation. It is worth noting that, at least within the fixed-node scheme, the charge and spin rearrangement is possible by changing only the amplitudes of the approximate ground-state wavefunction, without changing its relative phases. By calculating the density-density structure factor, we have given an accurate phase separation boundary for the Hubbard and the $t-J$ models.

Moreover, there is a strong and subtle dependence of the electron charge and spin distribution upon the shape of the lattice cluster. If rotational symmetry is broken by considering a rectangular cluster, the ground-state exhibits peaks in the density-density and spin-spin correlation functions, suggesting a charge and spin ordering. These results may explain the fact that a different numerical method, the density matrix renormalization group, applied to rectangular clusters with cylindrical boundary conditions, finds huge density modulations, whereas Monte Carlo techniques, with periodic boundary conditions leads to a homogeneous ground-state. The main feature which comes out

is that the $t - J$ model has a superconducting ground-state at moderate doping, but small perturbations in the underlying lattice, that induce some anisotropy in the original model, may drive the system towards a charge and spin inhomogeneity.

Chapter 1

The strongly correlated electron systems

1.1 Introduction

The discovery of high-temperature superconductors (HTSC) by Bednorz and Müller in 1986 [2] marked the beginning of the new era of the unconventional superconductors. Indeed Bednorz and Müller succeeded in finding superconductivity in a class of transition metal oxides, which are known to show a wide range of phase transitions driven by strong purely electronic and strong electron-phonon interactions. Hence, transition metal oxides range from antiferromagnetic insulators (NiO, Cr_2O_3) to ferromagnetic metals (CrO_2), and can show metal-insulator transitions (V_2O_3), spin pairing (Ti_2O_3) or charge ordering (V_4O_7, Ti_4O_7), see Fig. 1.1 [23]. Therefore, it soon became clear that the microscopic mechanism leading to high-temperature superconductivity has a completely different origin from the classic low-temperature superconductors, described by the BCS theory [24, 25]. The difference between these two kinds of superconductors is not restricted only to the value of the critical temperature T_c , but involves many aspects of their properties, both in the superconducting and in the metallic phase. Indeed, the basis of the BCS theory is the existence of a metallic Fermi-liquid at high temperatures [4]. Then, by decreasing the temperature, an attractive pairing interaction makes the metal unstable and drives the system towards a state in which the electrons are strongly bound in pairs. This scenario does not work for HTSC: indeed, through the years, it became clear that the phase above T_c cannot be described by a simple Fermi-liquid, in view of the many anomalous properties.

A common characteristic of the HTSC is the presence of CuO_2 layers; between these

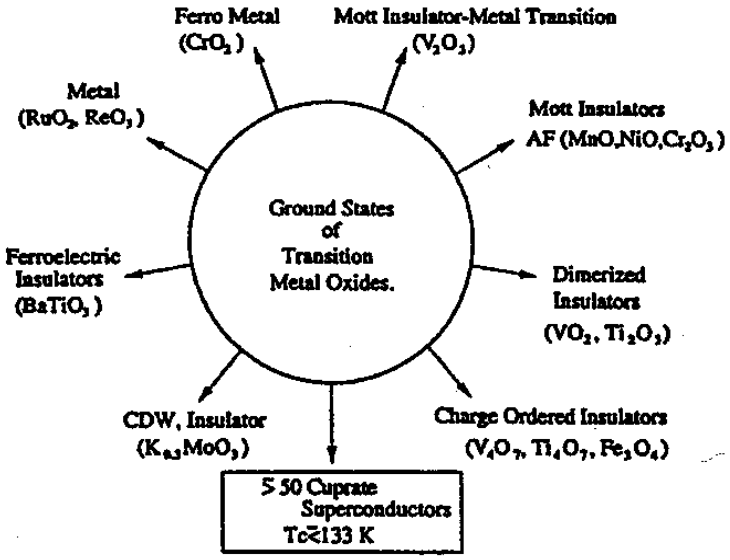

Figure 1.1: Phases of transition metal oxides, from Ref. [23].

layers there are charge *reservoirs* of rare-earth atoms like Lanthanum or Barium (see Fig. 1.2). In all the stoichiometric compounds, the Cu^{2+} ions have a magnetic moment and, below a Néel temperature, the undoped materials are insulating antiferromagnets with a charge-transfer gap, despite there being one hole per unit cell. This fact has led to the consideration of the strong electronic interaction as a fundamental ingredient: in particular, the local Coulomb interaction between two holes on a Copper atom is of the same magnitude as the bandwidth.

As the system is doped, the antiferromagnetic order is suppressed and the system eventually becomes superconducting (see Fig. 1.2). For example, in the case of La_2CuO_4, doping can be achieved in two different ways, either by substituting La^{3+} with Sr^{2+} or by inserting O^{2-}. Although the new atoms reside in the *reservoirs*, in both cases the free carriers (holes and electrons, respectively) are injected into the CuO_2 layers. This fact suggests that the CuO_2 planes have a fundamental role in determining the entire physics of HTSC.

The confirmation of the d-wave character of the superconducting gap [26], has definitely convinced that a purely phononic mechanism is not adequate to describe these materials and that superconductivity is caused by a different mechanism. Many authors have suggested theories that combine the pairing ideas with the presence of strong antiferromagnetic correlations. Among these there are the spin-bag theories [27], the nearly antiferromagnetic Fermi-liquid theories [28], and theories based on a self-consistent fluctuating exchange approximation [29].

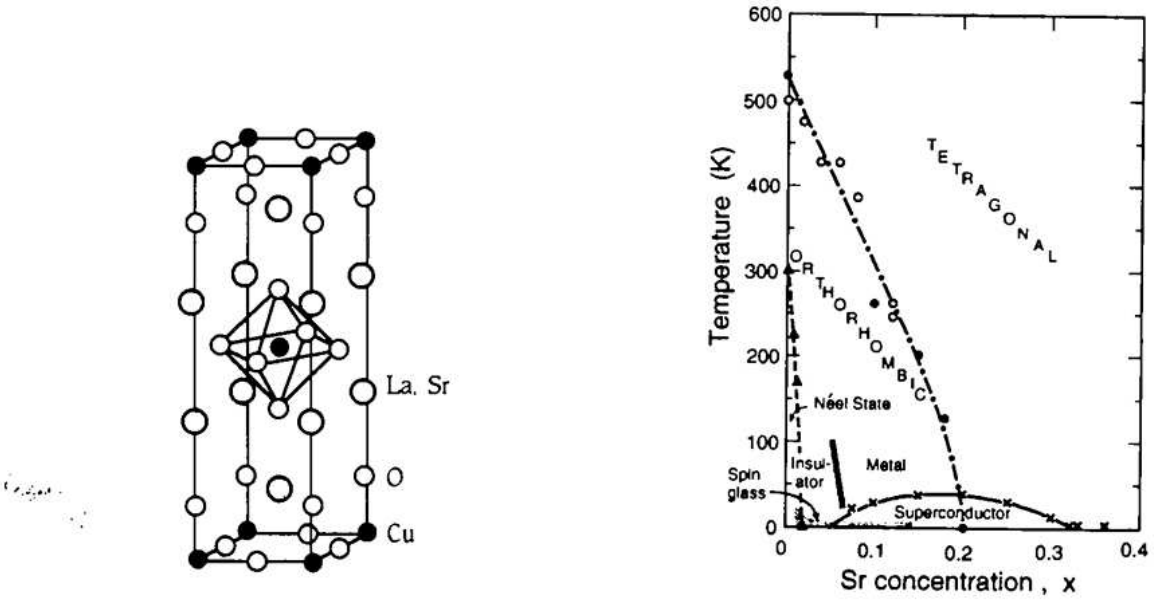

Figure 1.2: The structure of La_2CuO_4 and the phase diagram of $La_{2-x}Sr_xCuO_4$. The CuO_2 planes are believed to be the active region when additional holes are added by replacing some Lanthanum with Strontium.

A different point of view considers the superconductivity as caused by charge fluctuations [30, 31]. As pointed out first in Ref. [30], the strong electronic interaction between carriers can lead to phase separation, that is a state in which the mobile carriers cluster together, leaving the rest of the system undoped. This is what is experimentally observed for the Oxygen doped $La_2CuO_{4-\delta}$ [32]. In this compound the long-range Coulomb repulsion between charge carriers in the CuO_2 planes is screened by the mobile Oxygen atoms in the *reservoirs*. By contrast, in those compounds in which the long-range Coulomb repulsion is not screened, the long wavelength charge fluctuations are energetically unfavorable and only microscopic inhomogeneities are possible [30].

One of the most puzzling aspects of the HTSC is the anomalous behavior of the metallic state above the superconducting transition temperature. Both in the optimally doped region, where the critical temperature has the maximum value, and in the underdoped region, there is clear evidence that the metallic state cannot be described by the usual Fermi-liquid theory [4]. At optimal doping, the linear behavior of the resistivity from the critical temperature over a wide range of temperatures [33] has led many authors to claim that there is a breakdown of the Fermi-liquid theory in the normal state [34]. In the underdoped regime, below a crossover temperature T^* the cuprates are characterized by the opening of a large *pseudogap* in the single-particle excitation spectrum

and in the spin and charge response function, as observed in angle resolved photoemission, tunneling and specific heat [35]. Although in this state there is a gap, of $d_{x^2-y^2}$ symmetry, there is no long-range order [7, 8].

On the other hand, one of the longstanding mysteries of HTSC concerns the suppression of superconductivity in $\mathrm{La_{2-x}Ba_xCuO_4}$ at $\mathrm{x} = \frac{1}{8}$ [36]. Different studies [9, 37, 38, 39] of this and related cuprates materials, such as $\mathrm{La_{1.6-x}Nd_{0.4}Sr_xCuO_4}$, have established that the suppression of T_c requires both a hole concentration of $\mathrm{x} = \frac{1}{8}$ and a lattice distortion from the usual low-temperature orthorhombic to the low-temperature tetragonal structure. Furthermore, at the same doping, neutron studies have found a clear evidence of static incommensurate ordering of antiferromagnetic stripes separated by charged domain walls [9, 39]. The presence of dynamic incommensurate spin and charge fluctuations is well established also for other hole densities and different compounds [40, 41]. The understanding of the role of these inhomogeneities remains a challenging unsolved problem.

Definitely, the discovery of HTSC has given a great impetus to clarifying old issues and to investigating new possible phases in solid state physics. Indeed, HTSC has been the starting point for studying different problems such as the metal-insulator transition, the breakdown of the Fermi-liquid theory, charge and spin order in solids. Moreover, in the last few years it has become evident that many different materials, such as manganites [42], fullerides [43], organic conductors [44], cannot be described by standard theories and electron-electron correlations play a crucial role in determining their physics.

In this regard, simple microscopic models of strongly correlated electrons represent a very useful training ground to understand the fundamental physics of the much more complicated real materials.

1.2 Microscopic models

The simplest model of interacting electrons on a lattice is the Hubbard Hamiltonian [12]

$$H = -t \sum_{\langle i,j \rangle, \sigma} c^{\dagger}_{i,\sigma} c_{j,\sigma} + U \sum_{i} n_{i,\uparrow} n_{i,\downarrow}, \tag{1.1}$$

where $\langle\ \rangle$ stands for nearest neighbors, $c_{i,\sigma}$ ($c^{\dagger}_{i,\sigma}$) destroys (creates) an electron with spin σ at site i, and $n_{i,\sigma} = c^{\dagger}_{i,\sigma} c_{i,\sigma}$. Each site can be empty, singly occupied, by an electron with spin up or down, or doubly occupied. Electrons can hop from a site to the neighboring one with an amplitude $-t$. The interaction between particles is reduced to a local density-density term, while all the non-local terms are dropped.

A more realistic model for describing the $\mathrm{CuO_2}$ layers is the three-band Hubbard model

$$\begin{aligned} H &= \epsilon_d \sum_{i\sigma} d^\dagger_{i,\sigma} d_{i,\sigma} + \epsilon_p \sum_{l\sigma} p^\dagger_{l,\sigma} p_{l,\sigma} + U_d \sum_i d^\dagger_{i,\uparrow} d_{i,\uparrow} d^\dagger_{i,\downarrow} d_{i,\downarrow} \\ &+ U_p \sum_l p^\dagger_{l,\uparrow} p_{l,\uparrow} p^\dagger_{l,\downarrow} p_{l,\downarrow} + U_{pd} \sum_{\langle i,l\rangle\sigma,\sigma\prime} d^\dagger_{i,\sigma} d_{i,\sigma} p^\dagger_{l,\sigma\prime} p_{l,\sigma\prime} \\ &- t_{pd} \sum_{\langle i,l\rangle\sigma} d^\dagger_{i,\sigma} p_{l,\sigma} + H.c., \end{aligned} \tag{1.2}$$

where $d^\dagger_{i,\sigma}$ creates a $\mathrm{Cu}(3d_{x^2-y^2})$ hole with spin σ at Copper site i, $p^\dagger_{l,\sigma}$ creates an $\mathrm{O}(2p_x)$, or $\mathrm{O}(2p_y)$, hole with spin σ at Oxygen site l, ϵ_d and ϵ_p are the atomic energies of Copper and Oxygen respectively, and $\Delta_{pd} = \epsilon_p - \epsilon_d > 0$. U_d and U_p are the local Coulomb repulsion on Copper and Oxygen atoms, U_{pd} is the Coulomb interaction between nearest neighbor Copper and Oxygen atoms. Finally, t_{pd} is the $\mathrm{Cu-O}$ hybridization, and the last sum runs over the four Oxygen atoms around the Copper site i.

Although the Hubbard model (1.1) is certainly a very simple Hamiltonian of interacting electrons on a lattice, there are no exact solutions for spatial dimensions greater than one [45], and even at zero temperature the ground-state properties as a function of the interaction strength U and the electron density are not known. In Fig. 1.3 we report the Hartree-Fock phase diagram of the two-dimensional Hubbard model as calculated in Ref. [46]. Although the Hartree-Fock approximation gives a presumably reasonable description of the true ground-state only in the weak-coupling limit, this approach can give important insights into the competing phases, e.g. metallic, or with spin or charge order.

Furthermore, the most intriguing problem in strongly correlated electron models is the possibility of having superconductivity from a purely repulsive interaction. The nature and the extent of the pairing correlations in the two-dimensional Hubbard model near half-filling remains an open question. Diagrammatic calculations based upon the exchange of spin fluctuations [28, 29] suggest the possibility of d-wave pairing. Within quantum Monte Carlo calculations it turns out that the superconducting correlations are suppressed by increasing the electron interaction both in the single-band [47] and in the three-band Hubbard models [48]. On the other hand, within a renormalization group approach [49], a $d_{x^2-y^2}$ superconducting ground-state at infinitely small coupling and finite doping has been recently obtained.

In the strong coupling regime, i.e. $U \gg t$, the Hubbard model can be mapped onto

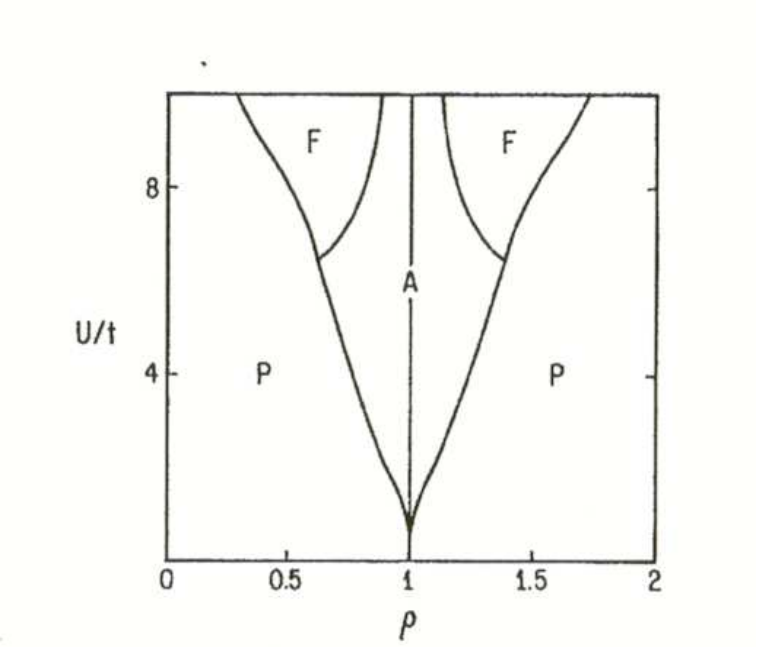

Figure 1.3: Hartree-Fock phase diagram for the two-dimensional Hubbard model from Ref. [46], ρ is the electron density. A, F, and P denote antiferromagnetic, ferromagnetic, and paramagnetic ground-states, respectively.

the so-called $t-J$ model, projecting out the subspace with doubly occupied sites

$$H = -t \sum_{\langle i,j\rangle,\sigma} \tilde{c}^{\dagger}_{i,\sigma} \tilde{c}_{j,\sigma} + J \sum_{\langle i,j\rangle} \left(\mathbf{S}_i \cdot \mathbf{S}_j - \frac{1}{4} n_i n_j \right) \tag{1.3}$$

where $\tilde{c}^{\dagger}_{i,\sigma} = c^{\dagger}_{i,\sigma}(1 - n_{i,\bar{\sigma}})$, $n_i = \sum_{\sigma} n_{i,\sigma}$ is the electron density on site i, $\mathbf{S}_i = \sum_{\sigma,\sigma'} \tilde{c}^{\dagger}_{i,\sigma} \tau_{\sigma,\sigma'} \tilde{c}_{i,\sigma'}$ is the spin operator and $\tau_{\sigma,\sigma'}$ are Pauli matrices. The antiferromagnetic coupling J is related to the Coulomb interaction by $J = 4t^2/U$ [50].

The relevance of this model for HTSC is given by the fact that also the more realistic three-band Hubbard model (1.2) reduces to the $t-J$ model for large on-site Copper repulsion $U_d \gg t_{pd}, \Delta_{pd}, U_p, U_{pd}$ [51], although in this case the expression for J is more complicated

$$J = \frac{4t_{pd}^4}{(\Delta_{pd} + U_{pd})^2} \left[\frac{1}{U_d} + \frac{2}{2\Delta_{pd} + U_p} \right]. \tag{1.4}$$

Using the realistic values for the parameters [52], it is found that $J \sim 0.2 \div 0.6t$.

At half-filling, that is when the number of electrons equals the number of sites, the charge dynamics is completely frozen and only the spin degrees of freedom are effective, in this case the $t-J$ model is equivalent to the Heisenberg model. Although we lack the exact solution of the Heisenberg model for dimensions greater than one, it is well accepted that, in two dimensions, the ground-state is magnetically ordered and has a

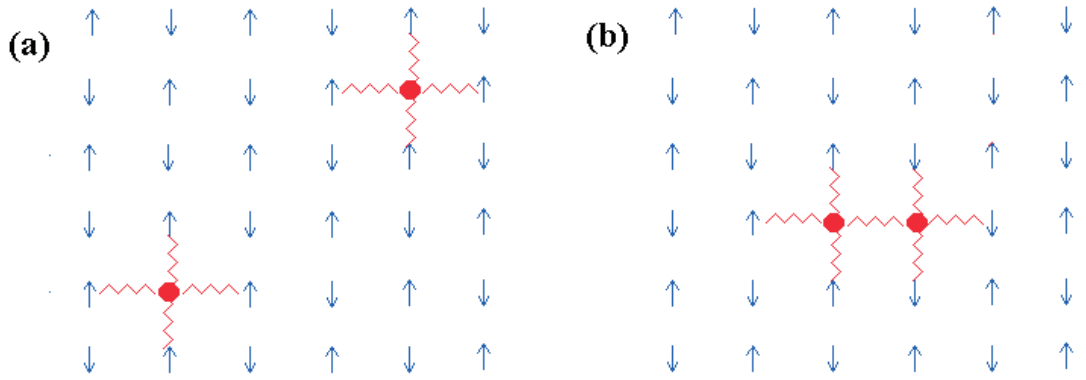

Figure 1.4: Two holes in an antiferromagnetic background. In the $J \gg t$ limit, the energy loss with respect to the ordered state is given by number of broken bonds. If the holes are far apart (a) the energy loss is $8BJ$ whereas if they form a cluster (b) it is $7BJ$.

finite staggered magnetization in the thermodynamic limit [16, 53]. This fact strongly suggests that, at least at half-filling, the cuprates are well described by this Hamiltonian. The crucial point for HTSC is whether the underdoped regime can be described by doping the Heisenberg model, that is by the $t-J$ model.

1.2.1 Phase separation

Recently, the problem of a finite number of holes in an antiferromagnetic background has attracted considerable attention. At finite hole doping there is competition between the kinetic energy, which favors a homogeneous delocalized state, and the interaction energy, which favors an inhomogeneous localized state. This competition may give rise to strong charge fluctuations and eventually to phase separation or charge density waves.

In order to gain insight into the possible charge inhomogeneities in the lightly doped $t-J$ model, it is instructive to consider the case of two holes and $J \gg t$. In this limit the kinetic energy can be neglected, and the energy of a state with two widely separated holes is $E = E_0 - 8BJ$, where E_0 is the energy of the uniform antiferromagnetic background and B is the antiferromagnetic energy per bond. By contrast the energy of a state with the two holes clustered together to form a pair is $E = E_0 - 7BJ$ (see Fig. 1.4). The same argument holds for a finite number of holes.

This simple variational calculation suggests that, at least for very large values of J, the state in which the holes are segregated, leaving the rest of the system undoped, is favored over the uniform one. At finite t the loss in antiferromagnetic energy competes with the gain in kinetic energy, and it is not at all obvious if the homogeneous state is

unfavorite.

In an early work, Emery and co-workers [54] claimed that, at low doping, the ground-state of the $t-J$ model is phase-separated for all the interaction strength J. Their statement was supported by an exact diagonalization on a small lattice cluster and by a variational calculation for $J \ll t$. Although the exact diagonalization results give insights into the physical properties of the cluster under consideration, for fermion systems it is impossible to consider sizes with more than $16-32$ sites and, for such small lattices, any size scaling in more than one dimension is highly questionable. Since the phase separation is a long-wavelength instability it is crucial to consider large systems. Moreover, on small lattices and for low doping it is not easy to distinguish between phase separation and pairing. For example, for a 16-sites lattice, the clustering of two holes can represent both pairing or phase separation at a doping of $\delta \sim 0.12$.

In the thermodynamic limit, the compressibility of a stable system is finite and positive. Since the compressibility can be related to the second derivative of the energy per site $e(\delta)$ with respect to the density δ

$$\chi = \left(\frac{\partial^2 e}{\partial \delta^2} \right)^{-1}, \tag{1.5}$$

it turns out that, in an infinite system, the stability criterium requires that the energy per site is a concave function of the density, see Fig. 1.5 (a). By contrast, if the compressibility is negative, the system phase-separates, i.e. it creates two macroscopic regions with densities δ_{c_1} and δ_{c_2}. In this case, the energy of the homogeneous state can be lowered by forming two separated regions with different densities, being the total energy given by the Maxwell construction, see Fig. 1.5 (b).

In Ref. [54], a very clever way to detect phase separation by using energy calculations has also been suggested. Assuming that, at a fixed hole doping δ, the system is composed of a hole-free and a hole-rich phase, with density x, and assuming that the volume is large enough that the surface interaction can be neglected, the energy per site can be written in the form

$$e(\delta) = \min_x e(\delta, x) = \min_x \left\{ \left(1 - \frac{L_x}{L} \right) e_0 + \frac{L_x}{L} e_x \right\}, \tag{1.6}$$

where L is the total number of sites, L_x is the number of sites in the hole-rich phase, e_0 is the energy per site of the Heisenberg (hole-free) phase, and e_x is the energy per site of the uniform hole-rich phase, which is a function of $x = N_h/L_x$, with N_h number of holes, finally the hole density of the total system is $\delta = N_h/L$. For fixed values of N_h and L, i.e. for a given doping δ, $e(\delta, x)$ is a function of L_x. The system phase-separates

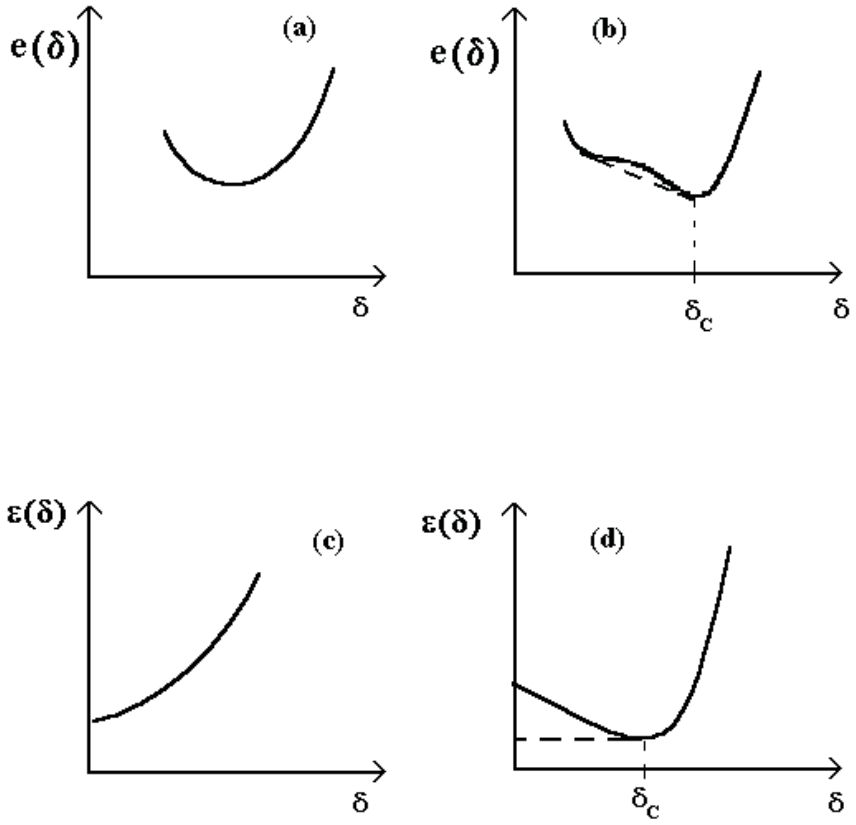

Figure 1.5: Energy per site landscape versus doping for a stable (a) and a phase-separated (b) system. Energy per per hole versus doping for a stable (c) and unstable (d) system. The dashed line is the Maxwell construction.

if $e(\delta, x)$ has a minimum as a function of L_x at $L_x < L$. The energy per site can be rearranged into the form

$$e(\delta, x) = e_0 + \delta\epsilon(x), \tag{1.7}$$

where

$$\epsilon(x) = \frac{e_x - e_0}{x} \tag{1.8}$$

is the energy per hole in the (uniform) hole-rich region. Therefore phase separation occurs if $\epsilon(x)$ has a minimum at finite x, see Fig. 1.5 (c) and (d). It is worth noting that, in the thermodynamic limit, if the system phase-separates, $\epsilon(x)$ is a flat function of x for $0 < x < \delta_c$, whereas, in a finite size lattice, due to surface terms, $\epsilon(x)$ can be slightly convex.

By using the above mentioned method, different authors have addressed the problem of finding out the critical value J_c above which there is phase separation at low doping in

the $t-J$ model by using different numerical techniques [55, 56, 57, 58, 59, 60, 61, 62, 63]. It is worth noting that because the Hubbard model reduces to the $t-J$ one in the strong coupling limit, one could expect that, if the $t-J$ model phase-separates at small J's, the Hubbard model will also at large U's. Although there is no general consensus on the value of J_c, most of the calculations agree that it is between $0.5t$ and $1.2t$. Different quantum Monte Carlo calculations [57, 58, 59, 60] agree with a $J_c \sim 0.5t$, by contrast in Refs. [61, 62] it is found that there is phase separation at all the interaction strengths. These discrepancies are probably due to the fact that in the latter work the different dopings are not achieved by varying the number of holes while keeping the lattice size constant, but by varying the lattice size while keeping the number of holes constant. Although this procedure probably overcomes the problems of having shell effects, it forces one to use fairly small sizes in the delicate low-doping region.

The high-temperature expansion [55, 56] gives $J_c \sim 1.2t$, but this method suffers from the difficulty of extrapolating the ground-state energy from very high temperatures. Finally a recent density matrix renormalization group calculation [63] gives $J_c \sim t$. This value is found by calculating the critical value for N-leg ladders with increasing number of legs (up to $N=6$) and extrapolating to the two-dimensional limit.

1.2.2 Superconductivity

Many of the methods that have been used in establishing results on charge or spin order have not been able to provide clear and definite evidence for or against superconductivity. The main problem of quantum Monte Carlo techniques is that the sign problem prevents us from reaching low enough temperatures to show a clear superconducting signal [64, 65, 66]. Within the high-temperature expansion it is not clear whether series of high enough order can be calculated to reach a temperature below which a signal of superconductivity would be observed. As far as the exact diagonalization methods are concerned, Dagotto and Riera [67] found a strongly enhanced pair-pair structure factor in a 4×4 cluster at quarter filling for $J \sim 3t$. Their results indicate that the symmetry of the order parameter is $d_{x^2-y^2}$. However the 4×4 system is still quite small and this signal may be due to short-range correlations instead of true off-diagonal long-range order.

Insights in favor of superconductivity come from variational results. Although variational calculations are limited by the small number of wavefunctions one can choose, they nevertheless provide useful information about the ground-state properties and they give a good starting point for further investigations. The work is especially hard in the

$t-J$ model, where many different magnetic and charge-ordered phases are competing. Indeed, from variational calculations it becomes clear that in the low-doping region antiferromagnetic ordered phases are competing with superconductivity, the two phases having very similar energies. Moreover it is not clear if it is possible to have a coexistence of these two phases or if they are exclusive.

Gros [68] suggested that the $d_{x^2-y^2}$ BCS wavefunction projected onto the subspace of no doubly occupied sites is a very good variational state for the $t-J$ model. Moreover, Giamarchi and Lhuillier [69] found the d-wave state stable up to $\delta \sim 0.4$.

More recently, different more involved techniques have been used to improve the variational state by using few Lanczos steps [70], or the fixed-node approximation [17] on the lattice. The former approach has given controversial results. Shih and co-workers [71] have shown that the pair-pair structure factor is suppressed and they argued that there is no superconducting order for $J \lesssim 0.7t$. Conversely, Heeb and Rice [58] identify a finite region of d-wave superconductivity for hole densities down to $\delta \sim 0.16$.

Calandra and Sorella [72] have suggested that, instead of calculating the long-range pair-pair correlations, in Monte Carlo methods a more reliable and less biased quantity is the short-range superconducting order parameter. Indeed it is found that by increasing the accuracy of the calculation, the order parameter remains finite and sizeable for $J = 0.4t$ and $\delta \sim 0.13$.

The density matrix renormalization group calculations present a completely different scenario. Using a rectangular cluster with open boundary condition in one direction, it is found that the ground-state has a huge charge modulation and that the superconducting pair-pair correlations are almost negligible [73].

As far as the Hubbard model is concerned, a superconducting instability, with a maximal $T_c \sim 150K$ at $\delta \sim 0.2$, has been found for $U = 12t$ within the dynamical cluster approximation [74]. Moreover a wide region of coexistence of antiferromagnetism and superconductivity comes out at $U \sim 5t$ from a slightly different approach [75]. Finally, a weak-coupling renormalization group approach [49] also gives rise to a d-wave order parameter in a large region of the phase diagram of the Hubbard model. These results are in strong disagreement with what is found in quantum Monte Carlo calculations [47], where no sign of superconducting correlations is detected.

1.2.3 Magnetic order

At half-filling both the $t-J$ and the Hubbard model are antiferromagnetic insulators. The $t-J$ model reduces to the Heisenberg model, and due to the constraint of no doubly

occupied sites, only the spin exchange interaction is relevant. By contrast in the Hubbard model there are both charge and spin fluctuations, but at half-filling, because of the completely nested Fermi surface, the ground-state is an insulator antiferromagnetically ordered at any finite interaction U. At finite doping, the hole hopping highly frustrates the antiferromagnetic background, leading to the suppression of the long-range order. This has been verified in the $t-J$ model by Variational Monte Carlo [69, 76] which found a rapid suppression of antiferromagnetism with doping, and by high-temperature expansion [77] which found a sharp antiferromagnetic peak in the spin-spin structure factor at $Q = (\pi, \pi)$ at half-filling, which is present but suppressed by increasing the doping. Moreover, in the low-doping region of the Hubbard model it has been found by using the Hartree-Fock approximation that the commensurate antiferromagnetic state is unstable against domain-wall formation [78], and by Monte Carlo calculations that the spin-spin structure factor develops incommensurate peaks at wavevectors near Q [79].

Another type of magnetic order, not related to cuprates, is the ferromagnetic instability, that may occur at low doping and small coupling, i.e. $J \ll t$. In particular, one of the few rigorous theorems in strongly correlated systems refers to one hole in the $J = 0$ limit [80]. In this case, Nagaoka showed that the ground-state is fully polarized, that is it has all the spins aligned. Although the Nagaoka theorem holds at any finite size and in the thermodynamic limit, there are no generalizations at finite hole densities. Indeed, the case of one hole is not relevant for infinite size and can only be a "singular point".

The question of ferromagnetism in the infinite-U Hubbard model (or equivalently the $J = 0$ case of the $t-J$ model) has attracted much interest in the past years [20, 21, 22, 81, 82, 83, 84]. In particular, it has become clear that, at least for small sizes, there are huge boundary effects that affect the result [84]. Extrapolating series of few coefficients, the high-temperature expansion gives an energy much lower than the ferromagnetic one, suggesting that at any finite hole doping the ground-state is not fully polarized. It is worth noting that the high-temperature expansion is not a variational method and extrapolation from high temperature down to zero temperature is highly non trivial. By contrast, pure variational calculations [21, 22], which are based on a single spin-flip on the ferromagnetic state, give a finite critical hole density below which the ground-state is fully polarized.

Chapter 2

Numerical methods

2.1 Lanczos

From a general point of view, the ground state $|\Phi_0\rangle$ of an Hamiltonian H can be obtained by the *power method* from a trial wavefunction $|\Psi_T\rangle$, provided that $\langle\Psi_T|\Phi_0\rangle \neq 0$. Indeed, if we define the operator $G = \Lambda - H$, with Λ a suitable constant chosen to allow us the convergence to the ground-state, we have that:

$$G^n|\Psi_T\rangle = (\Lambda - E_0)^n \left\{ a_0|\Phi_0\rangle + \sum_{i\neq 0} \left(\frac{\Lambda - E_i}{\Lambda - E_0}\right)^n a_i|\Phi_i\rangle \right\}, \tag{2.1}$$

where E_i and $|\Phi_i\rangle$ are the eigenvalues and eigenvectors of H respectively, and $a_i = \langle\Phi_i|\Psi_T\rangle$. Therefore

$$\lim_{n\to\infty} G^n|\Psi_T\rangle \sim |\Phi_0\rangle, \tag{2.2}$$

that is, as n goes to infinity, the iteration converges to the ground-state of the Hamiltonian H.

Starting from the power method, it is possible to define a much more efficient iterative procedure for the determination of the lowest eigenstate of Hermitian matrices, known as the Lanczos technique. Indeed, within the power method, the ground-state is approximated by a single state, i.e. $|\Phi_0\rangle \sim G^n|\Psi_T\rangle$, by contrast, the basic idea of the Lanczos method, is to use all the information contained in the powers $G^i|\Psi_T\rangle$, with $i = 1, \ldots, n$ to reconstruct the ground-state $|\Phi_0\rangle$, namely

$$|\Phi_0\rangle \sim \sum_{i=1,\ldots,n} \alpha_i H^i|\Psi\rangle. \tag{2.3}$$

However, the vectors generated by the power method are not orthogonal, whereas within the Lanczos method a special orthogonal basis is constructed. This basis is generated

iteratively. The first step is to choose an arbitrary vector $|\Psi_1\rangle$ of the Hilbert space, the only requirement is that this vector has a non-zero overlap with the true ground-state. If there is no *a priori* information about the ground-state, this requirement is satisfied by selecting random coefficients in the working basis. If some information about the ground-state is known, like its momentum, spin, or its properties under rotation, then it is useful to initialize the starting vector using these properties, choosing a vector that belongs to the particular subspace having the right quantum numbers.

The Lanczos procedure consists in generating a set of orthogonal vectors as follow: we normalize $|\Psi_1\rangle$ and define a new vector by applying the Hamiltonian H to the initial state, and we subtract the projection over $|\Psi_1\rangle$

$$\beta_2|\Psi_2\rangle = H|\Psi_1\rangle - \alpha_1|\Psi_1\rangle, \tag{2.4}$$

the coefficients α_1 and β_2 are such that $\langle\Psi_2|\Psi_2\rangle = 1$ and $\langle\Psi_1|\Psi_2\rangle = 0$, that is:

$$\alpha_1 = \langle\Psi_1|H|\Psi_1\rangle \tag{2.5}$$
$$\beta_2 = \langle\Psi_2|H|\Psi_1\rangle. \tag{2.6}$$

Then we can construct a new state, orthogonal to the previous ones as

$$\beta_3|\Psi_3\rangle = H|\Psi_2\rangle - \alpha_2|\Psi_2\rangle - \beta_2|\Psi_1\rangle, \tag{2.7}$$

with

$$\alpha_2 = \langle\Psi_2|H|\Psi_2\rangle \tag{2.8}$$
$$\beta_3 = \langle\Psi_3|H|\Psi_2\rangle. \tag{2.9}$$

In general the procedure can be generalized by defining an orthogonal basis recursively as

$$\beta_{n+1}|\Psi_{n+1}\rangle = H|\Psi_n\rangle - \alpha_n|\Psi_n\rangle - \beta_n|\Psi_{n-1}\rangle, \tag{2.10}$$

for $n = 1, 2, 3, \ldots$, being $|\Psi_0\rangle = 0$, $\beta_1 = 0$ and

$$\alpha_n = \langle\Psi_n|H|\Psi_n\rangle \tag{2.11}$$
$$\beta_{n+1} = \langle\Psi_{n+1}|H|\Psi_n\rangle. \tag{2.12}$$

It is worth noting that, by construction, the vector $|\Psi_n\rangle$ is orthogonal to all the previous ones, although we subtract only the projections of the last two. In this basis the

Hamiltonian has a tridiagonal form

$$H = \begin{pmatrix} \alpha_1 & \beta_2 & 0 & 0 & \dots \\ \beta_2 & \alpha_2 & \beta_3 & 0 & \dots \\ 0 & \beta_3 & \alpha_3 & \beta_4 & \dots \\ 0 & 0 & \beta_4 & \alpha_4 & \dots \\ \dots & \dots & \dots & \dots & \dots \end{pmatrix} . \tag{2.13}$$

Once in this form, the matrix can be easily diagonalized by using standard library subroutines. In principle, in order to obtain the exact ground-state of the Hamiltonian, it is necessary to perform a number of iterations equal to the dimension of the Hilbert space. In practice, the greatest advantage of this method is that a very accurate approximation of the ground-state is obtained after a very small number of iterations, typically of the order of 100, depending on the model.

The main limitation of this technique is the exponential growing of the Hilbert space. Indeed, although the ground-state can be written with a great accuracy in terms of few $|\Psi_n\rangle$ as

$$|\Phi_0\rangle \simeq \sum_{n=1}^{\sim 100} c_n |\Psi_n\rangle, \tag{2.14}$$

it is necessary to express the general vector of the Lanczos basis $|\Psi_n\rangle$ in a suitable basis to which the Hamiltonian is applied. For example, for the spin-$\frac{1}{2}$ Heisenberg model, in which each site can have an up or a down spin, it is convenient to work in the Ising basis, where S_z is defined at every site, i.e. a generic element is given by $|x\rangle = |\uparrow, \downarrow, \downarrow, \uparrow, \downarrow, \uparrow, \uparrow, \downarrow, \dots\rangle$. For the Hubbard model, each site can be singly occupied, by a spin up or down, doubly occupied by opposite spins or empty, and the generic element reads $|x\rangle = |\uparrow, 0, \uparrow\downarrow, \downarrow, 0, 0, \uparrow\downarrow, \uparrow, \dots\rangle$. For the Hubbard model on 16 sites at half-filling and $S_z = 0$ the Hilbert space is about 165×10^6, a huge computer memory. In practice this problem can be heavily alleviated by using the symmetries of the Hamiltonian (in Appendix A it is shown how to implement symmetries in the Lanczos algorithm). Indeed, in the case of periodic boundary conditions, there is translational invariance and the total momentum of the system is a conserved quantity. Moreover, on square lattices also discrete rotations of $\pi/2$ and reflections with respect to a particular axis are defined and can give rise to good quantum numbers.

Since in general translations and rotations do not commute, it is not possible to diagonalize the Hamiltonian in a subspace with a definite momentum and a definite symmetry with respect to rotations. However, for particular values of the momentum it is possible to define also the rotational quantum number. For example, for $k = (0, 0)$ or

$k = (\pi, \pi)$ the Hamiltonian has a block-form also with respect to rotations. After the introduction of these symmetries, the Hilbert space of the Hubbard model at half-filling, $S_z = 0$, zero momentum and s-wave is about 1.3×10^6. Therefore it comes out that the use of the symmetries is a fundamental achievement to perform a diagonalization of the Hubbard model, at least near half-filling.

In principle the Lanczos procedure, as described in Eqs. (2.10), (2.11) and (2.12), can give informations about both the ground-state energy and the ground-state vector. In practice, during the Lanczos matrix construction, only three vectors are stored, i.e. $|\Psi_{n+1}\rangle$, $|\Psi_n\rangle$ and $|\Psi_{n-1}\rangle$ (by using an improved algorithm, it is possible to store only two vectors), because each element $|\Psi_n\rangle$ of the basis is represented by a large set of coefficients, when it is expanded in the basis selected to carry out the problem. Therefore, it is not convenient to store all the $|\Psi_n\rangle$ vectors individually, since this procedure would demand a memory requirement equal to the size of the Hilbert space times the number of Lanczos steps. A possible solution of the problem is to run the Lanczos twice: in the first run we find the coefficient c_n of Eq. (2.14), in the second run the vectors $|\Psi_n\rangle$ are systematically reconstructed one by one, multiplied by their coefficient and stored in $|\Phi_0\rangle$.

Within the Lanczos method, it is useful to consider not only the $N \times N$ cluster, but also other tilted square lattices, which have axes forming non-zero angles with lattice axes. In general it is possible to construct square cluster with $L = l^2 + m^2$, being l and m positive integers. Only cluster with $l = 0$ (or $m = 0$) or $l = m$ have all the symmetries of the infinite lattice, clusters with $n \neq m$ can have rotations but not reflections with respect to a given axis.

In this thesis, using all the lattice symmetries, we have diagonalized the Hubbard model on 18 sites, where the symmetrized Hilbert space at half-filling and $S_z = 0$ is about 16×10^6 [85]. By contrast, due to the smaller bare Hilbert space, the $t - J$ model can be diagonalized in rather bigger cluster, i.e. for 4 holes on 26, where the symmetrized Hilbert space is about 50×10^6.

2.2 Variational Monte Carlo

One of the most useful properties of quantum mechanics is that the expectation value of an Hamiltonian H over any trial wavefunction $|\Psi\rangle$ gives an upper bound to the ground-state energy E_0

$$E = \frac{\langle\Psi|H|\Psi\rangle}{\langle\Psi|\Psi\rangle} \geq E_0, \tag{2.15}$$

this can be easily seen if we expand $|\Psi\rangle$ in terms of the eigenfunction $|\Phi_i\rangle$ of H with energy E_i

$$\frac{\langle\Psi|H|\Psi\rangle}{\langle\Psi|\Psi\rangle} = \sum_i E_i \frac{|\langle\Phi_i|\Psi\rangle|^2}{\langle\Psi|\Psi\rangle} = E_0 + \sum_i (E_i - E_0)\frac{|\langle\Phi_i|\Psi\rangle|^2}{\langle\Psi|\Psi\rangle} \geq E_0 . \tag{2.16}$$

In this way, if we have a set of different wavefunctions, we can choose the best approximation of the ground-state by looking for the lowest expectation value of the energy.

In general, due to the rapid growth of the Hilbert space with the lattice size, the variational expectation values (2.15) can be calculated exactly only for very small clusters, e.g. about 40 sites for the spin-$\frac{1}{2}$ Heisenberg model. On larger sizes only a Monte Carlo approach to evaluate Eq. (2.15) is possible. In order to show how statistical methods can be used to calculate this kind of expectation values, it is useful to introduce complete sets of states $|x\rangle$ in Eq. (2.15)

$$\frac{\langle\Psi|H|\Psi\rangle}{\langle\Psi|\Psi\rangle} = \frac{\sum_{x,x'} \Psi(x') H_{x',x} \Psi(x)}{\sum_x \Psi^2(x)}, \tag{2.17}$$

where $\Psi(x) = \langle x|\Psi\rangle$, $H_{x',x} = \langle x'|H|x\rangle$, and for the sake of simplicity we have restricted to real wavefunctions. Defining the *local energy* E_x as

$$E_x = \frac{\langle x'|H|\Psi\rangle}{\langle x|\Psi\rangle} = \sum_{x'} \frac{\Psi(x')}{\Psi(x)} H_{x',x} , \tag{2.18}$$

Eq. (2.17) can be written as

$$E = \frac{\sum_x E_x \Psi^2(x)}{\sum_x \Psi^2(x)} . \tag{2.19}$$

The local energy E_x depends crucially on the choice of the wavefunction $|\Psi\rangle$, in particular, if $|\Psi\rangle$ is an eigenstate of H with eigenvalue E, it comes out from Eq. (2.18) that $E_x = E$, and the Monte Carlo method is free from statistical fluctuations.

The evaluation of Eq. (2.19) can be done by generating a sample X of $\mathcal{N}$ configurations according to the probability distribution

$$P(x) = \frac{\Psi^2(x)}{\sum_{x'} \Psi^2(x')} \tag{2.20}$$

and then averaging the values of the local energy over these configurations

$$E \simeq \frac{1}{\mathcal{N}} \sum_{x \in X} E_x . \tag{2.21}$$

In practice, the simplest method to generate a set of configurations according to the probability distribution $P(x)$ is the Metropolis algorithm [15]: given a configuration x,

a new configuration x' is accepted if a random number ξ, between 0 and 1, satisfied the condition

$$\xi < \frac{P(x')}{P(x)} = \left[\frac{\Psi(x')}{\Psi(x)}\right]^2, \tag{2.22}$$

otherwise the new configuration is kept equal to the old one, $x' = x$.

By the Variational Monte Carlo, it is possible to calculate any kind of expectation value over a given wavefunction in a similar way

$$\langle O \rangle = \frac{\langle \Psi | O | \Psi \rangle}{\langle \Psi | \Psi \rangle} = \frac{\sum_x O_x \Psi^2(x)}{\sum_x \Psi^2(x)}, \tag{2.23}$$

where

$$O_x = \frac{\langle x | O | \Psi \rangle}{\langle x | \Psi \rangle} = \sum_{x'} \frac{\Psi(x')}{\Psi(x)} O_{x',x}. \tag{2.24}$$

An important point is that the only rigorous result is the upper bound to the ground-state energy, and there are no criteria about the accuracy of other properties of the ground-state, such as $\langle O \rangle$.

2.2.1 Systematic improvement by Lanczos steps

A given trial wavefunction $|\Psi\rangle$ can be systematically improved by applying p times the Hamiltonian and then by constructing a linear combination of all the p terms

$$|\Psi_{\alpha_1,\ldots,\alpha_p}\rangle = \sum_{i=1,\ldots,p} \alpha_i H^i |\Psi\rangle, \tag{2.25}$$

where the coefficients α_i are variational parameters. If we want to calculate the expectation value of H over Eq. (2.25), we need all the moments $\langle \Psi | H^i | \Psi \rangle$ up to the order $2p+1$. In principle, if we want to calculate exactly the moments, the above description is straightforward, but, in practice, it has serious computational limitations, because the time required for the evaluation of the moments grows exponentially with the number of Lanczos steps. On the other hand, if we compute the moments stochastically, we face the problem of having statistical errors, that strongly affect the final expectation value of the Hamiltonian.

What we can easily do is to consider $p = 1$, in this case it is possible to evaluate the expectation value of the Hamiltonian over

$$|\Psi_\alpha\rangle = (1 + \alpha H)|\Psi\rangle, \tag{2.26}$$

with a reasonable amount of computer time. For an efficient way to find the optimal value of the parameter α see Appendix B. In this case we have

$$E^\alpha = \frac{\langle \Psi_\alpha | H | \Psi_\alpha \rangle}{\langle \Psi_\alpha | \Psi_\alpha \rangle} = \frac{\sum_{x,x'} \Psi_\alpha(x') H_{x',x} \Psi_\alpha(x)}{\sum_x \Psi_\alpha^2(x)}, \tag{2.27}$$

where $\Psi_\alpha(x) = \langle x|\Psi_\alpha\rangle$.

By defining the local energy as

$$E_x^\alpha = \sum_{x'} H_{x',x} \frac{\Psi_\alpha(x')}{\Psi_\alpha(x)}, \tag{2.28}$$

we obtain

$$E^\alpha = \frac{\sum_x E_x^\alpha \Psi_\alpha^2(x)}{\sum_x \Psi_\alpha^2(x)}, \tag{2.29}$$

which can be stochastically sampled using Monte Carlo by generating configurations according to $\Psi_\alpha^2(x)/\sum_{x'} \Psi_\alpha^2(x')$. Notice that the ratio $\Psi_\alpha(x')/\Psi_\alpha(x)$, necessary to the Metropolis algorithm, is evaluated by using the fact that

$$\frac{\Psi_\alpha(x')}{\Psi_\alpha(x)} = \frac{\langle x'|(1+\alpha H)|\Psi\rangle}{\langle x|(1+\alpha H)|\Psi\rangle} = \frac{\Psi(x')}{\Psi(x)} \left(\frac{1+\alpha E_{x'}}{1+\alpha E_x}\right). \tag{2.30}$$

Therefore, at each Monte Carlo step, we have to calculate the local energy of the trial wavefunction $|\Psi\rangle$ both on the configuration x and x'. This kind of calculation takes order of the number of the lattice sites operations. Notice that we have to evaluate all the matrix elements $\langle x'|H|\Psi\rangle$, even if the movement from x to x' is not accepted. It is easy to see that, if we want to perform p Lanczos steps exactly, we have to calculate quantities like $\langle x'|H^i|\Psi\rangle$ for $i = 1, \ldots, 2p+1$, which takes an exponential increasing time with p. Indeed we have to consider all the possible configurations which come from the application of H^i to x'.

In Section 2.4, we will show an efficient way to perform the Lanczos steps by using the stochastic reconfiguration technique.

2.3 Green function Monte Carlo

2.3.1 Basic principles

The Green function Monte Carlo (GFMC) [16] is a stochastic technique that allows us to filter out the ground-state $|\Phi_0\rangle$ of an Hamiltonian H from a trial wavefunction $|\Psi_T\rangle$, provided that $\langle\Psi_T|\Phi_0\rangle \neq 0$, by using the power method Eq. (2.1).

In practice we define a basis $|x\rangle$ (e.g. the spin configuration of the lattice) and the iterative application of the Green function $G_{x',x}$ given by Eq. (2.1) reads

$$\Psi_{n+1}(x') = \sum_x G_{x',x} \Psi_n(x). \tag{2.31}$$

On large sizes it is not possible to evaluate exactly this recursive equation. Indeed, after few steps, the application of G generates transitions to a very large number of

different states, implying a huge amount of memory occupation. Therefore an alternative approach is necessary. The solution is to sample in a statistical way the matrix-vector product (2.31) by defining a Markov process.

In order to implement efficiently the power method, it is convenient to consider not the original matrix G, but the slightly more involved non-symmetric one [86]

$$\bar{G}_{x',x} = \frac{\Psi_G(x')}{\Psi_G(x)} G_{x',x}, \tag{2.32}$$

where $\Psi_G(x)$ is the so-called *guiding wavefunction*. The convenience of using $\bar{G}$ instead of G comes out from the following argument. If we consider $\bar{G}$, the local energy E_x is given by

$$E_x = \sum_{x'} \frac{\Psi_G(x')}{\Psi_G(x)} H_{x',x} = \sum_{x'} \bar{H}_{x',x}. \tag{2.33}$$

Thus if $\Psi_G(x)$ is exactly equal to the ground-state of H then $E_x = E_0$, independently on x. This is the so called zero-variance property, namely if the guiding wavefunction approaches an exact eigenstate of H, the method is free of statistical fluctuations. The guiding wavefunction has to be as simple as possible to be efficiently implemented in the calculation of the matrix elements and as close as possible to the ground-state of G. Moreover, it is easy to show that if $\Phi_i(x)$ is an eigenvector of G with eigenvalue E_i, then $\Psi_G(x)\Phi_i(x)$ is an eigenvector of $\bar{G}$ with the same eigenvalue, i.e. G and $\bar{G}$ have the same spectrum. It is worth noting that, after the importance sampling transformation (2.32), the iteration step (2.31), reads

$$\Psi_{n+1}(x')\Psi_G(x') = \sum_x \bar{G}_{x',x} \Psi_n(x)\Psi_G(x). \tag{2.34}$$

For simplicity, from now on the bar over an operator represents the same operator after the importance sampling transformation.

2.3.2 Statistical implementation of the power method

In order to define the statistical implementation of Eq. (2.34), we decompose the matrix $\bar{G}_{x',x}$ in terms of three factors:

$$\bar{G}_{x',x} = s_{x',x} p_{x',x} b_x, \tag{2.35}$$

where $s_{x',x}$ is the sign of $\bar{G}_{x',x}$, b_x is a normalization factor and $p_{x',x}$ is a *stochastic matrix*, i.e. it fulfills the conditions $p_{x',x} \geq 0$ and $\sum_{x'} p_{x',x} = 1$.

The basic element of the stochastic process is the *walker*, which, in the simplest formulation, is defined by (x, w), i.e. by its configuration in the lattice x and by a

weight w. Stochastically, the iteration (2.34) is interpreted as a transition of the walker $x \to x'$, whereas the weight of the walker is scaled $w \to w' = s_{x',x} b_x w$. This scheme defines a Markov process in the walker space (x, w). The basic idea of the stochastic implementation of Eq. (2.34) is that, although the number of non-zero elements of $\bar{G}_{x',x}$ is of the order of the Hilbert space times the number of sites, the number of non-zero entries in each column is of the order of the number of sites. Therefore all the non-zero elements of $\bar{G}_{x',x}$ for a fixed x can be computed, even for large size systems.

The previous Markov iteration allows us to define the evolution of the probability distribution $P_n(w, x)$ to have a walker with weight w and configuration x, namely:

$$P_{n+1}(w', x') = \sum_x \frac{p_{x',x}}{b_x} P_n \left(\frac{w'}{b_x s_{x',x}}, x \right) . \tag{2.36}$$

The first momentum of the probability distribution $P_n(w, x)$ completely determines the wavefunction wavefunction $\Psi_n(x)$ of the power method (2.1)

$$\Psi_n(x)\Psi_G(x) = \int dw\, w\, P_n(w, x). \tag{2.37}$$

Indeed, it can be easily seen that the evolution (2.36) correctly reproduces the dynamics of the wavefunction, Eq. (2.34). Therefore, after an equilibration, the probability $P_n(w, x)$ converges to its equilibrium limit $P^*(w, x)$, which defines the ground-state wavefunction

$$\Phi_0(x)\Psi_G(x) = \int dw\, w\, P^*(w, x). \tag{2.38}$$

Therefore, the ground-state energy is given by

$$E_0 = \frac{\langle \Psi_G | H | \Phi_0 \rangle}{\langle \Psi_G | \Phi_0 \rangle} = \frac{\sum_{x,x'} \bar{H}_{x',x} \int dw\, w\, P_0(w, x)}{\sum_x \int dw\, w\, P_0(w, x)}. \tag{2.39}$$

Using the fact that the local energy $E_x = \sum_{x'} \bar{H}_{x',x}$, we have that the ground-state energy E_0 can be computed over a sample X of independent $\mathcal{N}$ values of configurations

$$E_0 \simeq \frac{\sum_{(w,x)\in X} w E_x}{\sum_{(w,x)\in X} w}. \tag{2.40}$$

In addition, within the same Monte Carlo sampling, it is also possible to calculate the so-called *mixed averages* [16] of arbitrary linear operators O,

$$\langle O \rangle_{\mathrm{MA}} = \frac{\langle \Psi_G | O | \Phi_0 \rangle}{\langle \Psi_G | \Phi_0 \rangle}. \tag{2.41}$$

In fact, such mixed averages can be calculated using Eq. (2.40) by substituting the local energy E_x with the local estimator associated to the operator O, namely

$$O_x = \sum_{x'} \bar{O}_{x',x} . \tag{2.42}$$

where $\bar{O}_{x',x}$ are the operator matrix elements transformed according to the guiding wavefunction.

In the practical implementation of the method, since the walker weights grow exponentially with the Markov iteration, the procedure for the statistical evaluation of the ground-state energy and the mixed averages is slightly different. We can consider that, after many iterations, the configuration x, generated in the Markov process, is distributed according to the maximum right eigenstate of the matrix $p_{x',x}$. This state is different from the state $\Psi_G(x)\Phi_0(x)$ we are interested in, and we can consider it as a trial state in the power method. At any Markov iteration we can compute the weight of the walker assuming that L iterations before it was equal to 1. In this way the ground-state energy is given by

$$E_0 = \frac{\sum_n E_{x_n} G_n^L}{\sum_n G_n^L}, \tag{2.43}$$

where

$$G_n^L = \prod_{j=1}^{L} b_{x_{n-j}} s_{x_{n-j+1},x_{n-j}}. \tag{2.44}$$

In principle, the previously described procedure is free from any approximation, and, it gives exact results within the statistical errors. Unfortunately there are two main technical problem. The first one is that the weight G_n^L grows exponentially by increasing L, implying a divergent variance in the energy average. Indeed G_n^L is a product of L different factors and it can assume very large or very small values. This problem has a simple solution by considering the GFMC technique with many walkers and by introducing a reconfiguration scheme, which enables to drop out the irrelevant walkers with small weights. Recently, Calandra and Sorella [53] have introduced a reconfiguration scheme working at fixed number of walkers, in a way that allows us to control the bias due to the finite walker population, which we will describe in the following.

The second problem is much more serious and it is related to the *sign problem*. It is due to the fact that the average sign,

$$\langle s_L \rangle = \frac{\sum_n G_n^L}{\sum_n |G_n^L|}, \tag{2.45}$$

vanishes exponentially with L. Indeed walkers with positive and negative weights cancel almost exactly, giving rise to an exponentially small quantity to sample, with huge fluctuations. In the following Sections we will discuss different ways to introduce some approximation to avoid the sign problem.

Let us focus on the first problem and, in order to show how the reconfiguration scheme works, let consider a case without sign problem, i.e. with $s_{x',x} = 1$. We consider

M walkers and label the corresponding configurations and weights with a couple of vectors $(\mathbf{x}, \mathbf{w})$, with each component (x_i, w_i), $i = 1, \ldots, M$ corresponding to the i^{th} walker. It is easy to generalize Eq. (2.36) to many independent walkers

$$P_{n+1}(\mathbf{w}', \mathbf{x}') = \sum_{x_1,\ldots,x_M} P_n\left(\frac{w'_1}{b_{x_1}}, \ldots, \frac{w'_M}{b_{x_M}}\right) \frac{p_{x'_1,x_1} \ \cdots \ p_{x'_M,x_M}}{b_{x_1} \ \ldots \ b_{x_M}}. \tag{2.46}$$

Again, the wavefunction $\Psi_n(\mathbf{x})$ is completely determined by the first momentum of the probability $P_n(\mathbf{w}, \mathbf{x})$, namely

$$\Psi_n(x)\Psi_G(x) = \int [\mathbf{dw}] \sum_{\mathbf{x}} \frac{\sum_j w_j \delta_{x,x_j}}{M} P_n(\mathbf{w}, \mathbf{x}). \tag{2.47}$$

If the evolution of $P_n(\mathbf{w}, \mathbf{x})$ is done without any restriction, we have that each walker is completely uncorrelated from the other

$$P_n(\mathbf{w}, \mathbf{x}) = \prod_{i=1,\ldots,M} P_n(w_i, x_i). \tag{2.48}$$

In order to prevent the divergence of the weights, we define a reconfiguration process that changes the probability distribution without changing its first momentum, i.e. the wavefunction:

$$P'_n(\mathbf{w}', \mathbf{x}') = \int [\mathbf{dw}] \sum_{\mathbf{x}} K(\mathbf{w}', \mathbf{x}', \mathbf{w}, \mathbf{x}) P_n(\mathbf{w}, \mathbf{x}), \tag{2.49}$$

where the kernel $K(\mathbf{w}', \mathbf{x}', \mathbf{w}, \mathbf{x})$ is given by

$$K(\mathbf{w}', \mathbf{x}', \mathbf{w}, \mathbf{x}) = \prod_{i=1}^{M} \left(\frac{\sum_j w_j \delta_{x'_i,x_j}}{\sum_j w_j}\right) \delta(w'_i - \frac{1}{M}\sum_j w_j), \tag{2.50}$$

where the symbol $\int [\mathbf{dw}]$ indicates the M dimensional integral over the w_i variables.

In practice this reconfiguration process amounts to generate a new set of M walkers $(\mathbf{x}', \mathbf{w}')$ in terms of the old M walkers $(\mathbf{x}, \mathbf{w})$ in the following way: each new walker will have a weight $\bar{w} = \frac{1}{M}\sum_j w_j$ and a new configuration x'_i among the possible old ones x_j, chosen with a probability $p_i = w_{j(i)} / \sum_k w_k$. After this reconfiguration scheme, all the new walkers have the same weight and most of the irrelevant walkers with small weight are dropped out. Moreover it is easy to show that this kind of reconfiguration does not change the first momentum of the probability distribution [53].

2.3.3 Fixed-node approximation

When the weights of the walkers are not all positive it is always possible to define the transition probability for the stochastic process, but even if the Markov process converges to a probability distribution which determines the ground-state wavefunction, calculations are unstable due to wild cancelations between positive and negative weights. It is then necessary to consider some kind of approximation. The fixed-node (FN) approximation [17] defines an effective Hamiltonian $\bar{H}^{eff}$, starting from $\bar{H}$, setting to zero the positive off diagonal elements of $\bar{H}$

$$\bar{H}^{eff}_{x',x} = \begin{cases} \bar{H}_{x',x} & \text{if} \quad \bar{H}_{x',x} \leq 0 \\ 0 & \text{if} \quad \bar{H}_{x',x} > 0. \end{cases} \tag{2.51}$$

Moreover, in order to have variational results for the energies, it is also necessary that the diagonal term takes an additional sign-flip contribute:

$$\bar{H}^{eff}_{x,x} = \bar{H}_{x,x} + \mathcal{V}_{sf}(x) \tag{2.52}$$

$$\mathcal{V}_{sf}(x) = \sum_{\bar{H}_{x',x}>0, x' \neq x} \bar{H}_{x',x}. \tag{2.53}$$

A generalization of the fixed node approximation can be obtained defining the effective Hamiltonian in a slightly different way. Indeed reversing the sign of the positive off-diagonal matrix elements of $\bar{H}$ and multiplying them by a constant $\gamma > 0$ one obtains:

$$\bar{H}^{eff}_{x',x} = \begin{cases} \bar{H}_{x',x} & \text{if} \quad \bar{H}_{x',x} \leq 0 \\ -\gamma \bar{H}_{x',x} & \text{if} \quad \bar{H}_{x',x} > 0. \end{cases} \tag{2.54}$$

The diagonal term must be changed as

$$\bar{H}^{eff}_{x,x} = \bar{H}_{x,x} + (1+\gamma)\mathcal{V}_{sf}(x). \tag{2.55}$$

Note that the standard FN dynamic is recovered with $\gamma = 0$, while the case with $\gamma = -1$ is the opposite limit in which $\bar{H}^{eff} = \bar{H}$. The energy only slightly depends on γ and the lowest value can be obtained in the standard FN framework, i.e. $\gamma = 0$. Nevertheless the introduction of γ allows us transition to states on different nodal regions. This feature will be extensively used in the framework of the Green function with stochastic reconfiguration.

The FN approximation gives an upper bound of the ground-state energy. Indeed if we consider any state $|\Psi\rangle$, and we compare its energy with respect to H and H^{eff}:

$$\Delta E = \langle \Psi | \left(H^{eff} - H \right) | \Psi \rangle, \tag{2.56}$$

we obtain:

$$\Delta E = (1+\gamma) \sum_{\bar{H}_{x',x}>0, x' \neq x} |H_{x,x'}| \left| \Psi(x) \sqrt{\left| \frac{\Psi_G(x')}{\Psi_G(x)} \right|} - \Psi(x') \sqrt{\left| \frac{\Psi_G(x)}{\Psi_G(x')} \right|} \mathrm{sgn} H_{x,x'} \right|^2 . \tag{2.57}$$

Because ΔE is positive for any wavefunction, it comes out that the ground-state of H^{eff} is an upper bound of the ground-state of H. Moreover the GFMC method can calculate the exact ground-state energy E_0^{eff} and the wavefunction Ψ^{eff} of H^{eff}, without any sign problem. Hence

$$E_0^{eff} \geq \frac{\langle \Psi^{eff} | H | \Psi^{eff} \rangle}{\langle \Psi^{eff} | \Psi^{eff} \rangle} \geq E_0, \tag{2.58}$$

where the last inequality follows from the usual variational principle. Therefore we can conclude that the FN energy is an upper bound to the true ground-state energy. Furthermore, because one can easily verify that $\langle \Psi_G | H | \Psi_G \rangle = \langle \Psi_G | H^{eff} | \Psi_G \rangle$, one can be sure that the GFMC procedure improves the energy of the guiding wavefunction

$$E_0^{eff} \leq \frac{\langle \Psi_G | H^{eff} | \Psi_G \rangle}{\langle \Psi_G | \Psi_G \rangle} = \frac{\langle \Psi_G | H | \Psi_G \rangle}{\langle \Psi_G | \Psi_G \rangle}. \tag{2.59}$$

2.3.4 Forward walking technique

The GFMC technique can be used with success to compute also correlation functions on the ground-state of H. In particular, it is simple to compute expectation values of operators that are diagonal in the working basis, so that $O_{x,x'} = \delta_{x,x'} \langle x|O|x \rangle$. By using GFMC, the configurations of the walkers are distributed as $\Psi_G(x)\Phi_0(x)$, however, in order to compute

$$\langle O \rangle = \frac{\langle \Psi_0 | O | \Psi_0 \rangle}{\langle \Psi_0 | \Psi_0 \rangle}, \tag{2.60}$$

a further work is required.

To this purpose, the desired expectation value is written as

$$\langle O \rangle = \lim_{N,N' \to \infty} \frac{\langle \Psi_G | H^N O H^{N'} | \Psi \rangle}{\langle \Psi_G | H^{N+N'} | \Psi \rangle}. \tag{2.61}$$

From a statistical point of view, Eq. (2.61) amounts first to sample a configuration x after N' GFMC steps, then to measure the quantity $\langle x|O|x \rangle$, and finally to let the walker propagate forward for further N steps. In order to evaluate the stochastic average, an approach similar to that done for the energy is possible. In this case we have:

$$\langle O \rangle = \frac{\sum_n O^n G_n^L}{\sum_n G_n^L}, \tag{2.62}$$

where O^n is the average over the walker population of the operator O at the generation n, i.e. $O^n = \frac{1}{M}\sum_j O_j^n$, being O_j^n the value of the operator O on the configuration x_j of the j^{th} walker at the iteration n, and

$$G_n^L = \prod_{j=-N}^{L-1} \bar{w}_{n-j}. \tag{2.63}$$

Notice that the correcting factors G_n^L are different from the case of the energy. Indeed, in this case, G_n^L contain a further propagation of N steps as compared to the previous expression.

A further condition is necessary in order to control the bias in the forward walking technique. The set of measured values O_j^n with weight factors given by Eq. (2.63) has to be modified after each reconfiguration process occurring in the forward direction. In practice after each reconfiguration, we have to bookkeep only the values O_j^n of the observable that survive after the reconfiguration. Therefore, after each reconfiguration, $O_i^{n\prime} = O_{j(i)}$, for $i = 1, \ldots, M$ and the function $j(i)$ describing the reconfiguration scheme has to be computed: the walker with index i assumes the configuration with index $j(i)$ before the reconfiguration.

In order to implement recursively the forward walking, it is useful to store at each reconfiguration the integer function $j_n(i)$ for each reconfiguration n and the value of O_i^n of the operator for each walker. Then it is possible to compute the relevant configurations contributing to the operator O after N reconfiguration steps by recursive application of the integer function $j_n(i)$.

2.3.5 Green function Monte Carlo with stochastic reconfiguration

The GFMC with stochastic reconfiguration (SR) [18, 19] represents a systematic improvement of the FN approximation that allows us to sample the sign changes of the guiding wavefunction. This method is based upon the simple requirement that, after a short propagation via the approximate FN dynamics, a number p of correlation functions over the state $\Psi_n(x)$ can be constrained to be exact by a small perturbation of the FN evolved state $\Psi_n^{eff}(x)$, which is free from sign problem. By iterating this process the average sign remains stable. Moreover the method has the important property to be exact if all the possible correlation functions are included.

Therefore, in the original formulation, the main idea of the SR is to replace the many-body state $\Psi_n(x)$, to which the exact Green function has been applied, with an approximate state related to the FN dynamics. In this way, the Green function $\bar{G}_{x',x}$ is

related to the FN one $\bar{G}^{eff}_{x',x}$ by a factor $s_{x',x}$

$$\bar{G}_{x',x} = s_{x',x}\bar{G}^{eff}_{x',x}, \tag{2.64}$$

where

$$s_{x',x} = \begin{cases} 1 & \text{if} \quad \bar{G}_{x',x} \geq 0 \\ -\frac{1}{\gamma} & \text{if} \quad \bar{G}_{x',x} < 0 \\ \frac{\Lambda - H_{x,x}}{\Lambda - H^{eff}_{x,x}} & \text{if} \quad x = x'. \end{cases} \tag{2.65}$$

Notice that we have

$$b_x = \sum_{x'} \bar{G}_{x',x} = \sum_{x'} \bar{G}^{eff}_{x',x}. \tag{2.66}$$

The appropriate stochastic process relative to the Hamiltonian H can be defined by the following three steps:

1. Given the walker (x, w), change the weight by scaling it with b_x:

$$w \to b_x w \ .$$

2. Generate randomly a new configuration x' according to the stochastic matrix $p_{x',x}$.

3. Finally multiply the weight of the walker by $s_{x',x}$:

$$w' \to w s_{x',x} \ .$$

Without the last step, one is actually sampling the fixed-node Hamiltonian H^{eff}. In the simulation both the dynamics given by $\bar{G}^{eff}$ and by $\bar{G}$ are followed, by updating both the weight w associated to the true Hamiltonian and the weight w^{eff} associated to the approximate H^{eff}. Therefore the walker can be characterized by the triad (x, w, w^{eff}). The previous algorithm allows us to define the evolution of the probability to find the walker with weights w and w^{eff}, in a configuration x, namely:

$$P_{n+1}(w', w^{eff'}, x') = \sum_x \frac{p_{x',x}}{b_x^2 |s_{x',x}|} P_n \left(\frac{w'}{b_x s_{x',x}}, \frac{w^{eff'}}{b_x}, x \right). \tag{2.67}$$

The first moments of the probability distribution $P_n(w, w^{eff}, x)$ over w and w^{eff} give the state $\Psi_n(x)$, propagated with the exact $\bar{G}$, and the state $\Psi^{eff}_n(x)$, propagated with the approximate $\bar{G}^{eff}$, respectively

$$\Psi_n(x)\Psi_G(x) = \int dw \int dw^{eff}\, w\, P_n(w, w^{eff}, x) \tag{2.68}$$

$$\Psi^{eff}_n(x)\Psi_G(x) = \int dw \int dw^{eff}\, w^{eff}\, P_n(w, w^{eff}, x). \tag{2.69}$$

The iteration step reads

$$\Psi_{n+1}(x')\Psi_G(x') = \sum_x \bar{G}_{x',x}\Psi_n(x)\Psi_G(x) \quad (2.70)$$

$$\Psi^{eff}_{n+1}(x')\Psi_G(x') = \sum_x \bar{G}^{eff}_{x',x}\Psi^{eff}_n(x)\Psi_G(x). \quad (2.71)$$

The generalization of this algorithm for many walkers is straightforward: if we consider M walkers and we label the corresponding configurations and weights by $(\mathbf{x}, \mathbf{w})$, with each component (x_i, w_i, w_i^{eff}) referring to the i^{th} walker, for $i = 1, \ldots M$, we have

$$\Psi_n(x)\Psi_G(x) = \int [\mathbf{dw}] \sum_{\mathbf{x}} \frac{\sum_j w_j \delta_{x,x_j}}{M} P_n(\mathbf{w}, \mathbf{x}) \quad (2.72)$$

$$\Psi^{eff}_n(x)\Psi_G(x) = \int [\mathbf{dw}] \sum_{\mathbf{x}} \frac{\sum_j w^{eff}_j \delta_{x,x_j}}{M} P_n(\mathbf{w}, \mathbf{x}), \quad (2.73)$$

the symbol $\int [\mathbf{dw}]$ indicates the $2M$ dimensional integral over the (w_i, w_i^{eff}) variables, $i = 1, \ldots, M$. The reference weights w_i^{eff} sample statistically the reference state $\Psi^{eff}_n(x)\Psi_G(x)$, whereas the weights w_i refers to the state $\Psi_n(x)\Psi_G(x)$, propagated by the exact Green function, namely:

$$\langle\langle w_i^{eff}\delta_{x,x_i}\rangle\rangle = \Psi^{eff}_n(x)\Psi_G(x) \quad (2.74)$$

$$\langle\langle w_i\delta_{x,x_i}\rangle\rangle = \Psi_n(x)\Psi_G(x), \quad (2.75)$$

where the brackets $\langle\langle \ \ \rangle\rangle$ indicate both the average over the number of walkers at a given Markov iteration n and the statistical average.

The Eqs. (2.72) and (2.73) show that the states $\Psi_n(x)$ and $\Psi^{eff}_n(x)$ do not uniquely determines the walker probability $P_n(\mathbf{w}, \mathbf{x})$, but, as for the case without sign problem, it is possible to change the probability distribution without changing the exact information content, i.e. $\Psi_n(x)$ and $\Psi^{eff}_n(x)$. In this regard it is possible to define a linear transformation, described by a simple kernel $X(\mathbf{w}', \mathbf{x}'; \mathbf{w}, \mathbf{x})$

$$P'_n(\mathbf{w}', \mathbf{x}') = \int [\mathbf{dw}] \sum_{\mathbf{x}} X(\mathbf{w}', \mathbf{x}'; \mathbf{w}, \mathbf{x}) P_n(\mathbf{w}, \mathbf{x}). \quad (2.76)$$

The kernel is defined by:

$$\begin{aligned} X(\mathbf{w}', \mathbf{x}'; \mathbf{w}, \mathbf{x}) &= \prod_{i=1}^{M} \left(\frac{\sum_j |p_{x_j}| \delta_{x'_i,x_j}}{\sum_j |p_{x_j}|} \right) \\ &\times \delta \left(w'_i - \beta^{-1} \frac{\sum_j w_j}{M} \mathrm{sgn} p_{x'_i} \right) \\ &\times \delta \left(w_i^{eff\prime} - |w'_i| \right), \end{aligned} \quad (2.77)$$

where

$$\beta = \frac{\sum_j p_{x_j}}{\sum_j |p_{x_j}|}, \tag{2.78}$$

the coefficients p_{x_j} will be defined in the following. Notice that the outcoming variables x'_j and w'_j are completely independent for different j values. Therefore it is possible to integrate each of the M factors of the kernel in the variables w'_j and $w_j^{eff'}$ and to sum over the new configurations x'_j, the result being simply one, as required by the normalization condition of the density probability. In the reconfiguration process, the new configurations x'_i are taken randomly among the old ones x_j, according with the probability $|p_{x_{j(i)}}|/\sum_k |p_{x_k}|$, defined below in terms of the weights w_j, w_j^{eff} and the configurations x_j. Furthermore the new weights w'_i are taken as

$$w'_i = \beta^{-1} \frac{\sum_k w_k}{M} \mathrm{sgn} p_{x'_{j(i)}}, \tag{2.79}$$

whereas the FN weights are restricted to be positive

$$w_i^{eff'} = |w'_i|. \tag{2.80}$$

In this way, after each reconfiguration

$$\Psi_n(x) \to \Psi'_n(x), \tag{2.81}$$

moreover, also the reference state explicitly depends on the SR iteration, and after each reconfiguration

$$\Psi_n^{eff}(x) \to \mathrm{sgn}\Psi_G(x)|\Psi'_n(x)|. \tag{2.82}$$

The reason of this choice is to optimize the reference state and make it as close as possible to $\Psi'_n(x)$, being the signs fixed by $\Psi_G(x)$.

The coefficient β guarantees that the normalization of the wavefunction is preserved

$$\sum_x \Psi'_n(x) = \sum_x \Psi_n(x). \tag{2.83}$$

The only quantities which we need to define are the coefficients p_{x_j}. The important point is that these coefficients are not restricted to be positive, and they may depend on all the weights w_j, the configurations x_j and the reference weights w_j^{eff}.

The choice $p_{x_j} = w_j$ is exact in the sense that $\Psi'_n(x) = \Psi_n(x)$, and coincides with the one for the case without sign problem. However this choice is not convenient, because this reconfiguration will not improve the average sign, which will decay exponentially to zero. Instead, in the case with sign problem, we can parameterize the coefficients p_{x_j} by assuming that they are close enough to the positive definite weights

w_j^{eff}, the ones obtained with $\bar{G}^{eff}$. The reason for this choice is that, though the weights w_j^{eff} may be occasionally very different from the exact ones w_j, namely their sign can be wrong, they sample a state $\Psi_n^{eff}(x)$, which is supposed to be quite close to the exact propagated one $\Psi_n(x)$. This condition is clearly verified for an appropriate choice of the guiding wavefunction, making the FN accurate. Then, we can assume that small perturbations over the state $\Psi_n^{eff}(x)$ may lead to fulfill the equality

$$\Psi'_n(x) = \Psi_n(x), \tag{2.84}$$

with an arbitrary small error. Therefore we can assume that the p_{x_j} are given by small correction to the w_j^{eff}

$$p_{x_j} = w_j^{eff} \left\{ 1 + \sum_k \alpha_k \left(O^k_{x_j} - O^{k,eff} \right) \right\}. \tag{2.85}$$

The corrections are taken proportional to the fluctuations of p different operators O^k , with corresponding local estimator

$$O^k_{x_j} = \frac{\langle \Psi_G | O^k | x_j \rangle}{\langle \Psi_G | x_j \rangle}, \tag{2.86}$$

and average value over the positive reference weights

$$O^{k,eff} = \frac{\sum_j w_j^{eff} O^k_{x_j}}{\sum_j w_j^{eff}}. \tag{2.87}$$

With the general form (2.85) for the coefficients p_{x_j}, it is possible to fulfill that all the mixed averages for the chosen p operators have the same value before and after the reconfiguration

$$\sum_{x,x'} \bar{O}^k_{x',x} \Psi'_n(x) = \sum_{x,x'} \bar{O}^k_{x',x} \Psi_n(x). \tag{2.88}$$

It can be proven [19] that, in order to fulfill exactly the SR conditions (2.88), it is *sufficient* that the p_{x_j} coefficients are chosen in a way that

$$\frac{\sum_j p_{x_j} O^k_{x_j}}{\sum_j p_{x_j}} = \frac{\sum_j w_j O^k_{x_j}}{\sum_j w_j}, \tag{2.89}$$

which can be fulfilled with a solution of a simple linear system for the unknown variables α_k, for $k = 1, \ldots, p$

$$\sum_{k'} S_{k,k'} \alpha_{k'} = \frac{\sum_j w_j \left(O^k_{x_j} - O^{k,eff} \right)}{\sum_j w_j}, \tag{2.90}$$

where $S_{k,k'}$ is the covariance matrix

$$S_{k,k'} = \frac{\sum_j w_j^{eff} \left(O_{x_j}^k - O^{k,eff} \right) \left(O_{x_j}^{k'} - O^{k',eff} \right)}{\sum_j w_j^{eff}}. \tag{2.91}$$

It is worth noting that, asymptotically, by adding more and more parameters α_k, we can achieve the condition $\Psi'_n(x) = \Psi_n(x)$ exactly, since the state $\Psi_n(x)$ is completely determined by its correlation functions. Indeed, consider the diagonal operators: all these operators may be written as a linear combination of elementary ones $O^{x_0}_{x',x} = \delta_{x',x}\delta_{x,x_0}$, acting on a single configuration x_0, plus at most an overall constant. If the conditions (2.88) are satisfied for all the elementary operators $O^{x_0}_{x',x}$, it follows that $\Psi'_n(x_0) = \Psi_n(x_0)$ for all x_0. Then it is simple to show that the coefficients p_{x_j} are invariant for any constant shift of the operators O^k. Furthermore, with a little algebra it turns out that these coefficients do not change for any linear transformation of the chosen operator set. Thus we prove the convergence of the SR for any sequence of diagonal operators, that, with increasing p, becomes complete. For non-diagonal operators $O_{x',x}$, we simply note that they assume the same mixed average values of the equivalent diagonal ones $O^{diag}_{x',x} = \delta_{x',x} \sum_{x'} O_{x',x}$. Thus the proof that the SR procedure converges to the exact solution is valid in general even for non-diagonal operators.

2.4 Few Lanczos steps from Monte Carlo technique

In this Section we show that the SR procedure can be considered as a projection of the exactly propagated state onto a particular subspace. By using as a reference dynamics the FN one, the method is not variational, but, if a different reference is taken, it comes out that the SR gives variational estimate of the energy. Moreover, we show that a slightly different approach allows us to perform p Lanczos steps on a given variational wavefunction.

Let us redefine the p_{x_j} coefficients as

$$p_{x_j} = w_j^{eff} \left\{ 1 + \sum_k \alpha_k O^k_{x_j} \right\}. \tag{2.92}$$

Then the constants α_k are determined by the condition

$$\alpha_k = \sum_{k'} S^{-1}_{k,k'} \frac{\sum_j w_j O^{k'}_{x_j}}{\sum_j w_j}, \tag{2.93}$$

where the covariance matrix is

$$S_{k,k'} = \frac{\sum_j w_j^{eff} O_{x_j}^k O_{x_j}^{k'}}{\sum_j w_j^{eff}}. \tag{2.94}$$

In this way, at each reconfiguration step, the new state $\Psi'_n(x)$ is defined starting from the reference one $\Psi_n^{eff}(x)$

$$\Psi'_n(x) = \left(\sum_k \alpha_k O_x^k \right) \Psi_n^{eff}(x) = r_x \Psi_n^{eff}(x), \tag{2.95}$$

with

$$O_x^k = \frac{\langle \Psi_G | O^k | x \rangle}{\langle \Psi_G | x \rangle}, \tag{2.96}$$

where $k = 0, \ldots, p$, O^0 being the identity operator. In the limit if large number of walkers, the constants α_k are given by

$$\alpha_k = \sum_{k'} S_{k,k'}^{-1} \sum_{x'} \Psi_G(x') \Psi_n(x') O_{x'}^{k'}, \tag{2.97}$$

with

$$S_{k,k'} = \sum_x \Psi_G(x) \Psi_n^{eff}(x) O_x^k O_x^{k'}. \tag{2.98}$$

Therefore the SR can be considered as a projection of the exactly propagated wavefunction onto the subspace spanned by the states $O_x^k \Psi_n^{eff}(x)$

$$\Psi'_n(x) = \sum_{x'} (\mathcal{P}_{SR})_{x,x'} \Psi_n(x'), \tag{2.99}$$

being

$$(\mathcal{P}_{SR})_{x,x'} = \sum_{k,k'} S_{k,k'}^{-1} O_x^k \Psi_n^{eff}(x) \Psi_G(x') O_{x'}^{k'}. \tag{2.100}$$

The operator $\mathcal{P}_{SR}$ is not a true projector, because, although it satisfies the requirement $\mathcal{P}_{SR}^2 = \mathcal{P}_{SR}$, the condition $\mathcal{P}_{SR}^\dagger = \mathcal{P}_{SR}$ is not generally satisfied. At equilibrium, the state $\Psi_n(x)$ represents the maximum right eigenvector of the matrix

$$\mathcal{G}_{SR} = \mathcal{P}_{SR} G \mathcal{P}_{SR} = \mathcal{P}_{SR} (\Lambda I - H) \mathcal{P}_{SR}. \tag{2.101}$$

The method is therefore rigorously variational *provided* the operator $\mathcal{P}_{SR}$ is a true projector, namely for $\Psi_n^{eff}(x) = \Psi_G(x)$. Indeed the maximum eigenvalue $(\Lambda - E_{SR})$ of the Hermitian matrix $\mathcal{P}_{SR}(\Lambda I - H)\mathcal{P}_{SR}$ is certainly smaller than the corresponding one

$(\Lambda - E_0)$ of the exact Green function $(\Lambda I - H)$. In fact if $\Psi_{SR}(x) = \mathcal{P}_{SR}\Psi_{SR}(x)$ is the eigenstate of $\mathcal{P}_{SR}(\Lambda I - H)\mathcal{P}_{SR}$ with eigenvalue $(\Lambda - E_{SR})$, then $\mathcal{P}_{SR}^{\dagger} = \mathcal{P}_{SR}$ implies

$$E_{SR} = \frac{\langle \Psi_{SR}|\mathcal{P}_{SR}H\mathcal{P}_{SR}|\Psi_{SR}\rangle}{\langle \Psi_{SR}|\mathcal{P}_{SR}\mathcal{P}_{SR}|\Psi_{SR}\rangle} = \frac{\langle \Psi_{SR}|H|\Psi_{SR}\rangle}{\langle \Psi_{SR}|\Psi_{SR}\rangle} \geq E_0. \tag{2.102}$$

In order to have a rigorous variational method, a further detail has to be taken into account. Indeed, after each reconfiguration, not only the state $\Psi_n(x)$ is replaced by $\Psi'_n(x)$, but also the reference state $\Psi_n^{eff}(x)$ is changed as

$$\Psi_n^{eff'}(x) = \mathrm{sgn}\Psi_G(x)|\Psi'_n(x)|. \tag{2.103}$$

Within the Monte Carlo method, instead of changing the weights of the reference wavefunction with the choice $w_i^{eff'} = |w'_i|$ (which implies Eq. (2.103), in the large number of walkers), it is possible to remain with the same reference state $\Psi_n^{eff}(x)$, without changing it during the simulation. This is obtained by the following *reweighting* scheme: after the reconfiguration, the new configurations x'_i are selected among the old ones x_j, according to the weights $|p_{x_j}|$. The new weights for the state $\Psi'_n(x)$ are taken as

$$w'_i = \frac{\sum_k |p_{x_k}|}{M}\mathrm{sgn}p_{x_{j(i)}}, \tag{2.104}$$

whereas the weights for the reference state $\Psi_n^{eff}(x)$ are taken as

$$w_i^{eff'} = \frac{\sum_k |p_{x_k}|}{M}\frac{w_{j(i)}^{eff}}{|p_{x_{j(i)}}|} = \frac{|w'_i|}{|r_{x'_i}|}. \tag{2.105}$$

In this way the walker population can describe both the wavefunction $\Psi'_n(x)$ and the reference one $\Psi_n^{eff'}(x)$, by considering the weights w'_i and $w_i^{eff'}$, respectively:

$$\langle\langle w_i^{eff'}\delta_{x,x_i}\rangle\rangle = \Psi_n^{eff'}(x)\Psi_G(x) \tag{2.106}$$

$$\langle\langle w'_i\delta_{x,x_i}\rangle\rangle = \Psi'_n(x)\Psi_G(x), \tag{2.107}$$

where, as stated before, the symbol $\langle\langle \quad \rangle\rangle$ stands for both the average over the walker population, at a given Markov iteration n, and the statistical average.

As the reference Green function, the one proposed by Hellberg and Manousakis [62] is the most convenient from the practical point of view of reducing statistical fluctuations

$$\bar{G}_{x',x}^{var} = \frac{1}{z_{x'}}|\Lambda\delta_{x',x} - \bar{H}_{x',x}|, \tag{2.108}$$

where

$$z_x = \sum_{x'}|\Lambda\delta_{x',x} - \bar{H}_{x',x}|. \tag{2.109}$$

By applying the power method with the Green function (2.108), the convergence is reached when the maximum right eigenvector $\Psi_G^2(x)$ is filtered out, namely

$$\sum_x \bar{G}^{var}_{x',x}\Psi_G^2(x) = \Psi_G^2(x'). \tag{2.110}$$

Thus this Green function can be used to generate configurations distributed according $\Psi_G^2(x)$ with a stochastic matrix

$$p^{var}_{x',x} = \frac{z_{x'}}{z_x}\bar{G}^{var}_{x',x}, \tag{2.111}$$

and, because in general Eq. (2.71) holds, we have that, using the fixed reference algorithm Eqs. (2.104) and (2.105), $\Psi_n^{eff}(x) = \Psi_G(x)$. Therefore, by using $\bar{G}^{var}_{x',x}$ as the reference Green function, the method is *rigorously variational*.

The advantage of using the reference Green function (2.108) is that it has a very simple relation with the exact one $\bar{G}_{x',x}$

$$\frac{\bar{G}_{x',x}}{\bar{G}^{var}_{x',x}} = s_{x',x} = \pm z_{x'}, \tag{2.112}$$

where the sign $\pm$ is given by the exact Green function matrix element. In this way, the stochastic conditions (2.88) can be fulfilled with high statistical accuracy since both the left and right hand side of Eq. (2.88) are sampled statistically with the same configurations and weights w_i and w_i^{eff}, which are highly correlated.

We notice an important property of this method: if we consider only operators defined by powers of the Hamiltonian, i.e. $O^k = H^k$ for $k = 0, \ldots, p$, the projector $\mathcal{P}_{SR}$ acts on the Krilov basis, the same of the Lanczos algorithm. Therefore $(\mathcal{P}_{SR}\bar{G}\mathcal{P}_{SR})^n$ filters out the lowest energy state in the Krilov basis, i.e. the state obtained by applying p Lanczos steps. Moreover, since $\Psi_G(x)$ belongs to the subspace projected by $\mathcal{P}_{SR}$, we have that $\langle\Psi_G|H\mathcal{P}_{SR} = \langle\Psi_G|\mathcal{P}_{SR}H$, and hence the mixed average of the energy coincides with the variational energy

$$\frac{\langle\Psi_G|H|\Psi_{SR}\rangle}{\langle\Psi_G|\Psi_{SR}\rangle} = \frac{\langle\Psi_G|\mathcal{P}_{SR}H\mathcal{P}_{SR}|\Psi_{SR}\rangle}{\langle\Psi_G|\mathcal{P}_{SR}|\Psi_{SR}\rangle} = E_{SR}. \tag{2.113}$$

The advantage of using the SR scheme to perform p Lanczos steps is due to the fact that it is sufficient to compute only p Hamiltonian powers on a given configuration. By contrast, in the conventional method, all the powers of the Hamiltonian up to $2p + 1$ are needed, leading to a much more demanding numerical effort. It is also important to emphasize that within this technique it is not necessary to optimize the parameters α_k, with an iterative procedure. These parameters are simply obtained at the end of the

simulation as a simple statistical average of the ones obtained by solving Eq. (2.93) for each Markov iteration.

In principle, with this method it is possible to perform p Lanczos steps onto a given wavefunction, but, in practice, only few powers of the Hamiltonian are feasible. By combining this technique with the one described in Section 2.2.1, it is easy to apply two Lanczos steps to a given variational wavefunction. In practice, first we apply one Lanczos step without using the SR scheme (see Section 2.2.1), then, we use the SR to reconstruct the second Lanczos step.

2.4.1 Variance extrapolation

A great advantage of the variational method is that we have an additional information about the quality of the trial wavefunction. Indeed the variance

$$\sigma^2 = \frac{1}{L^2}\left\{\frac{\langle\Psi|H^2|\Psi\rangle}{\langle\Psi|\Psi\rangle} - \left(\frac{\langle\Psi|H|\Psi\rangle}{\langle\Psi|\Psi\rangle}\right)^2\right\} \tag{2.114}$$

measures the width of the energy distribution of the wavefunction $|\Psi\rangle$. In other words it provides a criterion for how much $|\Psi\rangle$ deviates from an eigenfunction. Indeed the variance σ^2 vanishes for all the eigenstates of H, and a good variational state have both an energy close to E_0 and a small variance.

In practice the variance is easy to calculate by using Monte Carlo techniques, indeed, if we introduce a complete set $|x\rangle$ of states, we have

$$\frac{\langle\Psi|H^2|\Psi\rangle}{\langle\Psi|\Psi\rangle} = \frac{\sum_x \langle\Psi|H|x\rangle\langle x|H|\Psi\rangle}{\sum_x \Psi^2(x)} = \frac{\sum_x E_x^2 \Psi^2(x)}{\sum_x \Psi^2(x)}, \tag{2.115}$$

where we have used the definition of the local energy E_x, Eq. (2.18). Therefore the calculation of the variance can be performed sampling both the local energy and its square.

Suppose that a given wavefunction is close to the true ground-state $|\Psi_0\rangle$, i.e $|\Psi\rangle \sim |\Psi_0\rangle + \epsilon|\xi\rangle$, with $\langle\Psi_0|\xi\rangle = 0$ and $\langle\Psi_0|\Psi_0\rangle = \langle\xi|\xi\rangle = 1$, then its energy per site is

$$\frac{E}{L} = \frac{1}{L}\left\{\frac{E_0 + \epsilon^2\langle\xi|H|\xi\rangle}{1+\epsilon^2}\right\} \sim \frac{E_0}{L} + \frac{\epsilon^2}{L}(\langle\xi|H|\xi\rangle - E_0). \tag{2.116}$$

Therefore the difference between the variational and the exact energies vanishes linearly with ϵ^2. On the other hand the variance is given by

$$\sigma^2 = \frac{1}{L^2}\left\{\frac{E_0^2 + \epsilon^2\langle\xi|H^2|\xi\rangle}{1+\epsilon^2} - \left(\frac{E_0 + \epsilon^2\langle\xi|H|\xi\rangle}{1+\epsilon^2}\right)^2\right\}. \tag{2.117}$$

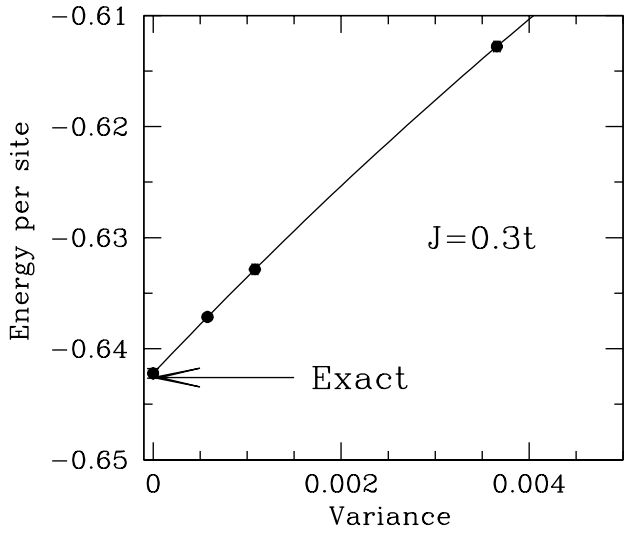

Figure 2.1: Energy per site extrapolation for the $t-J$ model, 4 holes on 26 sites, $J=0.3t$. $p=0,1,2$ Lanczos iterations over the projected d-wave wavefunction are reported. The extrapolated value of the energy is also shown, and the continuous line is a linear fit of the data.

Expanding to the leading order in ϵ^2, we obtain

$$\sigma^2 \sim \frac{\epsilon^2}{L^2}\langle\xi|\,(H-E_0)^2\,|\xi\rangle. \tag{2.118}$$

It follows that, if the trial wavefunction is close to the exact ground-state, we have that

$$\frac{E}{L} \sim \frac{E_0}{L} + \text{const} \times L \times \sigma^2. \tag{2.119}$$

The last relation can be used to extract information about E_0, we can use different values of E and σ^2, for different number of Lanczos iterations and extrapolate to $\sigma^2 = 0$, obtaining an estimate of E_0. This kind of estimate is not a variational bound and it is meaningful only if the starting wavefunction is a good approximation for the ground-state.

We note that the best information of the variance extrapolation is achieved by using the results of a *given* starting variational wavefunction (for example the one which minimizes the energy), and then by applying a certain number of Lanczos steps. By contrast, the information contained in different variational starting points may be questionable for the variance extrapolation. Indeed the relation between the energy and the variance for different variational wavefunctions is uncorrelated, because, in general the minimum for the energy does not coincide with the minimum for the variance. Instead the application of p Lanczos steps generates a hierarchy of wavefunctions in which each state strictly descends from the previous one, improving its energy and variance. In this way, the

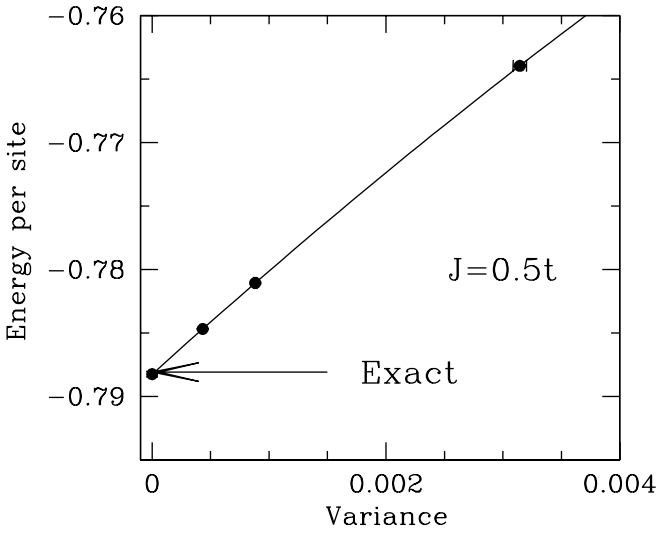

Figure 2.2: Energy per site extrapolation for the $t-J$ model, 4 holes on 26 sites, $J=0.5t$. $p=0,1,2$ Lanczos iterations over the projected d-wave wavefunction are reported. The extrapolated value of the energy is also shown, and the continuous line is a linear fit of the data.

gain in the energy is highly correlated to the gain in the variance, and we have the best possible information about the energy of the best state belonging to the class generated by the starting wavefunction.

As an example of how the variance extrapolation works, we report in Figs. 2.1 and 2.2 the case of the $t-J$ model for 4 holes on 26 sites, where the exact results are known by Lanczos diagonalization, for $J=0.3t$ and $J=0.5t$ respectively. We refer to Section 3.3.1 for a detailed description of the variational wavefunction, moreover we express all the energies in unit of t. Both the energy and the variance are improved by a factor of three by applying exactly one Lanczos step to the variational wavefunction. As described in the previous Section, by using the SR technique, it is also possible to perform two Lanczos steps onto the variational wavefunction. The gain in energy and in variance is another factor of two. This represents the best variational result: we obtain $E_{2L}/L=-0.6372(1)$ for $J=0.3t$, and $E_{2L}/L=-0.7847(1)$ for $J=0.5t$.

Moreover the three results for $p=0,1,2$ Lanczos steps can be used to extrapolate the exact energy by using Eq. (2.119). It turns out that the, non variational, estimate is exact in the statistical errors: for $J=0.3t$, where the exact result is $E_0/L=-0.6426$, we obtain $E/L=-0.6422(4)$, whereas for $J=0.5t$, where $E_0/L=-0.7881$, we have $E/L=-0.7882(2)$. It is worth noting that, besides the fact the variational results for $p=0$ are about 0.03 above in energy with respect to the exact ones, the three points with $p=0,1,2$ lies on the same straight line, and Eq. (2.119) holds.

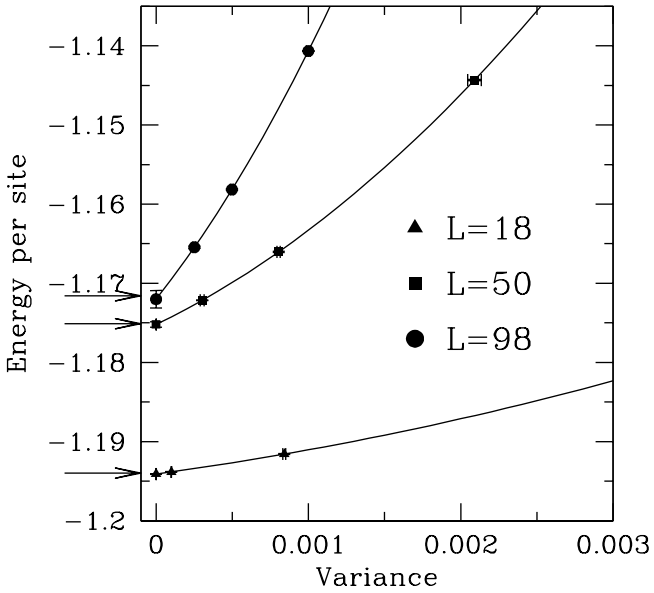

Figure 2.3: Energy per site of the finite-size Heisenberg model. Comparison of exact results (indicated by arrows) and the approximate $p = 0, 1, 2$ Lanczos iterations over the projected d-wave wavefunction for $L = 18$ (full triangles), $L = 50$ (full squares) and $L = 98$ (full circles). The extrapolated value of the energy is also shown, continuous lines are quadratic fit of the data.

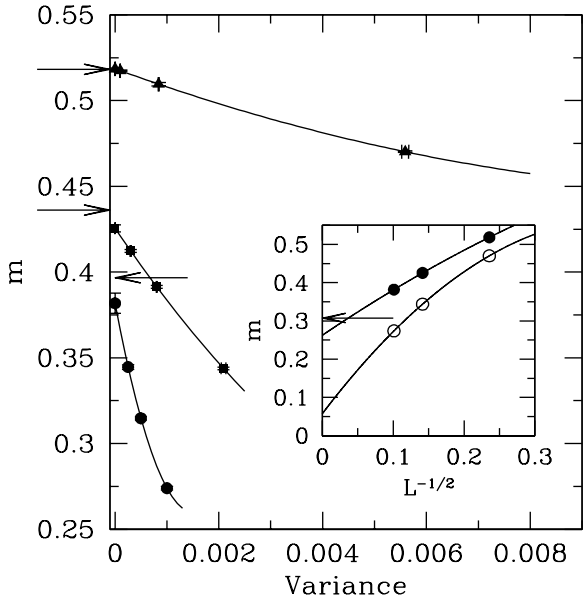

Figure 2.4: Order parameter $m = \sqrt{S(\pi,\pi)/L}$ in the finite-size Heisenberg model, $S(\pi,\pi)$ being the spin isotropic antiferromagnetic structure factor. Comparison of exact results (indicated by arrows) and the approximate $p = 0, 1, 2$ Lanczos iterations over the projected d-wave wavefunction for $L = 18$ (full triangles), $L = 50$ (full squares) and $L = 98$ (full circles). The extrapolated value of the order parameter is also shown, continuous lines are quadratic fit of the data. Inset: finite-size scaling with the variational wavefunction (empty circles) and with the variance extrapolated one (full circles).

It is remarkable that the variance extrapolation method can give exceptionally good results also for rather large lattice sizes. For the Heisenberg model, where there is no sign problem, it is possible to obtain the exact results, with arbitrary small statistical errors, both on the energy and on the correlation functions by using GFMC. In order to show the accuracy of the variance extrapolation we report in Fig. 2.3 the energy per site as a function of the variance for 18, 50 and 98 sites and $p = 0, 1, 2$. Much more impressive is the behavior of the antiferromagnetic order parameter as a function of the size of the lattice (Fig. 2.4). Although the variational wavefunction does not have magnetic long-range order, and the expectation value of the magnetic order parameter monotonically decreases by increasing the lattice size (see inset of Fig. 2.4), few Lanczos steps are enough to reproduce the magnetic correlations of the ground-state.

2.4.2 Improving the variational energy

We have seen that, by using (2.105) as the definition of the reference weights, the method is rigorously variational. However, the choice (2.80) gives a better reference dynamics because it allows us to improve self-consistently the amplitudes of the reference wavefunction. In this case $\Psi_n^{eff}(x) \neq \Psi_G(x)$ and the method is no longer variational. A compromise between the two cases is to introduce a parameter r that interpolate the two limits [87]

$$w_i^{eff'} = \frac{|w_i'|}{|r_{x_i'}|^{1-r}}. \tag{2.120}$$

In this case, the reference wavefunction $\Psi_n^{eff}(x)$ is not given by averaging the configurations with the weights w_i^{eff}: by using Eq. (2.95), $\Psi_n'(x) = r_x \Psi_n^{eff}(x)$, and Eq. (2.107), at equilibrium, we have that

$$\langle\langle w_i^{eff'} \delta_{x,x_i} \rangle\rangle = |r_x|^r \Psi^{eff}(x) \Psi_G(x) = \Psi_R(x) \Psi_G(x), \tag{2.121}$$

where $\Psi_R(x)\Psi_G(x)$ is the right eigenvector of the renormalized Green function

$$\bar{G}^r_{x',x} = |r_{x'}|^r \bar{G}^{var}_{x',x}. \tag{2.122}$$

From Eqs. (2.121) and (2.95), at equilibrium we obtain

$$\Psi^{eff}(x) = |r_x|^{-r} \Psi_R(x) \tag{2.123}$$

$$\Psi(x) = |r_x|^{1-r} \mathrm{sgn} r_x \Psi_R(x) = R_x \Psi_R(x), \tag{2.124}$$

and therefore the state $\Psi(x)$ is uniquely determined.

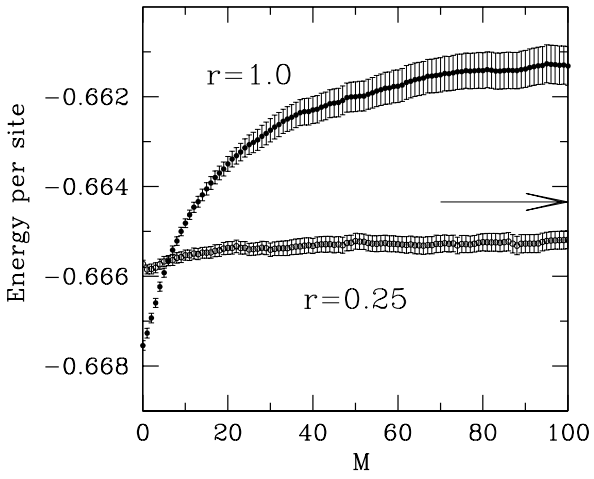

Figure 2.5: Energy per site for the $t-J$ model, 8 holes on a 8×8 lattice, $J=0.4t$ as a function of the number M of forward walking. The $r=0.25$ and $r=1.0$ cases are shown, the arrow indicate the result of $p=2$ Lanczos steps. The fixed-node approximation gives $E/L=-0.6560(1)$.

In order to compute the correlation function over the stochastic state $\Psi(x)$, it is necessary to use a slight generalization to non-symmetric matrices, of the forward walking technique. Indeed, for non-symmetric matrices, such as $\bar{G}^r_{x',x}$, the left eigenvector $\Psi_L(x)/\Psi_G(x)$ does not necessarily coincide with the right eigenvector $\Psi_R(x)\Psi_G(x)$. Since in the large number of walkers, the fluctuations of the parameters α_k are vanishingly small, it is convenient to implement the forward walking with fixed parameters α_k. The matrix $\bar{G}^r_{x',x}$ can be written in terms of a symmetric matrix $G^0_{x',x}$

$$\bar{G}^r_{x',x}=\frac{a_{x'}}{a_x}G^0_{x',x}, \tag{2.125}$$

where

$$a_x = \frac{|\Psi_G(x)|\,|r_x|^{r/2}}{\sqrt{z_x}} \tag{2.126}$$

$$G^0_{x',x} = \frac{|r_x|^{r/2}|r_{x'}|^{r/2}}{\sqrt{z_x z_{x'}}}|\Lambda\delta_{x,x'}-H_{x,x'}|. \tag{2.127}$$

The right and left eigenvectors of $\bar{G}^r_{x',x}$ are written in terms of the eigenvector $\phi_0(x)$ of $G^0_{x',x}$, namely $\Psi_R(x)\Psi_G(x)=a_x\phi_0(x)$ and $\Psi_L(x)/\Psi_G(x)=\phi_0(x)/a_x$. Then, it follows that the stochastic state $\Psi(x)$ can be written in terms of $\Psi_L(x)$

$$\Psi(x)=\frac{r_x}{z_x}\Psi_L(x)=L_x\Psi_L(x), \tag{2.128}$$

By applying several times the Green function $\bar{G}^r_{x',x}$, it is possible to filter out the state $\Psi_R(x)\Psi_G(x)$, then it is possible to evaluate the expectation value of any operator O by

propagating M times forward

$$\frac{\langle\Psi|O|\Psi\rangle}{\langle\Psi|\Psi\rangle} = \lim_{M\to\infty} \frac{\sum_{x,x',x''}(\bar{G}^r)^M_{x'',x'}\tilde{O}_{x',x}\Psi_R(x)\Psi_G(x)}{\sum_{x,x',x''}(\bar{G}^r)^M_{x'',x'}\tilde{I}_{x',x}\Psi_R(x)\Psi_G(x)}, \tag{2.129}$$

where the operators $\tilde{O}$ and $\tilde{I}$ are given by

$$\tilde{O}_{x',x} = \frac{\Psi_G(x')}{\Psi_G(x)} L_{x'} R_x O_{x',x} \tag{2.130}$$

$$\tilde{I}_{x',x} = L_x R_x \delta_{x',x}. \tag{2.131}$$

Therefore, contrary to the standard forward walking where $R_x = L_x = 1$ is satisfied, in this case slightly more involved matrix elements have to be considered. Indeed, by using the fact that $\sum_{x'}(\bar{G}^r)^M_{x',x} \sim \Psi_L(x)/\Psi_G(x)$, Eq. (2.129) is easily verified. Notice that also the denominator in Eq. (2.129) has to be forward propagated for M iterations, since in this case the diagonal elements of $\tilde{I}$ are not trivial. In particular, it is possible to consider $O = H$ and calculate the *variational* expectation value over the stochastic state $\Psi(x)$.

In Fig. 2.5, we report the energy as a function of the number M of forward walking for the $t-J$ model, 8 holes on a 8×8 lattice at $J = 0.4t$. The true energy expectation value ($M \to \infty$) can be much higher than the mixed average ($M = 0$) estimate, especially for $r \sim 1$ on large systems. The sizeable gain in energy by considering a small but finite r with respect to the case of $r = 0$ is due to the fact that, with $r > 0$, it is possible to strongly improve the amplitudes of the wavefunction. The $r > 0$ case can overcome, at least partially, the limitation of the few Lanczos step technique to be not size consistent, namely that in the thermodynamic limit the energy per site cannot be improved from the variational one. By contrast, for $r > 0$, the reference Green function is modified similarly to the FN case, and it is possible to obtain a size-consistent gain in energy [87].

Chapter 3

Phase separation

3.1 Introduction

One of the most debated issues in strongly correlated electron systems is the nature of the charge distribution in their ground-state. In particular, many authors have recently addressed the question of phase separation (PS) in the $t-J$ [54, 55, 56, 57, 58, 59, 60, 61, 62, 63] and in the Hubbard model [88, 89]. In the $t-J$ model, it is well accepted that for $J \gg t$ the holes tend to cluster together leaving the rest of the system in an undoped antiferromagnetic state. The main question is if this scenario persists down to small J's, or even to $J = 0$ [90]. Although most of the calculations lead to the conclusion that a finite critical value J_c of J below which the ground-state is homogeneous exists, it is not clear what this value is at low doping, with estimates ranging from $0.5t$ to $1.2t$. Moreover some authors [91] suggest that just before PS the ground-state has charge modulations, i.e. charge density waves.

As stated in Chapter 1, the simplest way to detect PS is by looking at the energy per hole

$$\epsilon(\delta) = \frac{e(\delta) - e(0)}{\delta}, \tag{3.1}$$

where $e(\delta)$ is the energy per site at hole doping δ and $e(0)$ is the energy per site at half-filling (Heisenberg model). In the thermodynamic limit, whereas for a stable system $\epsilon(\delta)$ is a concave function of δ, if the system phase-separates for densities up to $\delta = \delta_c$, $\epsilon(\delta)$ is a flat function for $\delta < \delta_c$. For finite systems, due to surface effects, $\epsilon(\delta)$ can be convex even for a stable system. Therefore, it is necessary to consider large enough lattices to wash out this spurious finite size effect. By using this approach with different quantum Monte Carlo techniques, many authors agree that the critical value of J is $J_c \sim 0.5t$ [57, 58, 59, 60]. By contrast Hellberg and Manousakis [61, 62], using a modified Green

function Monte Carlo (GFMC) technique, claim that the phase-separated state persists down to $J = 0$, that is the ground-state is unstable against PS at small hole doping for any interaction strength. The disagreement between these results is probably due to the fact that, in Refs. [61, 62], the delicate low-doping region is studied with fairly small clusters, introducing serious finite size effects. A completely different approach, the high-temperature expansion [55, 56], gives instead a stable ground-state up to $J_c \sim 1.2t$, but this method suffers from the difficulty of extrapolating the zero temperature limit from few coefficient series.

Recent density matrix renormalization group results support a different scenario. By performing the calculation on N-leg ladders, the value of $J_c \sim t$ in the two-dimensional case is found by extrapolating the value found at a fixed N for $N \to \infty$ [63]. Because of the growing of the Hilbert space when increasing N, the number of legs is limited to $4 \div 6$ and the large N limit is not well under control. Moreover, within the same approach, White and Scalapino proposed that the ground-state of the $t - J$ model has a charge density wave order in a wide range of dopings for $J \sim 0.4t$ [91]. This statement could be strongly affected by the choice of boundary conditions (periodic in one direction and open in the other) which might introduce uncontrolled finite size effects.

As far as the Hubbard model is concerned, little work has been done. Cosentini and co-workers [88], by calculating the energy per hole using the fixed-node method, found that there is a large region of PS in the phase diagram, at least for $U \geq 10t$. Their conclusions, however, are affected by the choice of the guiding wavefunction, which gives a very poor approximation near half-filling.

In this Chapter we present quantum Monte Carlo calculations for the Hubbard and the $t - J$ model. For the Hubbard model, the auxiliary-field quantum Monte Carlo (AFQMC) gives very accurate results in the weak- and intermediate-coupling regime, i.e. for $U \lesssim 4t$ [92]. AFQMC will then be used to assess the accuracy of our results also for sizes where the exact results by Lanczos diagonalization are not available. We will show that a study of the PS instability is very difficult using only energy calculation. Instead, a careful calculation of charge correlation functions

$$N(q) = \langle n_q n_{-q} \rangle = \frac{1}{L} \sum_{i,j} e^{iq(R_i - R_j)} \langle n_i n_j \rangle \tag{3.2}$$

gives a safer indication of the charge fluctuations. Moreover, the knowledge of $N(q)$ allows us to extract information about charge fluctuations for all the wavelengths, giving insight in favor of possible charge modulations. Within this approach, we are able to find an homogeneous ground-state for $U \lesssim 10t$.

For the $t-J$ model, the accuracy of the calculation is more difficult to assess compared to the Hubbard model, since there are no reliable methods for large sizes: the comparison with exact results is then limited to small clusters. We will report both energy and $N(q)$ calculations that support a scenario in which $J_c \sim 0.5t$.

3.2 The Hubbard Model

3.2.1 Variational wavefunction

We consider the Hubbard model on a square lattice of L sites with $N = N_\uparrow + N_\downarrow$ particles and $N_\uparrow = N_\downarrow$, $N_\uparrow$ ($N_\downarrow$) being the number of spin up (down) particles. The Hamiltonian reads:

$$H = -t \sum_{\langle i,j \rangle, \sigma} c^\dagger_{i,\sigma} c_{j,\sigma} + U \sum_i n_{i,\uparrow} n_{i,\downarrow}, \tag{3.3}$$

where $\langle\ \rangle$ stands for nearest neighbors, $c_{i,\sigma}$ ($c^\dagger_{i,\sigma}$) destroys (creates) an electron with spin σ at site i, and $n_{i,\sigma} = c^\dagger_{i,\sigma} c_{i,\sigma}$. In the following all energies are measured in units of t. In order to study PS as close as possible to half-filling using only closed-shell configurations, we consider square lattices tilted by 45° with $L^2 = 2l^2$ and l odd. In this way half-filling is a closed shell and the first doped closed shell has 8 holes independently on L.

In the presence of the sign-problem the choice of the guiding wavefunction is crucial. Our guiding wavefunction reads

$$|\Psi_G\rangle = \mathcal{P}_{S_z=0} \mathcal{P}_g \mathcal{J}_s |\mathcal{D}\rangle, \tag{3.4}$$

where $|\mathcal{D}\rangle$ is a Slater determinant in which the orbitals are suitably chosen (see below), $\mathcal{P}_{S_z=0}$ is the projector onto the subspace with $N_\uparrow = N_\downarrow$, i.e. with zero total spin component along the z-axis, $\mathcal{P}_g$ is a Gutzwiller operator that inhibits the double occupancies

$$\mathcal{P}_g = e^{-g \sum_i n_{i\uparrow} n_{i\downarrow}}, \tag{3.5}$$

where g is a variational parameter, and $\mathcal{J}_s$ is a Jastrow factor

$$\mathcal{J}_s = e^{\frac{\gamma}{2} \sum_{i,j} v_{i,j} S^z_i S^z_j}, \tag{3.6}$$

where γ is another variational parameter, and the $v_{i,j}$ are taken from the theory of spin-waves [93]. Some care must be taken in the choice of the orbitals appearing in the Slater determinant. The most common choice is to take the orbitals from an Hartree-Fock

approximation of the Hamiltonian breaking the SU(2) spin rotation symmetry along the z-axis.

$$H = -t \sum_{\langle i,j \rangle,\sigma} c^{\dagger}_{i,\sigma} c_{j,\sigma} + \frac{U}{2} \sum_{i,\sigma} \left[\langle n_i \rangle - \sigma (-1)^{R_i} \langle m_i \rangle \right] n_{i,\sigma}, \tag{3.7}$$

where

$$\langle n_i \rangle = \langle n_{i,\uparrow} \rangle + \langle n_{i,\downarrow} \rangle, \tag{3.8}$$

$$\langle m_i \rangle = (-1)^{R_i} \left[\langle n_{i,\uparrow} \rangle - \langle n_{i,\downarrow} \rangle \right]. \tag{3.9}$$

We consider only fillings which are closed shells for $U = 0$ and where a solution with constant density $\langle n_i \rangle = \frac{N}{L} = n$ and staggered magnetization $\langle m_i \rangle = m$ is found. In this case the Hartree-Fock many body wavefunction can be written as

$$|\mathcal{D}\rangle = \prod_{k}^{1,\ldots,N_{\uparrow}} \beta^{\dagger}_{k,\uparrow} \prod_{q}^{1,\ldots,N_{\downarrow}} \beta^{\dagger}_{q,\downarrow} |0\rangle, \tag{3.10}$$

where the quasi-particles have definite momentum modulo $Q = (\pi, \pi)$ and definite spin, since the antiferromagnetic order parameter is along the z-axis

$$\beta^{\dagger}_{k,\sigma} = v_k c^{\dagger}_{k,\sigma} + \sigma u_k c^{\dagger}_{k+Q,\sigma}, \tag{3.11}$$

k belongs to the reduced magnetic Brillouin zone, u_k and v_k are defined by:

$$u_k = \sqrt{\frac{1}{2}\left(1 + \frac{\epsilon_k}{\sqrt{\epsilon_k^2 + \Delta^2}}\right)} \tag{3.12}$$

$$v_k = \sqrt{\frac{1}{2}\left(1 - \frac{\epsilon_k}{\sqrt{\epsilon_k^2 + \Delta^2}}\right)}, \tag{3.13}$$

where $\epsilon_k = -2t \left(\cos k_x + \cos k_y\right)$ and $\Delta = \frac{Um}{2}$. It is worth noting that for $U/t \to \infty$ one has $u_k = v_k = \frac{1}{\sqrt{2}}$, namely the spin up and the spin down are in different sub-lattices (classical Néel state).

In a previous work [88] the wavefunction (3.4) with $|\mathcal{D}\rangle$ given by Eq. (3.10) has been found to be a rather poor approximation for large U/t at half-filling. In particular in this representation the Jastrow factor $\mathcal{J}_s$ does not play any important role.

We propose a new wavefunction which is a straightforward generalization of the one successfully used for the Heisenberg model [53]. The fundamental ingredient is to allow spin fluctuations perpendicular to the staggered magnetization. An easy implementation of this idea is to put the magnetization in the $x-y$ plane allowing transverse fluctuations

along the z-axis through a Jastrow-like factor [93]. This is achieved by a $\frac{\pi}{2}$ rotation $U_y(\frac{\pi}{2})$ around the y-axis of the canonical operators:

$$U_y^\dagger(\frac{\pi}{2})c_{i,\uparrow}^\dagger U_y(\frac{\pi}{2}) = \frac{1}{\sqrt{2}}\left(c_{i,\uparrow}^\dagger + c_{i,\downarrow}^\dagger\right) \tag{3.14}$$

$$U_y^\dagger(\frac{\pi}{2})c_{i,\downarrow}^\dagger U_y(\frac{\pi}{2}) = \frac{1}{\sqrt{2}}\left(c_{i,\uparrow}^\dagger - c_{i,\downarrow}^\dagger\right). \tag{3.15}$$

The fermionic part of our guiding wavefunction is therefore defined as a Slater determinant of the transformed orbitals

$$\beta_{k,+}^\dagger = U_y^\dagger(\frac{\pi}{2})\beta_{k,\uparrow}^\dagger U_y(\frac{\pi}{2}) \tag{3.16}$$

$$\beta_{k,-}^\dagger = U_y^\dagger(\frac{\pi}{2})\beta_{k,\downarrow}^\dagger U_y(\frac{\pi}{2}), \tag{3.17}$$

namely it is given by

$$|\mathcal{D}\rangle = \prod_k^{1,\ldots,N_\uparrow} \beta_{k,+}^\dagger \prod_q^{1,\ldots,N_\downarrow} \beta_{q,-}^\dagger |0\rangle. \tag{3.18}$$

Remarkably, for $U/t \to \infty$ and at half-filling, by construction the state (3.18) becomes the Néel state with spin quantization parallel to the x-axis, i.e. it has the correct Marshall sign on each of the 2^L configurations sampled by GFMC. In this limit it is also clear why the Jastrow factor may be much more effective: being defined along the z-axis, it allows us to sample the quantum fluctuation perpendicular to the staggered magnetization. In the previous case instead both the Jastrow quantization axis and the order parameter were parallel and for $U/t \to \infty$ there is no way to sample any fluctuation, the only possible configuration being the classical one.

An important systematic improvement of the wavefunction can be achieved by performing exactly one Lanczos step starting from $|\Psi_G\rangle$

$$|\Psi_L\rangle = (1 + \alpha H)\,|\Psi_G\rangle, \tag{3.19}$$

with α a variational parameter chosen to minimize the energy. This technique has been successfully used for the $t - J$ model both to improve the variational calculation [58] and as starting point for power methods [70]. Henceforth we will denote by VMC and LS the results obtained performing a variational Monte Carlo with the wavefunction (3.4) and (3.19), respectively. Analogously, the symbols FN and FNLS will indicate the fixed-node approximation applied to the wavefunction (3.4) and (3.19), respectively. Finally the symbol SR will indicate the (not variational) results obtained by stochastic reconfiguration applied to wavefunction (3.19).

U/t	$\|\mathcal{D}\rangle$	E_{ex}/L	E_{VMC}/L	E_{FN}/L	E_{LS}/L	E_{FNLS}/L
4	Eq. (3.10)	-0.9585	-0.9382(1)	-0.9514(1)	-0.9520(1)	-0.9556(1)
10	Eq. (3.10)	-0.4484	-0.4034(1)	-0.4284(1)	-0.4154(1)	-0.4316(1)
20	Eq. (3.10)	-0.2339	-0.2023(1)	-0.2195(1)	-0.2060(1)	-0.2225(1)
4	Eq. (3.18)	-0.9585	-0.9460(1)	-0.9547(1)	-0.9553(1)	-0.9576(1)
10	Eq. (3.18)	-0.4484	-0.4382(1)	-0.4451(1)	-0.4428(1)	-0.4470(1)
20	Eq. (3.18)	-0.2339	-0.2293(1)	-0.2232(1)	-0.2310(1)	-0.2337(1)

Table 3.1: Variational energies for 18 electrons on 18 sites as a function of U/t using (3.10) and (3.18) as Slater determinant.

U/t	E_{ex}/L	E_{VMC}/L	E_{FN}/L	E_{LS}/L	E_{FNLS}/L
4	-1.1299	-1.1124(1)	-1.1218(1)	-1.1229(1)	-1.1263(1)
10	-1.0193	-0.9749(1)	-1.0006(1)	-0.9997(1)	-1.0098(1)
20	-0.9598	-0.8983(1)	-0.9354(1)	-0.9253(1)	-0.9450(1)

Table 3.2: Variational energies for 10 electrons on 18 sites as a function of U/t.

In Table 3.1 and 3.2 we report the energies of 18 and 10 electrons on 18 sites, respectively. At half-filling we compare the results using (3.4) with the Slater determinant $|\mathcal{D}\rangle$ given by (3.10) and (3.18) for different approximations and values of U/t. Using (3.18) we obtain a sizeable improvement for large U's ($U \geq 10t$). Notice that for $U = 20t$ the best variational result with (3.10) is worse than the simple VMC with (3.18). For 10 electrons the two Slater determinants give the same results. Indeed for this doping the antiferromagnetic order is strongly suppressed and the Jastrow factor $\mathcal{J}_s$ does not play any important role.

3.2.2 Results

In order to show that the energy calculations may overestimate the tendency to a PS instability, it is important to compare the GFMC results with some exact reference. Previous studies on the Hubbard model have shown that it is important to consider relatively large lattice sizes since finite size effects favor PS [79]. At $U = 0$ and half-filling there is a large density of states at the Fermi level, this huge degeneracy being only slightly removed by a small Coulomb interaction. It turns out that the energy per hole is almost constant up to the first closed shell, i.e. for $\delta \sim 1/L$, giving rise to an unphysical and spurious PS [79]. We need therefore a reference result for large lattices, where exact diagonalizations are not available. In the case of the Hubbard model for $U \lesssim 4t$

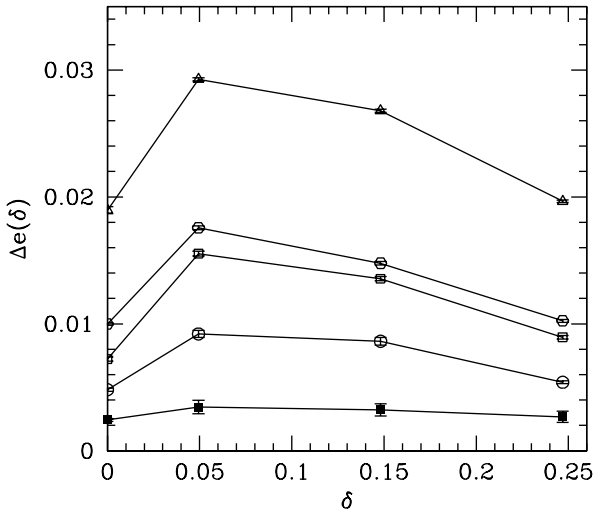

Figure 3.1: Relative accuracy of various GFMC techniques with respect to AFQMC for a 162-site lattice with $U = 4t$ as a function of filling δ. From top to bottom VMC (empty triangles), FN (empty hexagons), LS (empty squares), FNLS (empty circles), SR (full squares). Lines are guides to the eye.

the AFQMC is almost exact and represents the reference we need. Unfortunately, the AFQMC suffers from very large fluctuations for larger values of the Hubbard interaction U and no useful informations can be obtained with this method for $U \sim 10t$. Therefore, the GFMC plays a fundamental role in studying the strong coupling regime of the Hubbard model.

In Fig. 3.1 we show the accuracy of the GFMC results obtained with different approximations compared with the AFQMC ones for a 162-site lattice and $U = 4t$. For this coupling value AFQMC does not provide evidence for PS. We plot $\Delta e(\delta) = [e(\delta) - e_{AFQMC}(\delta)]/e_{AFQMC}(\delta)$, where $e(\delta)$ and $e_{AFQMC}(\delta)$ are the energies per site of GFMC and AFQMC respectively for a doping δ. Besides the improvement in the absolute accuracy, the curves get flatter and flatter improving the approximation, but only the SR accuracy is almost doping independent. In other words, we need a really accurate calculation to wash out the spurious dependence of the variational energy upon doping. Even for the best variational method, the FNLS, although the accuracy on the energy is for all dopings less than 1%, the difference in accuracy between, for example, the half-filled case and the first closed shell is still sizeable. This difference is very important, because it represents just the energy scale determining or ruling out PS.

In Fig. 3.2 the function $\epsilon(\delta)$ is shown for FN, FNLS, SR, and AFQMC methods. We need to use SR to exclude the occurrence of PS, where even the FNLS data would imply PS. The reason for this disappointing situation is that all the known variational meth-

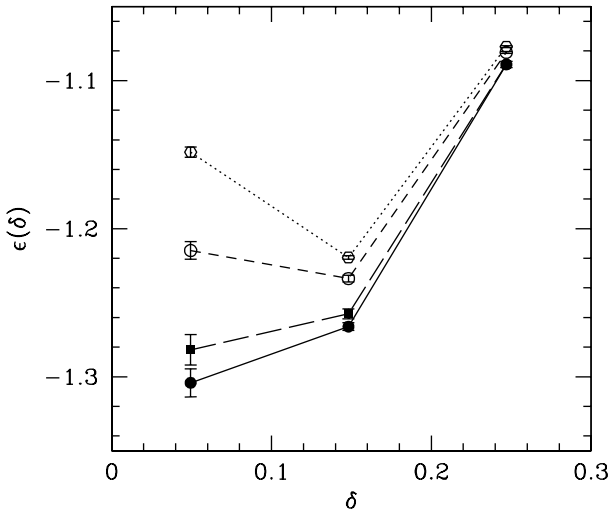

Figure 3.2: Energy per hole $\epsilon(\delta)$ for a 162-site lattice with $U = 4t$. From top to bottom FN (empty hexagons), FNLS (empty circles), SR (full squares) , and AFQMC (full circles). Lines are guides to the eye.

ods are still too dependent on the guiding wavefunction. As evidenced by the previous analysis, the resolution in energy necessary to detect or rule out PS is very hard to be reached with statistical methods, especially for large U/t.

On the other hand, GFMC methods have proven to be reliable not only for energy calculations but also for correlation functions like $N(q)$ [60]. For a phase-separated system there are strong fluctuations in the density for small momenta: $N(q \to 0)$ is expected to be strongly enhanced for small momenta, that is for $|q| \sim \frac{2\pi}{\xi}$, ξ being the characteristic length of the phase-separated region. Moreover if the compressibility χ diverges also $N(q \to 0)$ diverges yielding an alternative tool to probe PS.

The GFMC study of $N(q)$ turns out to be reliable, since it is based on a single calculation for a given doping value, whereas the evaluation using $\epsilon(\delta)$ involves a comparison between energies obtained by different simulations for different fillings, with corresponding guiding wavefunction having different accuracies. Moreover from $N(q)$ it is also possible to extract information about charge fluctuations at finite q's, related to charge density waves, and therefore the knowledge of $N(q)$ allows us to have more general results with respect to the simple study of $\epsilon(\delta)$.

We computed the density structure factor $N(q)$ by means of the forward-walking technique, within the FNLS approximation, at half-filling and for the first few closed-shell configurations on a 162 and a 98-site lattice. The evaluation of density-density correlation function is in principle possible even within SR by numerical differentiation of the energy with respect to an external field coupled to $N(q)$. However this approach

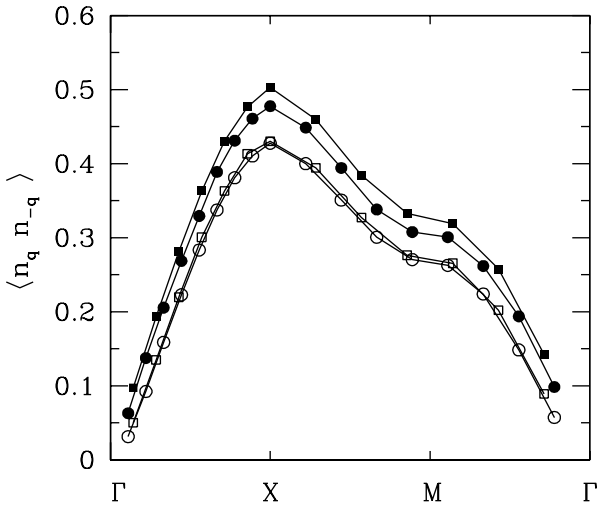

Figure 3.3: FNLS results of $N(q)$ for $U = 4t$, 162 electrons on 162 sites (empty circles), 98 electron on 98 sites (empty squares), 154 electrons on 162 sites (full circles) and 90 electrons on 98 sites (full squares). Lines are guides to the eye and error-bars are smaller than points. $\Gamma = (0,0)$, $X = (\pi,\pi)$, $M = (\pi,0)$.

$U = 4t$	q	FNLS	EXACT	$U = 10t$	q	FNLS	EXACT
	$(3,3)$	0.2117(1)	0.2106		$(3,3)$	0.0448(1)	0.0456
	$(6,6)$	0.4151(1)	0.4144		$(6,6)$	0.1164(1)	0.1176
	$(9,9)$	0.5310(1)	0.5283		$(9,9)$	0.1491(1)	0.1503
	$(6,0)$	0.2806(1)	0.2806		$(6,0)$	0.0647(1)	0.0658
	$(9,3)$	0.3616(1)	0.3613		$(9,3)$	0.0997(1)	0.1010

Table 3.3: Density-density correlation function $N(q)$ for 18 electrons on 18-site lattice in the Hubbard model. Momenta are in unit of $2\pi/18$.

is very demanding and does not give a significant improvement to the FNLS results, which are very accurate. In Table 3.3 we report the density-density correlation function for $U = 4t$ and $U = 10t$ at half-filling on a 18-site lattice. Furthermore, it is found that even in a larger system the FNLS provides a very accurate result: for 90 electrons on the 98-site lattice, the FNLS gives $N(q) = 0.097(1)$ for the smallest q-point, i.e. $q = (2\pi/7, 2\pi/7)$, whereas the AFQMC gives $N(q) = 0.0932(2)$. It is worth noting that the value of FNLS is slightly greater than the one of AFQMC, implying that the FNLS tends to overestimate the tendency towards PS.

In Fig. 3.3 $N(q)$ is shown for $U = 4t$ at half-filling for a 162-site and a 98-site lattices and for 154 electrons on a 162-site lattice and 90 electrons on a 98-site lattice. No sign of divergence, and consequently of PS or charge density waves, is seen in the data. We

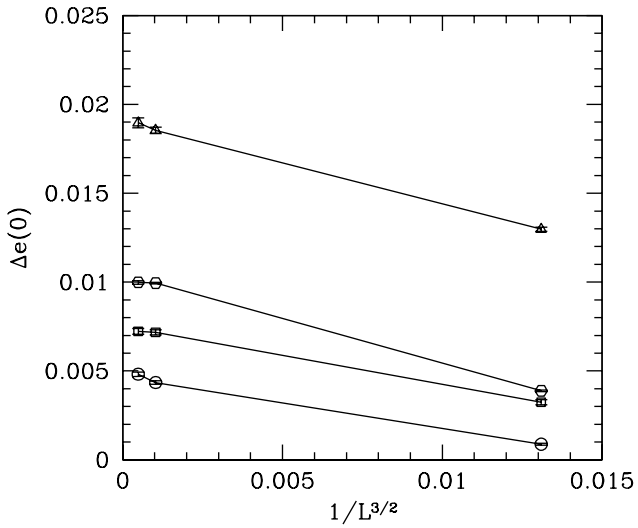

Figure 3.4: Relative accuracy of various GFMC techniques with respect to AFQMC for different lattices ($L = 18, 98, 162$) and $U = 4t$. From top to bottom VMC (empty triangles), FN (empty hexagons), LS (empty squares), FNLS (empty circles). Lines are guides to the eye.

also notice that the two sets of points for the half-filled systems lie on the same curve, showing that we have substantially reached the thermodynamic limit. For this value of U, $N(q)$ is essentially featureless for all dopings we considered, suggesting that there are no charge instabilities at any finite length. The smallest doping we considered is $\delta \simeq 0.049$ and we cannot exclude that for smaller dopings PS or charge density waves are present.

In order to investigate smaller dopings we should consider larger lattices. Unfortunately the accuracy of the approximations considered decreases when increasing the size of the system and the 162-site lattice represents the largest lattice where the accuracy is acceptable. In Fig. 3.4 we report $\Delta e(0)$ for various sizes and for different approximations: from the 18 sites to the 162 sites the accuracy of FNLS changes from less than 0.1% to about 0.5%. These indications prevent us from considering sizes larger than the ones presented in this thesis.

Now we turn to larger Coulomb interactions and consider $U = 10t$, where the AFQMC results are not reliable due to large fluctuations. In principle GFMC techniques do not suffer from intrinsic limitations in the large coupling regime and it is possible to consider any value of U. In practice we need an accurate knowledge of the nodes, i.e. an accurate guiding wavefunction. Our choice, Eq. (3.4) with orbitals given by Eqs. (3.16) and (3.17), is a very good approximation for the half-filling case. In Table 3.1 we report the energies for various methods for 18 electrons on 18 sites at different U's. Although

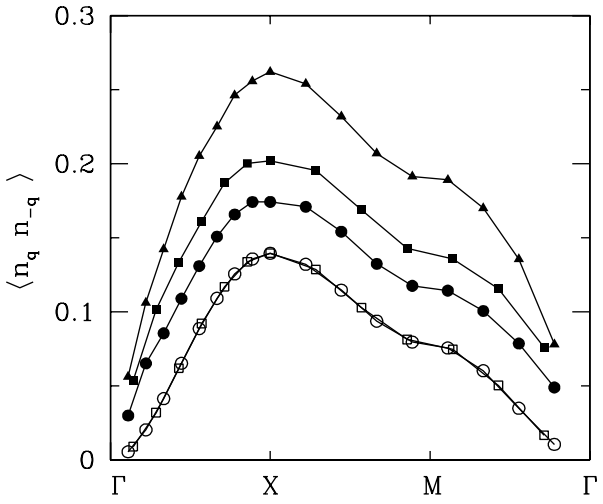

Figure 3.5: FNLS results of $N(q)$ for $U = 10t$, 162 electrons on 162 sites (empty circles), 98 electrons on 98 sites (empty squares), 154 electrons on 162 sites (full circles), 90 electrons on 98 sites (full squares), and 138 electrons on 162 sites (full triangles). Lines are guides to the eye and error-bars are smaller than points. $\Gamma = (0,0)$, $X = (\pi,\pi)$, $M = (\pi,0)$.

all the approximations are quite size dependent, the wavefunction becomes more and more accurate by increasing the Coulomb potential. Therefore we expect that it also gives a good starting point at least close to half-filling.

We present results for $U = 10t$, for which previous FN calculations based on $\epsilon(\delta)$ and a less accurate wavefunction [88] have shown PS up to $\delta \simeq 0.15$. Indeed if we use $\epsilon(\delta)$ as a probe for PS we find that the phase diagram shows a large instability region, confirming the results of Ref. [88]. As for the $U = 4t$ case, this instability is very likely to be a spurious effect: a consequence of the different energy accuracy for different dopings. This possibility, that cannot be proved without knowing the exact energies at strong coupling, is instead very clearly supported by the calculation of the charge correlation functions.

Fig. 3.5 displays $N(q)$ for the same fillings of Fig. 3.3 and for 138 electrons on the 162-site lattice, which corresponds to $\delta \simeq 0.148$. All the correlation functions are definitely non-divergent for $q \to 0$ and are qualitatively similar to the $U = 4t$ case, indicating that the system is far away from a PS instability. Furthermore $N(q)$ does not show peaks at any finite momenta for this Coulomb interaction.

3.2.3 Conclusions

An extensive GFMC analysis of the Hubbard model at low hole doping has been carried out. In particular we have focused on the possible instability of the model with respect to PS and charge density waves. Comparing GFMC results with AFQMC ones in the weak coupling region ($U = 4t$), we show that detecting PS by means of energy results requires a very accurate calculation at all electronic densities. Indeed the accuracy of the energy is strongly dependent on the electron density, and the signature of PS based only on energy calculations is clearly affected by this bias, leading to a spurious region of PS instability. In the case of the Hubbard model this is particularly relevant because, while we are able to give a very good description of the half-filled case, in which the ground-state is an antiferromagnetic insulator, we are not aware of equally accurate descriptions of the doped state. Even for $U = 4t$ it is necessary to use the really accurate SR and AFQMC technique to eliminate the doping dependence of the accuracy and to rule out PS.

On the other hand, PS and charge density waves instabilities can be probed more easily using density-density correlation functions. This approach has various advantages. First, it is found that $N(q)$ has very small size effects and the thermodynamic limit is reached with about 100 sites. Second, the information contained in $N(q)$ does not depend on different densities, implying that a different accuracy as a function of doping does not introduce any external bias.

Instead of using energy calculations, which are very expensive at moderate and large U's, we calculate the charge correlation functions and we are able to find clear evidence for the absence of PS up to $U = 10t$ in the low-doping regime.

3.3 The $t - J$ Model

3.3.1 Variational wavefunction

As in the case of the Hubbard model, we consider the $t - J$ model on a 45° tilted square lattice of L sites with $L^2 = 2l^2$ (l odd) and $N = N_\uparrow + N_\downarrow$ particles, $N_\uparrow = N_\downarrow$. In order to compare the quantum Monte Carlo results with exact results by Lanczos diagonalization, we report also calculations for a $L = 26$ lattice.

The $t - J$ Hamiltonian reads:

$$H = -t \sum_{\langle i,j \rangle, \sigma} \tilde{c}^\dagger_{i,\sigma} \tilde{c}_{j,\sigma} + J \sum_{\langle i,j \rangle} \left(\mathbf{S}_i \cdot \mathbf{S}_j - \frac{1}{4} n_i n_j \right), \tag{3.20}$$

where $\tilde{c}^{\dagger}_{i,\sigma} = c^{\dagger}_{i,\sigma}(1-n_{i,\bar{\sigma}})$, $n_i = \sum_{\sigma} n_{i,\sigma}$ is the electron density on site i, $\mathbf{S}_i = \sum_{\sigma,\sigma'} \tilde{c}^{\dagger}_{i,\sigma} \tau_{\sigma,\sigma'} \tilde{c}_{i,\sigma'}$ is the spin operator and $\tau_{\sigma,\sigma'}$ are Pauli matrices.

As pointed out by Gros [68], a very good variational wavefunction in the low-doping regime is given by the projected d-wave BCS state

$$|\Psi^N_{RVB}\rangle = \mathcal{P}_N \mathcal{P} \prod_k \left(1 + f_k c^{\dagger}_{k,\uparrow} c^{\dagger}_{-k,\downarrow}\right) |0\rangle, \tag{3.21}$$

where $\mathcal{P}_N$ projects onto the subspace of N particles, $\mathcal{P}$ is the Gutzwiller projector, which completely forbids doubly occupied sites, and f_k is the pair amplitude given by

$$f_k = \frac{\Delta_k}{\xi_k + \sqrt{\xi_k^2 + \Delta_k^2}}, \tag{3.22}$$

with $\Delta_k = \Delta(\cos k_x - \cos k_y)$, $\xi_k = -2t(\cos k_x + \cos k_y) - \mu$, Δ being a variational parameter and μ the chemical potential.

The non-projected wavefunction (3.21) can be obtained as the ground-state of the mean-field Hamiltonian

$$H = \sum_k \xi_k c^{\dagger}_{k,\sigma} c_{k,\sigma} + \sum_k \left[\Delta_k c^{\dagger}_{k,\uparrow} c^{\dagger}_{-k,\downarrow} + H.c.\right]. \tag{3.23}$$

It is worth noting that f_k is highly singular for a d-wave superconducting order parameter: it diverges along the diagonal directions for $\xi_k < 0$, i.e. inside the bare electronic Fermi surface. Therefore it comes out that the wavefunction (3.21) is ill-defined on every finite cluster containing k-points along the diagonal direction. In order to avoid these singularities, it is useful to perform a particle-hole transformation on down-spin

$$d_i = (-1)^{R_i} c^{\dagger}_{i,\downarrow} \tag{3.24}$$

$$c_i = c_{i,\uparrow}. \tag{3.25}$$

After this transformation, the average number of electron N is related to the difference between c and d particles as follows

$$N = L + \sum_i \left(\langle c^{\dagger}_i c_i\rangle - \langle d^{\dagger}_i d_i\rangle\right), \tag{3.26}$$

whereas the average magnetization is given by

$$M = \sum_i \left(\langle c^{\dagger}_{i,\uparrow} c_{i,\uparrow}\rangle - \langle c^{\dagger}_{i,\downarrow} c_{i,\downarrow}\rangle\right) = -L + \sum_i \left(\langle c^{\dagger}_i c_i\rangle + \langle d^{\dagger}_i d_i\rangle\right). \tag{3.27}$$

We can easily solve Eqs. (3.26) and (3.27) and obtain, in the subspace with zero magnetization:

$$\sum_i \langle c_i^\dagger c_i \rangle = \frac{N}{2} \tag{3.28}$$

$$\sum_i \langle d_i^\dagger d_i \rangle = L - \frac{N}{2}. \tag{3.29}$$

After the particle-hole transformation, the wavefunction (3.21) can be written as

$$|\Psi_{RVB}^N\rangle = \tilde{\mathcal{P}}_N \tilde{\mathcal{P}} \prod_k \left(u_k d_{k+Q}^\dagger + v_k c_k^\dagger \right) |\tilde{0}\rangle, \tag{3.30}$$

where $\tilde{\mathcal{P}}_N$ and $\tilde{\mathcal{P}}$ are the particle-hole transformed projectors $\mathcal{P}_N$ and $\mathcal{P}$, respectively.

$$u_k = \sqrt{\frac{1}{2}\left(1 + \frac{\xi_k}{\sqrt{\xi_k^2 + \Delta_k^2}}\right)} \tag{3.31}$$

$$v_k = \sqrt{\frac{1}{2}\left(1 - \frac{\xi_k}{\sqrt{\xi_k^2 + \Delta_k^2}}\right)}, \tag{3.32}$$

and $|\tilde{0}\rangle$ is the vacuum of c and d particles, i.e. $c_k|\tilde{0}\rangle = d_k|\tilde{0}\rangle = 0$, defined by $|\tilde{0}\rangle = \prod_k d_k^\dagger |0\rangle$. In this case the singular points are occupied by the particles. It is worth noting that, if the magnetization is zero, the system is always at half-filling.

In order to improve our variational and guiding wavefunction, we add to the wavefunction (3.21) a density-density Jastrow factor [94]

$$\mathcal{J} = e^{\frac{\gamma}{2}\sum_{i,j} v_{i,j} n_i n_j}, \tag{3.33}$$

with γ variational parameter. Therefore our wavefunction reads

$$|\Psi_G\rangle = \mathcal{J}|\Psi_{RVB}^N\rangle. \tag{3.34}$$

The accuracy of the wavefunction can be improved further by performing one Lanczos step:

$$|\Psi_L\rangle = (1 + \alpha H)\,|\Psi_G\rangle, \tag{3.35}$$

where α is a free parameter chosen to minimize the energy.

It is worth noting that, although for the $t - J$ model the projected d-wave BCS wavefunction with a spin-rotationally invariant density-density Jastrow factor represents a very accurate variational state, for the Hubbard model at small and intermediate coupling ($U \lesssim 10t$) the best choice for the variational and guiding wavefunction is given by

J/t	E_{ex}/L	E_{VMC}/L	E_{FN}/L	E_{LS}/L	E_{FNLS}/L
0.2	-0.57413	-0.5380(1)	-0.5550(1)	-0.5605(1)	-0.5654(1)
0.3	-0.64262	-0.6128(1)	-0.6271(1)	-0.6328(1)	-0.6365(1)
0.4	-0.71437	-0.6883(1)	-0.7007(1)	-0.7065(1)	-0.7096(1)
0.5	-0.78812	-0.7640(1)	-0.7754(1)	-0.7811(1)	-0.7839(1)
0.6	-0.86337	-0.8400(1)	-0.8510(1)	-0.8567(1)	-0.8594(1)

Table 3.4: Variational energies for 22 electrons on 26 sites as a function of J/t.

J/t	E_{ex}/L	E_{VMC}/L	E_{FN}/L	E_{LS}/L	E_{FNLS}/L
0.2	-0.40956	-0.3895(1)	-0.3997(1)	-0.4028(1)	-0.4058(1)
0.3	-0.50097	-0.4826(1)	-0.4921(1)	-0.4951(1)	-0.4981(1)
0.4	-0.59452	-0.5761(1)	-0.5860(1)	-0.5887(1)	-0.5918(1)
0.5	-0.68945	-0.6698(1)	-0.6807(1)	-0.6833(1)	-0.6867(1)
0.6	-0.78537	-0.7638(1)	-0.7763(1)	-0.7787(1)	-0.7826(1)

Table 3.5: Variational energies for 24 electrons on 26 sites as a function of J/t.

a Jastrow-Slater determinant with rotated orbitals (3.16) and (3.17). Indeed, although the projected d-wave BCS wavefunction is a singlet and does not break the SU(2) symmetry, it has a very poor variational energy for the Hubbard model. The quality of the variational energy obtained with our Jastrow-Slater determinant remains considerably better than the BCS one at half-filling and $U \lesssim 10t$ even when the accuracy of the approximation is improved by the GFMC. Instead, in the doped case, the BCS wavefunction with GFMC is only slightly worse than the corresponding Jastrow-Slater determinant proposed in Section 3.2.1. This may suggest that antiferromagnetism is already suppressed at small finite doping and d-wave superconductivity is a possible stable phase especially at large U/t.

In Table 3.4 and 3.5 we report the energies 22 and 24 electrons on 26 sites, where the exact result is known by Lanczos diagonalization, for different approximations. As for the case of the Hubbard model, we indicate with VMC and LS the results obtained with the wavefunction (3.34) and (3.35), respectively, using Variational Monte Carlo. The symbols FN and FNLS will indicate the results obtained with fixed-node approximation applied to wavefunction (3.34) and (3.35) respectively. Finally, the symbol SR will indicate the results obtained with stochastic reconfiguration applied to wavefunction (3.34).

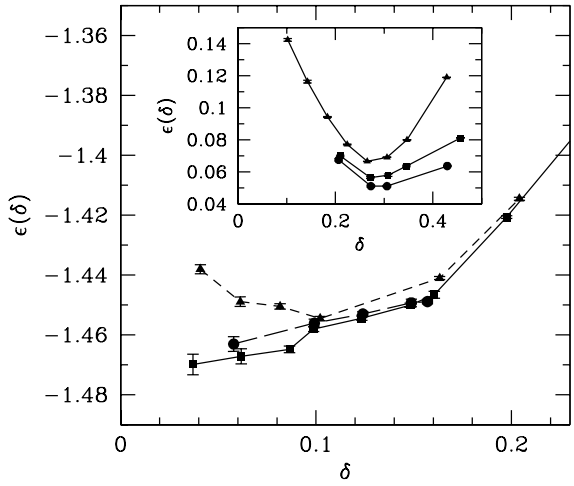

Figure 3.6: Energy per hole $\epsilon(\delta)$ within the FN approximation for 98-site (triangles), 162-site (squares) and 242-site lattice (circles), $J = 0.4t$. Inset: the same for $J = t$. Lines are guides to the eye.

3.3.2 Results

In this Section we show the result for the energy per hole and the density-density correlation function $N(q)$ for the $t - J$ model. Contrary to the case of the Hubbard model, for the $t - J$ model there are no accurate reference results for large lattice sizes, and therefore it is not possible to perform a comparison with an almost exact solution on large lattices. Assuming that the guiding wavefunction (3.21) is size consistent, i.e. that its accuracy does not depend too much on the system size, the same accuracy obtained on small lattice can be achieved also on larger cluster. In Fig. 3.6 we report the energy per hole calculation for $J = 0.4t$ within the FN approximation: the inset shows the case of $J = t$. The two cases are qualitatively different: for $J = 0.4t$ the minimum at finite doping, present in the 98-site lattice, disappears when larger sizes are considered (162 and 242 sites), suggesting that for this value of the antiferromagnetic coupling there is no PS for the infinite system. We believe that the occurrence of PS at $J = 0.4t$ and 98 sites is an artifact of the FN approximation on small sizes and the minimum in $\epsilon(\delta)$ no longer occurs in the thermodynamic limit. Instead, for $J = t$ the finite doping minimum in $\epsilon(\delta)$ is almost size independent, suggesting that, for this value of J, a true phase-separated state is present. On the other hand for $J = 0.4t$, a different insight in favor of a uniform ground-state comes from the SR method. In Fig. 3.7 it is reported the case of 50-site and 98-site lattice: although for the smallest cluster even the SR technique gives a minimum in the energy per hole, for the 98-site lattice the SR recovers a uniform ground-state.

As for the Hubbard model, in order to detect the charge inhomogeneities of the

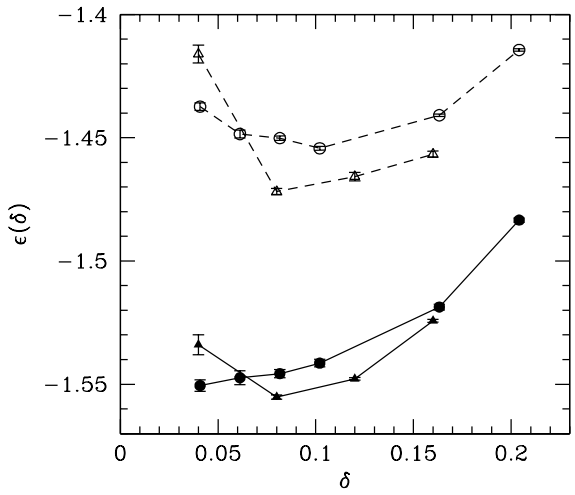

Figure 3.7: Energy per hole $\epsilon(\delta)$ for 50-site (triangles) and 98-site lattice (circles). FN results are connected by dashed lines and SR by continuous lines.

ground-state it is better to look at the density-density correlation function. We computed the density structure factor $N(q)$ by means of the forward-walking technique, within the FN approximation for few dopings near half-filling on a 98 and a 162-site lattice. In Fig. 3.8 $N(q)$ is shown for $J = 0.4t$ for a 98-site cluster and different dopings. The peak at $q \to 0$, near half-filling, progressively disappears by increasing the doping. At $\delta \sim 0.1$, a considerable peak at finite momenta is present, indicating a possible charge modulation.

In order to investigate more deeply the region near half-filling, we consider a 162-site lattice for 152 and 146 electrons, see Fig. 3.9. These two fillings give hole concentrations similar to the ones of the 98-site cluster. In this case, for both dopings, a clear peak at small, but finite, momenta is present. There are two possible interpretations of these results. The first one is that the thermodynamic limit is reached with about 100 sites, therefore the $N(q)$ results for the two clusters should lie on the same curve. This is especially the case for the smaller doping, where the two electron fillings give very similar densities. Because the q-points in the two lattices are slightly different, these results suggest that there is a very narrow peak at finite small momenta. The second possibility is that the 98-site system is too small to detect the finite-q charge modulation present in the larger 162-site lattice.

It is very important to note that the peak in $N(q)$ is a genuine feature of the ground-state of the $t - J$ model: indeed it is not present at a pure VMC level, and it is extremely important to use many power iterations to generate it, see Fig. 3.10.

It is worth noting that, at small doping, the shape of the density-density correlation

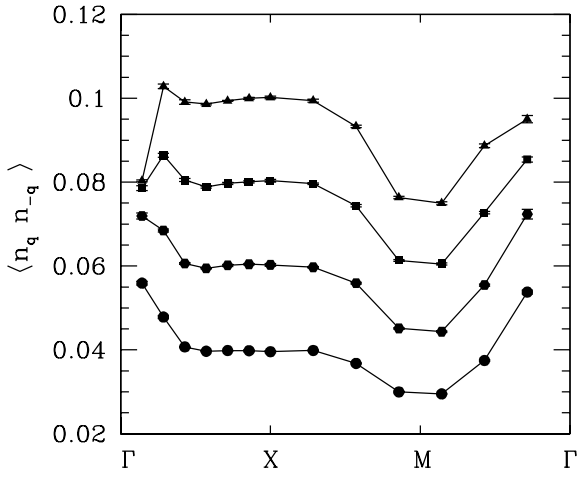

Figure 3.8: N(q) for $J = 0.4t$ and 98 sites by using FN approximation. From top to bottom: 88 (triangles), 90 (squares), 92 (hexagons), 94 (circles) electrons. Lines are guides to the eye. $\Gamma = (0,0)$, $X = (\pi,\pi)$, $M = (\pi,0)$.

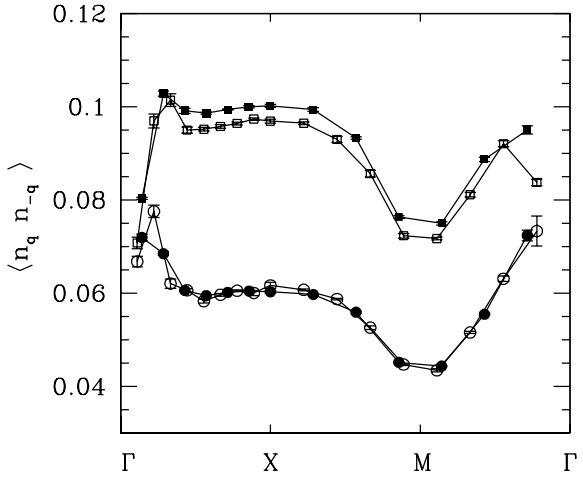

Figure 3.9: N(q) for $J = 0.4t$, 98 and 162 sites by using FN approximation. From top to bottom: 88 electrons on 98 sites (full squares) and 146 electrons on 162 sites (empty squares), and 92 electrons on 98 sites (full circles) and 152 electrons on 162 sites (empty circles). Lines are guides to the eye. $\Gamma = (0,0)$, $X = (\pi,\pi)$, $M = (\pi,0)$.

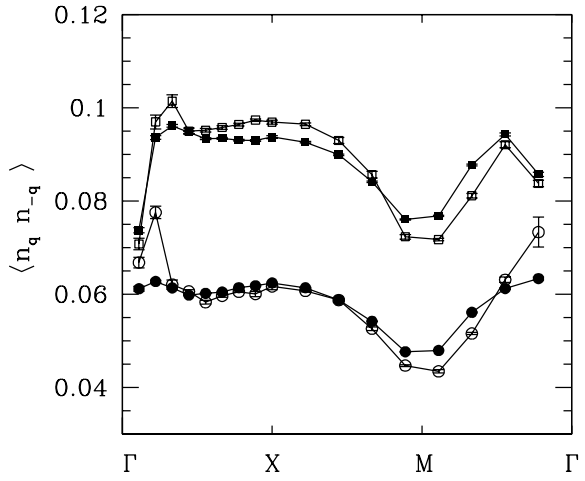

Figure 3.10: Comparison between the N(q) calculated by VMC and by FN for $J = 0.4t$ and 162 sites. From top to bottom: 146 electrons by VMC (full squares) and by FN (empty squares), and 152 electrons by VMC (full circles) and by FN (empty circles). Lines are guides to the eye. $\Gamma = (0, 0)$, $X = (\pi, \pi)$, $M = (\pi, 0)$.

function for the $t - J$ model at $J = 0.4t$ is quite different from the one of the Hubbard model at $U = 10t$. Indeed, whereas in the Hubbard model no signature of charge modulations are present in $N(q)$, in the $t - J$ model a considerable peak at small momenta is present even at rather large doping, $\delta \sim 0.1$. This disagreement is perhaps due to the fact that the $t - J$ model completely forbids doubly occupied sites. In Table 3.6 we report the $N(q)$ calculation for the Hubbard and the $t - J$ model for 16 electrons on a small 18-site lattice by exact Lanczos diagonalization. Even in this case there are some quantitative difference, but if we project out all the states with at least one site doubly occupied from the ground-state of the Hubbard model, the density-density correlations over this state look much more similar to the ones of the $t - J$ model.

In order to clarify the question of PS in the $t - J$ model, it is necessary to perform the same kind of calculation for different antiferromagnetic couplings J. Indeed, the density-density correlation function is found to be much less size dependent than the energy per hole, and therefore the PS instability can be studied in a much safer way with this kind of method. In Fig. 3.11 and 3.12 we show the $N(q)$ for $J = 0.2t$ and $J = 0.6t$, respectively. In the $J = 0.2t$ case, a finite peak at finite momenta is present, although it is sensibly smaller than the corresponding peak at $J = 0.4t$. Moreover, as soon as the doping is increased, every feature at small momenta disappears indicating that the density becomes almost uniform.

The situation is completely different for $J = 0.6t$ where a huge peak in the density-density correlations is present close to the Γ point, both in the 98 and in the 162-site

J/t	$q=(3,3)$	$q=(6,6)$	$q=(9,9)$	$q=(6,0)$	$q=(9,3)$
0.4	0.1104	0.1089	0.1101	0.0959	0.1016
0.2	0.0996	0.1100	0.1108	0.1005	0.1065
0.1	0.0951	0.1104	0.1110	0.1029	0.1083
U/t					
10	0.1349	0.2085	0.2448	0.1510	0.1865
20	0.1065	0.1376	0.1499	0.1145	0.1290
40	0.0974	0.1172	0.1211	0.1060	0.1136
40	0.0955	0.1102	0.1110	0.1029	0.1080

Table 3.6: Exact ground-state values for the density-density correlation function $N(q)$ for 16 electrons on 18-site lattice in the Hubbard and $t-J$ model by Lanczos diagonalization. The value of $N(q)$ on the ground-state of the Hubbard model, having projected out all the states with at least one site doubly occupied, is also reported in the last row for $U=40t$. Momenta are in unit of $2\pi/18$.

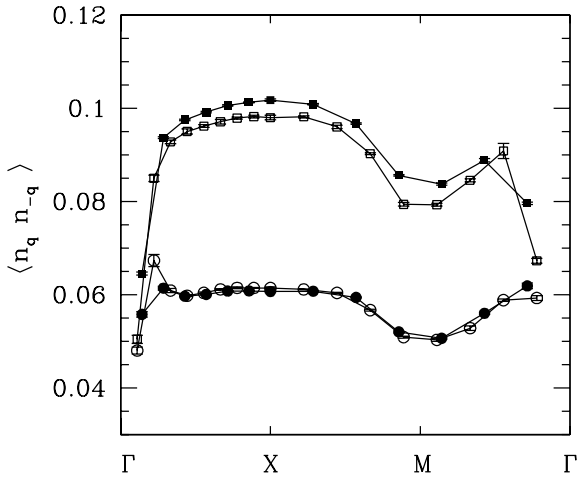

Figure 3.11: N(q) for $J=0.2t$, 98 and 162 sites by using FN approximation. From top to bottom: 88 electrons on 98 sites (full squares) and 146 electrons on 162 sites (empty squares), and 92 electrons on 98 sites (full circles) and 152 electrons on 162 sites (empty circles). Lines are guides to the eye. $\Gamma=(0,0)$, $X=(\pi,\pi)$, $M=(\pi,0)$.

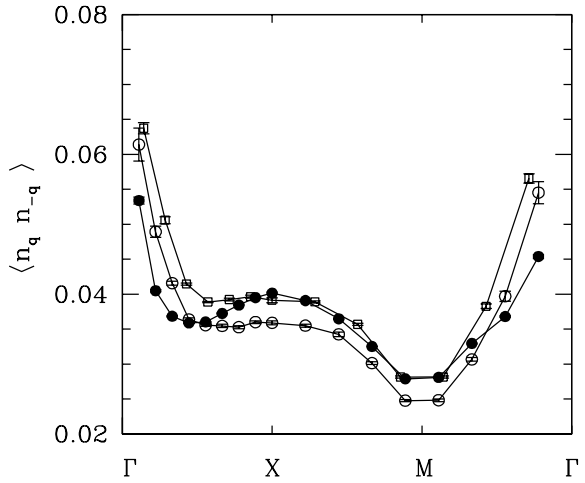

Figure 3.12: N(q) for $J = 0.6t$, 98 and 162 sites by using FN approximation. 94 electrons on 98 sites (empty squares) and 156 electrons on 162 sites (empty circles). The VMC calculation for 156 electrons on 162 sites is also reported (full circles). Lines are guides to the eye. $\Gamma = (0,0)$, $X = (\pi,\pi)$, $M = (\pi,0)$.

system, as shown in Fig. 3.12. Away from the Γ point the behavior of $N(q)$ is almost featureless and does not show any finite-q peak.

The boundary of PS instability found looking at $N(q)$ agrees very well with the one found looking at the energy per hole. In Fig. 3.13, the energy per hole is plotted for $J = 0.6t$ for 50 and 98 sites, using the SR approximation. For this value of the antiferromagnetic coupling, the behavior of $\epsilon(\delta)$ is rather different from the one of $J = 0.4t$. Indeed the minimum in the energy per hole is present both in the 50 and in the 98-site system, and, although it is less marked by increasing the size, its position is almost size-independent.

Our results on the $t-J$ model are in good quantitative agreement with other quantum Monte Carlo calculations [57, 58, 59], and, although it is not possible to rule out the possibility that PS takes place very close to half-filling, it is safe to conclude that no PS occurs for $J \lesssim 0.4t$ and $\delta \gtrsim 0.05$. This statement would be in disagreement with a recent calculation by Hellberg and Manousakis [61, 62], who claim that PS occurs at all interaction strengths. The main problem with Refs. [61, 62] is that, instead of working at fixed lattice and varying the number of particles, in order to change the doping, the size of the lattice is changed, keeping fixed the number of electrons. In this way, the delicate low-doping region is studied only with exceedingly small lattices. Therefore the energy per hole suffers of huge size effects and it is not at all representative of the thermodynamic limit.

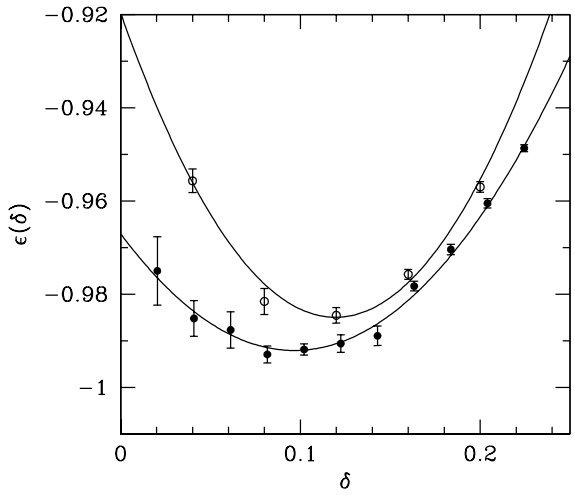

Figure 3.13: Energy per hole $\epsilon(\delta)$ for 50-site (empty circles) and 98-site lattice (full circles) by using the SR approximation, $J = 0.6t$. Lines are guides to the eye.

3.3.3 Conclusions

In this Section we performed an extensive study of the charge fluctuations in the $t - J$ model at low doping and for different antiferromagnetic couplings. Although both the energy per hole and the density-density correlation function calculations give a consistent boundary for the PS instability, we believe that the second method has much less size dependence and gives a more reliable tool to look at the long-wavelength instability. Moreover, it also gives information about finite-q charge modulations, that cannot be detected with the energy per hole only. A clear qualitative difference in $N(q)$ at small momenta for $J = 0.2 \div 0.4t$ and $J = 0.6t$ strongly suggests that the onset of PS is at $J_c \sim 0.5t$.

Even though at small couplings J the ground-state is not phase-separated, at least for $\delta \gtrsim 0.05$, there is clear evidence of some charge modulations with long wavelengths. These findings could support density matrix renormalization group calculations on rectangular lattices [91], although within this method clearer evidence of a true striped phase is found. Indeed, the charge fluctuations at small J's can be easily pinned by the open boundary conditions chosen along one of the direction of the rectangular cluster. In order to gain kinetic energy the system tends to expel the holes from the boundaries, favoring a pinned charge modulation.

It is worth noting that, even for $J = 0.4t$, the analysis of the energy per hole gives a very large compressibility, suggesting that, even though the ground-state is not phase-separated, the system is strongly susceptible and it is expected that a further small attractive interaction can drive the system towards a charge instability.

Chapter 4

Superconductivity and stripes in the $t - J$ model

4.1 Introduction

The theory of superconductivity developed by Bardeen, Cooper and Schrieffer (BCS) [24, 25] was founded on a number of assumptions which, on the basis of experiments, were generally accepted. In particular, the experimental evidence pointed to the fact that, in the transition of a metal to the superconducting state, the lattice and its properties were essentially unchanged, whereas the properties of the conduction electrons were changed drastically. The early attempts suggested that a theory based upon the independent-particle model of conduction electrons did not have the possibility of explaining the fundamental properties of superconductors. Thus the simplest model which seemed capable of explaining superconductivity was that of a gas of electrons interacting with each other through some two-particle interaction. The question of what specific interaction is responsible for superconductivity has been considered over a long period. When the Coulomb interaction between electrons was little understood, it was thought that the long-range part of this force could bring about the correlations that seemed necessary to explain superconductivity. However, Bohm and Pines [95] showed that the long-range part of the Coulomb potential is connected with the collective oscillation of the electrons (the plasma mode) which, because of its high frequency character, can weakly affect the low-energy superconducting phase. The difficulty in finding the right interaction is due to the small energy change between the normal and the superconducting states. Despite this difficulty, Fröhlich [96] proposed that the attraction which drives to the superconducting state arises as a result of the interaction of electrons with

the lattice vibrations, e.g. with phonons. Its significance in causing superconductivity is confirmed by the dependence of the critical temperature on the isotopic mass of the lattice.

A fundamental step toward the understanding of superconductivity was made by Cooper [97], who showed that the Fermi sea is unstable to the formation of bound pairs for an arbitrary small attractive interaction. He solved the problem of two particles interacting through an attractive potential $-V < 0$ in the presence of the Fermi sea, and demonstrated that they bind with an energy given by

$$E = -2\hbar\omega_D e^{-\frac{2}{N(0)V}}, \tag{4.1}$$

where $N(0)$ is the density of states at the Fermi level and $\hbar\omega_D$ is an energy cutoff. In particular ω_D is the frequency of the phonons which mediate the attractive interaction between particles.

The Cooper argument suggests that in the presence of an attractive interaction the normal state of a free electron gas is unstable. This argument is only suggestive, but it laid the foundations for the BCS theory. Assuming that, below the transition temperature, electrons of opposite spin and momentum condensate into bound states, Bardeen, Cooper and Schrieffer proposed that the wavefunction describing the superconducting state is

$$|\Phi_{BCS}\rangle = \prod_k \left(u_k + v_k c^\dagger_{k,\uparrow} c^\dagger_{-k,\downarrow}\right)|0\rangle, \tag{4.2}$$

where u_k and v_k are variational parameters.

In the presence of a small attractive interaction between electrons near the Fermi energy, it is possible to show [25] that the superconducting state energy E_{SC} is lower than the normal state E_N one

$$E_{SC} - E_N = -\frac{N(0)\Delta^2(0)}{2}, \tag{4.3}$$

where

$$\Delta(0) = 2\hbar\omega_D e^{-\frac{2}{N(0)V}} \tag{4.4}$$

is the zero-temperature gap which opens at the Fermi level in the superconducting state. In the low-temperature superconductors, described by the BCS theory, the gap does not depend on the momentum k, i.e. it opens isotropically over the Fermi surface. In this simple approach, the critical temperature T_c is related to the gap $\Delta(0)$ by

$$\Delta(0) = 1.75 k_B T_c. \tag{4.5}$$

The superconducting gap can be considered as the order parameter for the superconducting transition. Indeed, at finite temperatures the value of the gap decreases and eventually vanishes for $T > T_c$

$$\Delta(T) \sim \left(1 - \frac{T}{T_c}\right)^{\frac{1}{2}}. \tag{4.6}$$

The discovery of high-temperature superconductors has renewed the discussion of unconventional, i.e. non-phononic, pairing mechanisms in solids. Indeed, although phonon exchange [98] could explain transition temperatures around 30 K, as required for $\mathrm{La_{2-x}Sr_xCuO_4}$, it is more difficult to believe that it can be responsible for superconductivity above 90 K, as attained in $\mathrm{YBa_2Cu_3O_{9-x}}$. Moreover, besides the high critical temperature itself, the anomalous properties described in Chapter 1 have led to consider novel mechanisms for the superconducting instability.

One of the most striking features of the cuprate superconductors, and related insulating materials such as Neodymium doped compounds, is a strong evidence of dynamic and static ordering of spins and charges, which, for example, shows up as incommensurate peaks in low-energy neutron diffraction measurements [9, 39]. In an early work, Tranquada and co-workers [9], found a clear evidence of *static and incommensurate* charge and spin order in $\mathrm{La_{1.6-x}Nd_{0.4}Sr_xCuO_4}$ with $\mathrm{x} \sim \frac{1}{8}$. They argue that, although bulk superconductivity is absent in this material, their results are relevant also for superconducting samples.

Indeed, also in the superconducting $\mathrm{La_{2-x}Sr_xCuO_4}$, there is increasing evidence of dynamical magnetic and stripe correlations [10] from neutron and X-ray scattering measurements. The low-energy magnetic scattering, which is characterized by the antiferromagnetic wavevector $Q = (\pi, \pi)$ at low doping, shifts to positions $q_s = (\pi \pm 2\pi\epsilon, \pi)$ and $q_s = (\pi, \pi \pm 2\pi\epsilon)$, with ϵ proportional to the hole doping, i.e. $\epsilon \sim \mathrm{x}$. Moreover, peaks revealing charge ordering at $q_c = (\pm 4\pi\epsilon, 0)$ and $q_c = (0, \pm 4\pi\epsilon)$ are also found. The relation between q_c and q_s implies that the periodicity of the spins is twice the periodicity of charge: in Fig. 4.1 the case of $\mathrm{x} = \frac{1}{8}$ is reported. This hole density is often considered a "magic" filling, at which the charge and spin correlations are strongest and presumably locked by the tilt distortion of the underlying lattice [9]. Indeed, neutron and X-ray scattering measurements on $\mathrm{La_{1.6-x}Nd_{0.4}Sr_xCuO_4}$ show that the charge and magnetic ordering temperatures reach their maximum at $\mathrm{x} \sim \frac{1}{8}$, where the superconducting temperature has an anomalous suppression. Moreover, a similar suppression in the superconducting temperature is also observed in Barium based compounds, $\mathrm{La_{2-x}Ba_xCuO_4}$, for the same hole doping $\mathrm{x} \sim \frac{1}{8}$. This effect has attracted the attention of many authors and the major controversy regards the issue of whether

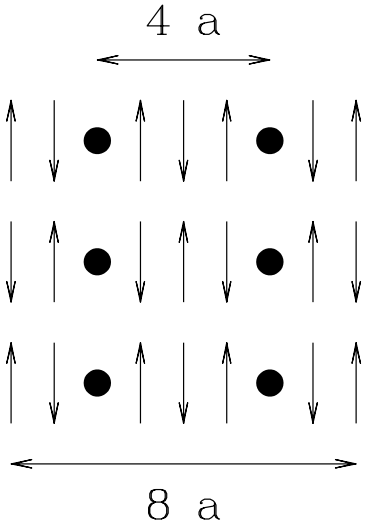

Figure 4.1: Idealized diagram of the spin and charge stripe pattern in a $\mathrm{CuO_2}$ plane of hole doped $\mathrm{La_{2-x}Sr_xCuO_4}$ with $\mathrm{x} = \frac{1}{8}$. Arrows indicate spins and circles indicate holes and a is the $\mathrm{Cu-Cu}$ lattice spacing. The hole stripes are half-filled, i.e. there is only one half of a hole per Cu site.

this mesoscopic self-organization of charges and spins is a necessary precursor for high-temperature superconductivity [99, 100] or whether it is simply an alternative instability that competes with superconductivity [73].

It is worth noting that, within a simple Hartree-Fock approach it is not possible to predict half-filled stripes, and only stripes with one hole per site, corresponding to $\epsilon = \frac{x}{2}$, are found [101]. Therefore a strong-coupling approach, which can treat more properly the local hole correlations, is needed. By using the density matrix renormalization group method on the $t-J$ model, White and Scalapino claimed that, for a wide range of dopings, the ground-state has stripe-like correlations and, in particular, at $J = 0.35t$ and hole doping $\delta = \frac{1}{8}$, they reproduced the half-filled stripes of Fig. 4.1 [91]. This result has stimulated much work in order to understand the stability of this kind of solution against the change of lattice shape, boundary conditions, interaction strength and electron doping. In general, the hole motion at finite doping, frustrates the antiferromagnetic alignment of the spins present at half-filling, and the strong electronic interaction may drive the system towards phase-separation [54, 61], superconductivity [58, 72], charge density waves or stripes [91], or to some exotic non-Fermi liquid phase, e.g. flux phases [102]. Therefore the scenario presented by the $t-J$ model is far to be understood and it is still an open question if this simple model containing only purely electronic correlations is able to describe the anomalous properties found in the underdoped region of the high-temperature superconductors.

In this Chapter we present Monte Carlo calculations of the superconducting order parameter for the $t-J$ model (3.20) at finite doping. Furthermore, in the last Section we report the density-density and spin-spin structure factor for two different lattice shapes, i.e. square and rectangular, in order to study the dependence of the charge and spin peaks on boundary conditions.

4.2 Small lattice calculations

In this Section we show the accuracy of the variance extrapolation method described in Section 2.4.1 on a small $L = 18$ sites, where exact results are available. The variational wavefunction is the one described in Section 3.3.1

$$|\Psi_{RVB}^{N}\rangle = \mathcal{P}_N \mathcal{P} \mathcal{J} \prod_k \left(1 + f_k c_{k,\uparrow}^{\dagger} c_{-k,\downarrow}^{\dagger}\right) |0\rangle, \tag{4.7}$$

where $\mathcal{P}_N$ is the projector onto the subspace of N particles, $\mathcal{P}$ is the Gutzwiller projector, which forbids doubly occupied sites, $\mathcal{J}$ is a density-density Jastrow factor (3.33), and f_k is defined by Eq. (3.22).

As stated in Section 3.3.1, the unprojected wavefunction (4.7) can be obtained as the ground-state of the mean-field Hamiltonian

$$H = \sum_k \xi_k c_{k,\sigma}^{\dagger} c_{k,\sigma} + \frac{\Delta}{2}\left(\hat{\Delta}^{\dagger} + \hat{\Delta}\right) \tag{4.8}$$

$$\hat{\Delta}^{\dagger} = \sum_{\langle i,j \rangle} M_{i,j}\left(c_{i,\uparrow}^{\dagger} c_{j,\downarrow}^{\dagger} + c_{j,\uparrow}^{\dagger} c_{i,\downarrow}^{\dagger}\right), \tag{4.9}$$

where $\xi_k = -2t\left(\cos k_x + \cos k_y\right) - \mu$, μ being the chemical potential, $\hat{\Delta}^{\dagger}$ creates all possible nearest-neighbor singlet bonds with d-wave symmetry, being $M_{i,j} = +1$ or -1 if the bond $\langle i,j \rangle$ is in the x or y direction, respectively.

Our main task is to compute the anomalous order parameter at finite system size

$$P_d = \frac{1}{L} \frac{\langle \Psi_p^{N+2} | \hat{\Delta}^{\dagger} | \Psi_p^{N} \rangle}{\sqrt{\langle \Psi_p^{N+2} | \Psi_p^{N+2} \rangle \langle \Psi_p^{N} | \Psi_p^{N} \rangle}}, \tag{4.10}$$

where $|\Psi_p^N\rangle$ and $|\Psi_p^{N+2}\rangle$ are the states with N and $N+2$ electrons, respectively, and p is the number of Lanczos steps applied onto the wavefunction (4.7). If P_d is finite in the thermodynamic limit this necessarily implies off-diagonal long-range order in the ground state. Following Refs. [72, 103], it is convenient with an approximate technique

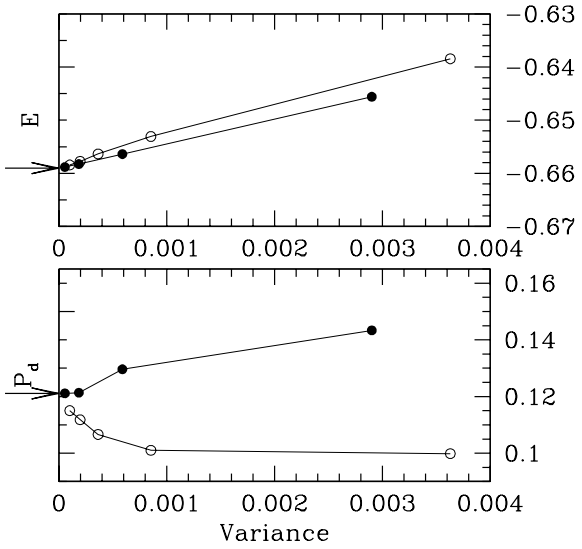

Figure 4.2: Variational energy (upper panel) and d-wave order parameter P_d (lower panel) as a function of the variance obtained by applying exactly p Lanczos steps to the variational wavefunction of Eq. (4.7). Full dots (optimal Δ), empty dots ($\Delta = 0$). $L = 18$, $N = 16$ and $J = 0.4t$

to calculate a short-range quantity like P_d, instead of the more conventional long-range expectation value

$$C = \frac{1}{L^2} \frac{\langle \Psi_p^N | \hat{\Delta} \hat{\Delta}^\dagger | \Psi_p^N \rangle}{\langle \Psi_p^N | \Psi_p^N \rangle}. \tag{4.11}$$

It is worth noting that, because of the constraint of no doubly occupied sites, the superconducting order parameter P_d, at small hole densities, is proportional to the number of holes and not to the number of electrons as in models of weakly correlated electrons. Therefore, in order to decide if the $t-J$ model has a superconducting ground-state or not, it makes no sense to compare the value of P_d in the $t-J$ model with the corresponding one in a free-electron model, as it is done in Ref. [71].

In Table 4.1 we show a comparison between the variance extrapolation method and the exact results for 18 and 16 electrons at $J = 0.4t$. In Table 4.2 we show P_d as a function of the number of Lanczos step iterations for the 18-site cluster at $J = 0.4t$. In the same Table we have computed also the variance σ^2, the overlap squared

$$Z_p = |\langle \Psi_p | \Phi_0 \rangle|^2, \tag{4.12}$$

of the wavefunction $|\Psi_p\rangle$ with the true ground state $|\Phi_0\rangle$, and the average sign of the $|\Psi_p\rangle$ wavefunction:

$$\langle S_p \rangle = \sum_x |\langle x | \Phi_0 \rangle|^2 \mathrm{Sgn}\left(\langle x | \Psi_p \rangle \langle x | \Phi_0 \rangle \right), \tag{4.13}$$

N	Δ	p	E/L	P_d	E_{ex}/L	P_d^{exact}
18	0.55	1	-0.4765(1)		-0.47668	
18	0.55	2	-0.4775(1)		-0.47749	
16	0.20	1	-0.6541(1)	0.1074(4)	-0.65420	0.10730
16	0.55	2	-0.6583(1)	0.122(1)	-0.65826	0.12135

Table 4.1: Comparison between the estimates of the ground-state energy per site E/L and of the d-wave order parameter P_d obtained with the exact and the statistical application of p Lanczos steps on the variational wavefunction of Eq. (4.7). Δ is the variational parameter of the mean-field Hamiltonian (4.8), $L = 18$, $N = 16, 18$ and $J = 0.4t$.

where $|x\rangle$ denotes configurations with definite electron positions and spins. For an exact calculation, namely $p >> 1$, both $Z_p \to 1$ and $S_p \to 1$, whereas $\sigma^2 \to 0$. The variance thus represents a very important tool to estimate the 'distance' from the exact ground state when the latter is not known. In particular, whenever $Z_p \simeq 1$ the energy approaches the exact result linearly with the variance σ^2, allowing us to estimate the error in the variational energy.

This can be achieved by plotting the variational energies as a function of the corresponding variance σ^2, and performing a linear or quadratic fit to the $\sigma = 0$ exact limit (see Fig. 4.2). Similar fits can be attempted for correlation functions though, in this case, a term $\propto \sqrt{\sigma^2}$ is also expected for $\sigma^2 \to 0$. This term is however negligible for quantities like P_d that are averaged bulk correlation functions in a large system size (see the Appendix C). In practice even in the small 18-site cluster the non-linear term turns out to be negligible (see Fig. 4.2). We believe that, being the convergence of the Lanczos algorithm particularly well behaved and certainly unbiased, the variance extrapolation method is in this case particularly useful and reliable. However for bad initial wavefunction (e.g., randomly generated) or very large sizes the approach to zero of the variance may behave rather wildly, requiring many Lanczos steps to reach the regime where the extrapolation is possible.

As shown in Table 4.2 the quality of the variational wavefunction (4.7) is exceptionally good, especially in the doped case with $N = 16$. Here Z_p is larger than 0.9 even at the simplest $p = 0$ variational level, and is drastically improved with very few Lanczos step iterations. Remarkable is also the behavior of the average sign S_p which measures directly the accuracy of the BCS wavefunction phases, without caring about the amplitudes. In the undoped case the signs of the wavefunction $\langle S_0 \rangle$ can be proven to be exact, i.e., $\langle S_0 \rangle = 1$, having the state (4.7) the well-known Marshall signs, i.e.,

N	Δ	p	$\langle S_p \rangle$	Z_p	σ^2	E/L
18	0.00	0	1.0000	0.6898	1.194	-0.43833
16	0.00	0	0.9656	0.8306	1.174	-0.63847
18	0.80	0	1.0000	0.8850	0.335	-0.46639
18	0.80	1	1.0000	0.9915	0.042	-0.47662
18	0.80	2	1.0000	0.9995	0.004	-0.47752
18	0.80	3	1.0000	1.0000	0.0003	-0.47759
18	0.80	4	1.0000	1.0000	0.00002	-0.47759
18	0.80	∞	1.0000	1.0000	0.0	-0.47759
16	0.55	0	0.9891	0.9260	0.940	-0.64559
16	0.55	1	0.9988	0.9814	0.191	-0.65638
16	0.55	2	0.9999	0.9942	0.060	-0.65826
16	0.55	3	1.0000	0.9983	0.018	-0.65882
16	0.55	4	1.0000	0.9995	0.005	-0.65898
16	0.55	5	1.0000	0.9999	0.002	-0.65902
16	0.55	6	1.0000	0.9999	0.0005	-0.65904
16	0.55	7	1.0000	1.0000	0.0001	-0.65904
16	0.55	∞	1.0000	1.0000	0.0	-0.65904

Table 4.2: Average sign $\langle S_p \rangle$, overlap squared on the exact ground-state Z_p and variance σ^2 obtained applying exactly p Lanczos steps on the variational wavefunction of Eq. (4.7). $L = 18$, $N = 16, 18$ and $J = 0.4t$.

the phases of the exact ground state of the Heisenberg model (see Appendix D). For the two-hole case, the nodes change in a non trivial way. Nevertheless, $\langle S_0 \rangle$ remains very close to 1 and it is much higher than the average sign of the corresponding Gutzwiller wavefunction ($\Delta = 0$), also shown in the Table for comparison.

These results suggest that there is a tendency to d-wave pairing in the $t - J$ model at doping $\delta \sim 0.1$ and $J \sim 0.4t$, and that the wavefunction (4.7) is a particularly accurate wavefunction to describe the small and even zero doping region of the $t - J$ model.

4.3 Superconducting order parameter

In order to confirm the results found on the small 18-site lattice, we compute in this Section the anomalous order parameter P_d on larger size systems, by using variational Monte Carlo with few Lanczos steps. In the variational approach, it is easy to calculate the quantity

$$P_d^+ = \frac{1}{L} \frac{\langle \Psi_p^{N+2} | \hat{\Delta}^\dagger | \Psi_p^N \rangle}{\langle \Psi_p^N | \Psi_p^N \rangle}. \tag{4.14}$$

Hence in order to have the value of the normalized order parameter P_d, it is necessary to perform a second simulation at $N + 2$ particles in which the quantity

$$P_d^- = \frac{1}{L} \frac{\langle \Psi_p^N | \hat{\Delta} | \Psi_p^{N+2} \rangle}{\langle \Psi_p^{N+2} | \Psi_p^{N+2} \rangle} \tag{4.15}$$

is calculated. Then, the product of the two variational calculations yields the square of the desired quantity

$$P_d = \sqrt{P_d^+ \times P_d^-}. \tag{4.16}$$

In Figs. 4.3 and 4.4 we show the results for the energy and the d-wave order parameter P_d for $p = 0, 1, 2$ Lanczos steps for 4 and 8 holes on the 50-site lattice, respectively. The starting variational wavefunction is chosen to have the best possible variational energy within the class described by Eq. 4.7. It turns out that the energy extrapolation is very stable and each Lanczos step improves by a factor of two both the variance and the energy accuracy, giving rise to a very accurate value of the extrapolated energy, $E/L = -0.5982(3)$ and $E/L = -0.7203(4)$ for 4 and 8 holes, respectively.

For small lattice sizes, the extrapolated value of the energy does not depend on the particular ansatz of the starting wavefunction, and it is possible to obtain an accurate value of the ground-state energy starting both from a metallic state, with $\Delta = 0$, and from a superconducting state, with a finite Δ (see Fig. 4.2). Indeed, for small clusters,

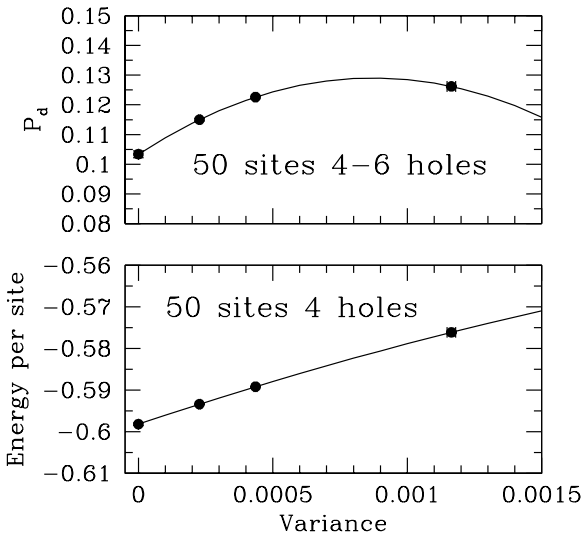

Figure 4.3: Variational energy (lower panel) and d-wave order parameter P_d (upper panel) as a function of the variance obtained by applying exactly $p = 0, 1, 2$ Lanczos steps to the variational wavefunction of Eq. (4.7). The extrapolated values of the energy and P_d are also shown. $L = 50$ and $J = 0.4t$

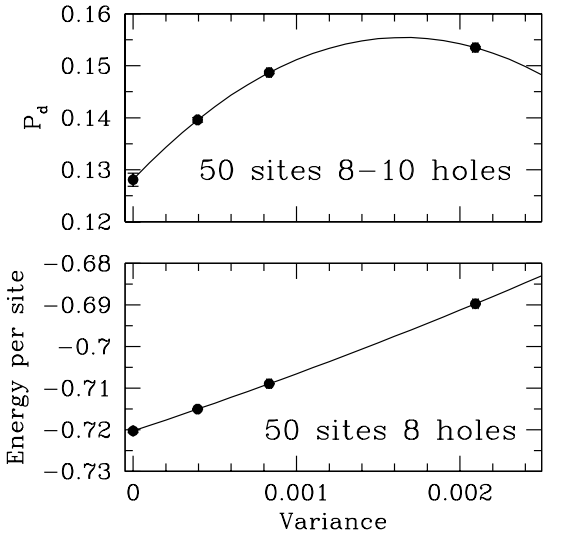

Figure 4.4: Variational energy (lower panel) and d-wave order parameter P_d (upper panel) as a function of the variance obtained by applying exactly $p = 0, 1, 2$ Lanczos steps to the variational wavefunction of Eq. (4.7). The extrapolated values of the energy and P_d are also shown. $L = 50$ and $J = 0.4t$

there is a large gap between the ground-state and the first excited state, and the Lanczos algorithm converges to the ground-state in few steps. By contrast, on large size systems, the choice of the starting wavefunction is a crucial point to obtain an accurate value of the ground-state energy. Indeed, although the Lanczos technique always converges to the lowest eigenstate, it is not obvious that few iterations are enough to obtain a good approximation of the ground-state. The variance vanishes for all the eigenstates of the Hamiltonian, and, with only few Lanczos steps, it is possible to remain stuck in a local minimum and converge to an excited state. The convergence to the lowest energy state is guaranteed only if the starting wavefunction has a large overlap with the ground-state. By increasing the size of the system this overlap goes to zero, and in order to converge to the ground-state, it is necessary to perform more and more Lanczos iterations. Therefore, it is interesting to compare the results obtained by starting from different wavefunctions. In particular, we can consider the optimal variational wavefunction, with a sizeable $\Delta \sim 0.2 \div 0.8$, and the wavefunction with $\Delta = 0$, which describes a correlated metal, without superconducting long-range order. At high densities of holes, the two states have almost the same energy, and even the extrapolated values coincide within the statistical errors. In the lower panel of Fig. 4.5, we report the variational energies for the case of 20 holes on 50 sites (in this case the optimal variational wavefunction has $\Delta \sim 0.2$). The fact that the two different wavefunctions converge to the same extrapolated energy suggests that this value of the energy accurately represents the true ground-state energy for this doping. In the low-doping region, for 4 holes, even if the $p = 0, 1, 2$ energies for the optimal variational wavefunction are lower than the corresponding ones of the metallic wavefunction, the extrapolated energies of the two wavefunctions coincide within the statistical errors, see Fig. 4.6. In this case, as shown in the inset of Fig. 4.6, the magnetic order parameter is almost independent from p for the optimal wavefunction, whereas it sensibly grows, by increasing p, for the metallic wavefunction, the difference between the two being only 1%. It appears that, in the low-doping region, the ground-state has short-range antiferromagnetic order, and its structure can be recovered from both the wavefunctions, which have almost the same structure. In this doping region, both the wavefunction with a finite Δ and the metallic one with $\Delta = 0$, appear to converge to the same (magnetically ordered) state by means of few Lanczos iterations.

When a symmetry breaking occurs, on large clusters, it is not possible to change the overall structure of the starting wavefunction by the application of only few Lanczos steps, as clearly suggested for the case of 8 holes on 50 sites, shown in the upper panel of Fig. 4.5. This failure in the convergence of the few Lanczos steps algorithm

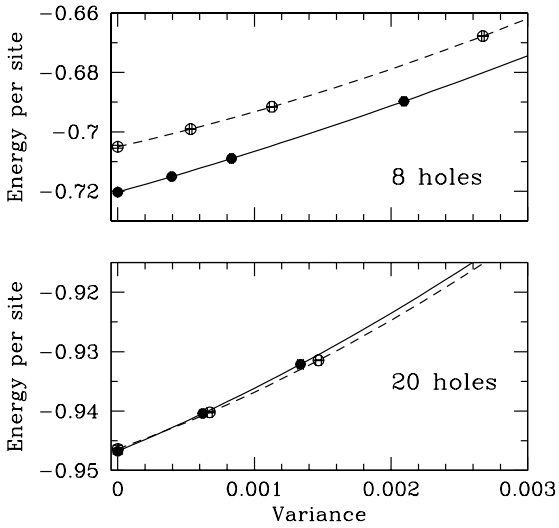

Figure 4.5: Variational energies as a function of the variance obtained by applying $p = 0, 1, 2$ Lanczos steps to the wavefunction of Eq. (4.7) on a 50-site lattice for $J = 0.4t$. Full dots (continuous line) correspond to the optimal Δ, empty dots (dashed line) to $\Delta = 0$, for $N = 30$ (lower panel) and $N = 42$ (upper panel). The extrapolated value of the energy is also shown.

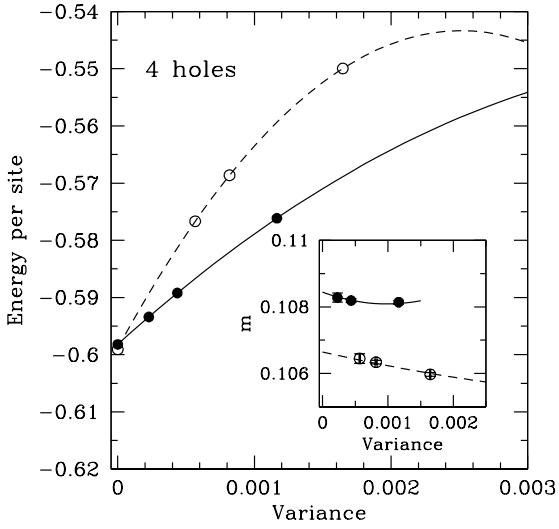

Figure 4.6: Variational energies as a function of the variance obtained by applying $p = 0, 1, 2$ Lanczos steps to the wavefunction of Eq. (4.7) on a 50-site lattice for $J = 0.4t$. Full dots (continuous line) correspond to the optimal Δ, empty dots (dashed line) to $\Delta = 0$, for $N = 46$. The extrapolated value of the energy is also shown. In the inset: magnetic order parameter $m = \sqrt{S(\pi, \pi)/L}$ for the two wavefunctions.

can be used to estimate the condensation energy, i.e. the difference of energy between the superconductor and the metal. Indeed, the precursor signal, on finite systems, of a symmetry breaking (which occurs only in the thermodynamic limit) is the existence of two distinct minima in the energy landscape. By increasing the lattice size, the energy barrier between these two minima raises up and, with few Lanczos steps, it is more and more difficult to cross it. Therefore, on large enough sizes, by starting from a metallic wavefunction and by applying $p = 2$ Lanczos steps, we remain stuck in the local minimum and we do not obtain the energy of the superconducting state. In this sense, it appears plausible that we can estimate the condensation energy.

For the case of 8 holes, both the variational $p = 0, 1, 2$ and the variance extrapolated results for the optimal variational wavefunction (with $\Delta = 0.7$) lie below in energy than the corresponding results for the $\Delta = 0$ wavefunction, see the upper panel of Fig. 4.5. In this case the difference in energy between the two wavefunctions is rather sizeable, $\Delta E \sim 0.02$, for the $p = 0$ variational level and is only slightly reduced by applying a few Lanczos steps. It turns out that the difference between the two extrapolated values is $\Delta E \sim 0.015$, implying a small but finite condensation energy. Therefore, in the intermediate hole doping, the two wavefunctions have a completely different structure, and hence, by applying few Lanczos steps, it is not possible to reconstruct the superconducting order starting from a wavefunction which does not contain it. We obtain that the condensation energy has a maximum at finite hole density and decreases when the doping in reduced. It is remarkable that this is just what is found experimentally from specific heat measurements [104].

On the other hand, the value of the variational parameter Δ is found to increase by reducing the number of holes. Even though the value of P_d is certainly related to the superconducting order parameter, the meaning of the "bare" variational parameter Δ is not clear. Indeed, although in the wavefunction (4.7) there are "preformed" pairs of electrons, the Gutzwiller projector strongly affects the charge dynamics, which, at half-filling, is completely frozen. Therefore, due to the strong electron correlations, Δ does not have the meaning of the superconducting gap, as it happens in the standard BCS theory. At finite doping δ, the holes generate a non-trivial charge dynamics, making possible a finite superconducting order parameter of order δ. It is worth noting that, because of the local constraint, P_d is of the order of the number of holes and not of the number of the electrons, as expected in a weakly correlated system. By contrast, Δ should control the single-particle excitations and could be related to the value of the pseudogap. Experimentally, it is found that, in the underdoped region of cuprates, above the superconducting critical temperature, there is a large $d_{x^2-y^2}$ gap in the excitation

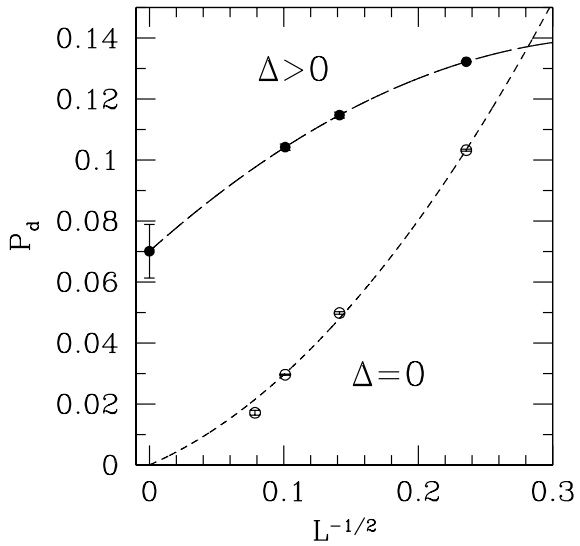

Figure 4.7: Size scaling of the variance extrapolated d-wave order parameter P_d for the d-wave wavefunction of Eq. (4.7) with $\Delta \neq 0$ (full circles and long-dashed line) and for the metallic wavefunction with $\Delta = 0$ (empty circles and short-dashed line). The extrapolated value of P_d for $\Delta \neq 0$ is also shown, and the lines are guide to the eye.

spectrum [6, 7], though there is not a true superconducting long-range order. The magnitude of the pseudogap decreases by increasing the hole doping, exactly as found for Δ. Moreover, in the slightly doped regime, the value of Δ is much higher than the one of the superconducting order parameter P_d, and therefore we might expect that at small but finite temperature the superconductivity is suppressed, while maintaining the "preformed" pairs.

In order to attempt a finite size scaling of the d-wave superconducting order parameter, we have considered a 98-site lattice and we have computed P_d for $N = 84$, corresponding to a hole doping of $\delta = 0.133$. In Fig. 4.7 the behavior of P_d as a function of the lattice size for this density is reported. In the 50 and 18-site lattice we have used a linear interpolation of the nearest densities available. Although by increasing the size from the small 18-site cluster to the 98-site one, the superconducting order parameter is decreased by a 20%, the finite size scaling is consistent with a finite value in the thermodynamic limit, implying a superconducting ground-state at this hole density for the $t-J$ model. On the other hand, the superconducting order parameter of the metallic wavefunction (with $\Delta = 0$) has a completely different behavior as a function of the system size, and it is consistent with a vanishing value in the thermodynamic limit. Indeed, although for the 18-site lattice the value of P_d of the metallic wavefunction is 20% smaller than the one of the superconducting wavefunction, by increasing the size of the cluster, the difference becomes more and more pronounced.

These results roughly confirm the ones of Ref.[72], though in that case a different strategy has been followed: the simulations were performed in the grand-canonical ensemble in the presence of a small external field which creates a d-wave Cooper pair. Then the calculation of the superconducting order parameter was performed by using the fixed-node and the stochastic reconfiguration approximations and the value of P_d was found by extrapolating to zero field. Although this kind of calculation has been demonstrated to be very accurate, at least on small sizes, it suffers from the fact that a difficult extrapolation to zero field is necessary. Indeed, although there is a qualitative agreement as far as the value of P_d is concerned, the method proposed in this thesis suggests that the value of P_d monotonically decreases by increasing the accuracy (e.g. by applying p Lanczos steps), on the contrary, in Ref. [72], it is found that P_d is enhanced, with respect to its variational value, both by fixed-node and stochastic reconfiguration. This may be a spurious effect which derives from the large value of the d-wave susceptibility at finite fields.

4.4 Charge and spin modulations

In this Section we study the dependence of the charge and spin distribution from the shape of the lattice. The motivation for this study is given by the fact that accurate density matrix renormalization group calculations applied to rectangular clusters with cylindrical boundary conditions find huge charge and spin modulations in the ground-state of the $t-J$ model for $J \sim 0.4t$ [73, 91]. The main limitation of this technique is that, up to very recently [105], it was not possible to consider a translationally invariant system, i.e. a lattice with periodic boundary conditions in both the directions, or sufficiently large clusters, such that the boundary effects are negligible. The breaking of the translational symmetry introduces huge spurious effects and may completely alter the nature of the ground-state. Indeed, as shown in the Chapter 3 by the analysis of the density-density structure factor, for $J \sim 0.4t$, there are incommensurate charge fluctuations, which can be easily enhanced by some external imposition. Within the density matrix renormalization group, stripes are found to be stable in a wide range of dopings and antiferromagnetic couplings [91], whereas the superconducting order parameter is found to be strongly suppressed [73].

By contrast, quantum Monte Carlo techniques, applied to square lattices with periodic boundary conditions, find that the finite-q charge fluctuations are strongly suppressed if compared to the ones found within the density matrix renormalization group. Moreover, the Monte Carlo method applied to clusters with cylindrical boundary condi-

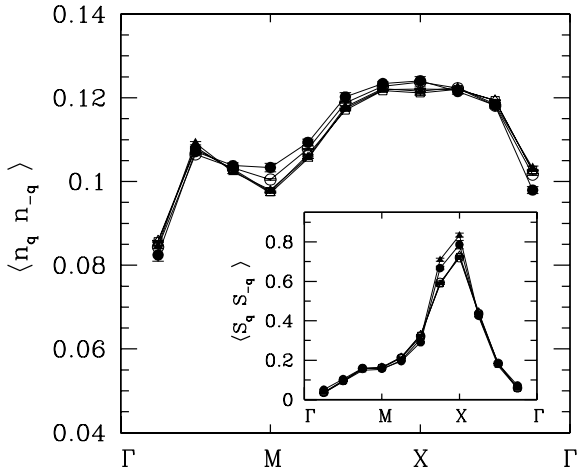

Figure 4.8: Density-density structure factor $N(q)$ for 8 holes on a 8×8 lattice and $J = 0.4t$. The variational with $p = 0$ (empty triangles), $p = 1$ (empty squares), $p = 2$ (empty circles), fixed-node (full triangles) and stochastic reconfiguration (full circles) results are reported. In the inset: the same for the spin-spin structure factor $S(q)$. $\Gamma = (0, 0)$, $X = (\pi, \pi)$, $M = (\pi, 0)$.

tions has shown a very weak charge modulation [106]. Nevertheless, though the density matrix renormalization group is $3 \div 4$ times more accurate in the variational energy than the quantum Monte Carlo, it is not clear whether the same is valid for the correlation functions. The discrepancy between these two numerical methods drives us to investigate, within the quantum Monte Carlo, the dependence of the charge distribution upon the anisotropies of the lattice. The simplest way to introduce the anisotropy, without breaking the translational symmetry, is to consider rectangular clusters with periodic boundary conditions in both directions. In this way, only the rotational symmetry is explicitly broken and a translational invariant wavefunction is expected to improve the accuracy of our quantum Monte Carlo calculation. The choice of rectangular lattices with periodic boundary conditions represents the mildest way to introduce an external perturbation to the square lattice without breaking the translational symmetry. For rectangular lattices, we consider the wavefunction of Eq. (4.7) with a different value for Δ in x and y directions.

We compute the density-density structure factor

$$N(q) = \langle n_q n_{-q} \rangle = \frac{1}{L} \sum_{i,j} e^{iq(R_i - R_j)} \langle n_i n_j \rangle, \tag{4.17}$$

and the spin-spin structure factor

$$S(q) = \langle S^z_q S^z_{-q} \rangle = \frac{1}{L} \sum_{i,j} e^{iq(R_i - R_j)} \langle S^z_i S^z_j \rangle, \tag{4.18}$$

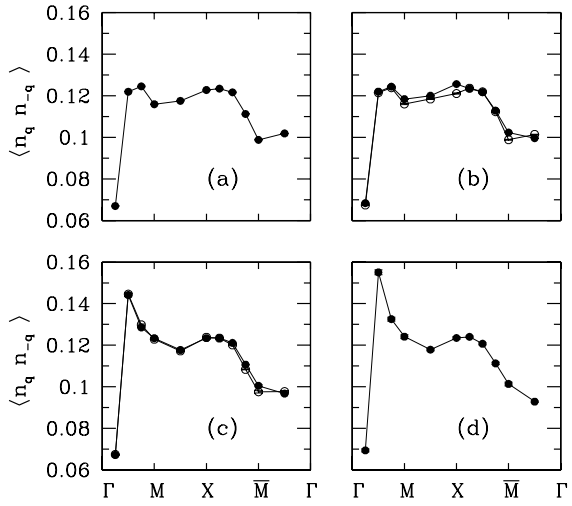

Figure 4.9: Density-density structure factor $N(q)$ for 4 holes on a 8×4 lattice and $J = 0.4t$. The variational with $p = 0$ (a), $p = 1$ and $p = 2$ (b), the fixed-node applied to the $p = 0$ (empty circles, c) and to the $p = 1$ (full circles, c) wavefunction, and the stochastic reconfiguration (d) results are reported. $\Gamma = (0, 0)$, $X = (\pi, \pi)$, $M = (\pi, 0)$, $\bar{M} = (0, \pi)$.

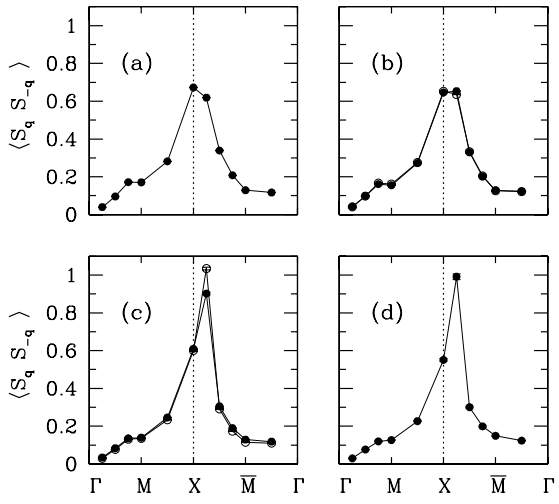

Figure 4.10: Spin-spin structure factor $S(q)$ for 4 holes on a 8×4 lattice and $J = 0.4t$. The variational with $p = 0$ (a), $p = 1$ and $p = 2$ (b), the fixed-node applied to the $p = 0$ (empty circles, c) and to the $p = 1$ (full circles, c) wavefunction, and the stochastic reconfiguration (d) results are reported. $\Gamma = (0, 0)$, $X = (\pi, \pi)$, $M = (\pi, 0)$, $\bar{M} = (0, \pi)$.

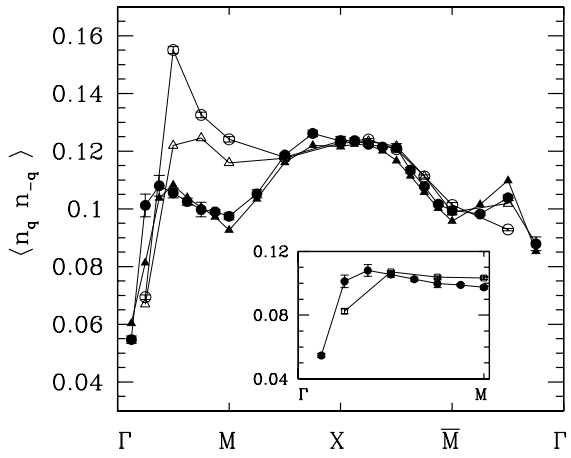

Figure 4.11: Density-density structure factor $N(q)$ for 4 holes on a 8×4 lattice and 16 holes on a 16×8 lattice and $J = 0.4t$. The empty symbols refer to the 8×4 cluster, the full ones to the 16×8 lattice. The variational with $p = 0$ (triangles) and the stochastic reconfiguration (circles) results are reported. In the inset it is shown the comparison between the 8×8 lattice (empty squares) and the 16×8 one (full circles), along the $\Gamma - M$ direction. $\Gamma = (0, 0)$, $X = (\pi, \pi)$, $M = (\pi, 0)$, $\bar{M} = (0, \pi)$.

for a rectangular 8×4 and a square 8×8 lattice with 4 and 8 holes respectively: in this way both the clusters have the same hole density, $\delta = \frac{1}{8}$. We find that, for the square lattice, the variational results for $N(q)$ and $S(q)$ are not modified by increasing the accuracy of the wavefunction: even within the most accurate approximation, the stochastic reconfiguration, the structure of both $N(q)$ and $S(q)$ is qualitatively, and also quantitatively, in agreement with the one of the $p = 0$ variational calculation. The direct inspection of the $N(q)$ does not reveal any trace of phase separation, and the only structure is a small peak in the $\Gamma - M$ direction for $q = (\pi/2, 0)$, see Fig. 4.8. Moreover, the spin-spin structure factor reveals a large peak for the commensurate wavevector $Q = (\pi, \pi)$, indicating that the ground-state has a strong short range antiferromagnetic order. Therefore, for this cluster, the d-wave wavefunction (4.7) represents a very good approximation of the ground-state and contains accurately the charge and spin correlations.

The situation is completely different for the rectangular cluster 4×8. In this case, although at the variational level the wavefunction does not show any kind of charge or spin order, a huge charge density wave is recovered within the stochastic reconfiguration and the fixed-node schemes. In Fig. 4.9, we report the calculation of $N(q)$ for various approximations. For this kind of cluster and the chosen hole density $\delta = \frac{1}{8}$, we find that the most accurate methods are able to produce a peak at $q_c = (\pi/2, 0)$, not present in the variational wavefunction, where the density-density correlations are almost structureless. In this case, the improvement given by the Lanczos steps is not sufficient to build

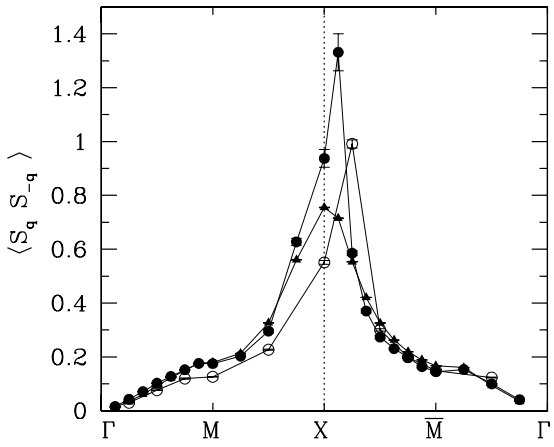

Figure 4.12: The stochastic reconfiguration results for the spin-spin structure factor $S(q)$ for 4 holes on a 8×4 lattice (empty circles) and 16 holes on a 16×8 lattice and $J = 0.4t$ (full circles). The $p = 0$ variational results for the 16×8 lattice (full triangles) are also reported. $\Gamma = (0, 0)$, $X = (\pi, \pi)$, $M = (\pi, 0)$, $\bar{M} = (0, \pi)$.

	$E_{p=0}/L$	$\Delta_{p=1}$	$\Delta_{p=2}$	Δ_{best}
8×4	-0.64144(5)	0.0306(1)	0.0400(1)	0.0437(4)
16×8	-0.64074(5)	0.0219(1)	0.0296(2)	0.0329(6)

Table 4.3: Variational energy per site with $p = 0$, $E_{p=0}/L$, and energy accuracy $\Delta_p = (E_p - E_{p=0})/E_{p=0}$, with $p = 1, 2$. $\Delta_{best} = (E_{SR} - E_{p=0})/E_{p=0}$ is related to the best variational energy obtained with the stochastic reconfiguration method.

up the incommensurate charge peak. Indeed, the application of few Lanczos iterations is not enough to completely change the structure of the starting wavefunction, and some more involved scheme, like the stochastic reconfiguration, is needed [87].

Furthermore, as shown in Fig. 4.10, a similar situation occurs also for the spin-spin structure factor $S(q)$: in this case the variational wavefunction has a broad maximum around $Q = (\pi, \pi)$, and the structure is only slightly changed by the application of one and two Lanczos steps. By contrast, within the fixed-node and the stochastic reconfiguration approximations, a sharp incommensurate peak rises at $q_s = (3\pi/4, \pi)$. It is remarkable that the wavevector q_c and q_s for which the $N(q)$ and the $S(q)$ have the peaks are exactly the ones that are found experimentally (see Section 4.1). These findings are in good qualitative agreement with the ones obtained with the density matrix renormalization approach [73, 91], where however cylindrical boundary conditions enhance even more the stripe features of the ground-state.

In order to clarify the relevance of the stripes in large size systems, we consider the

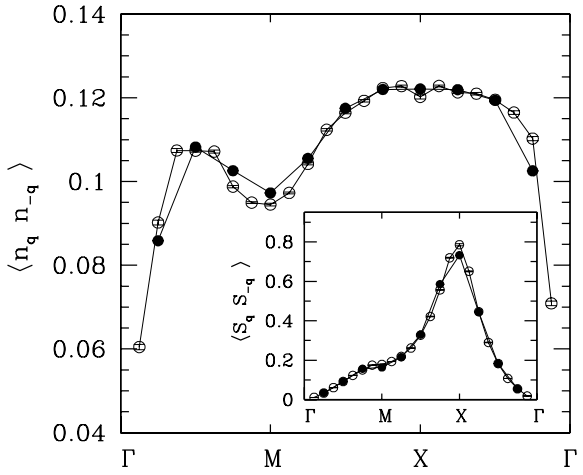

Figure 4.13: The $p = 0$ variational results for the density-density structure factor $N(q)$ for 8 holes on a 8×8 lattice (full circles) and 32 holes on a 16×16 lattice and $J = 0.4t$ (empty circles) are reported. In the inset: the same for the spin-spin structure factor $S(q)$. $\Gamma = (0,0)$, $X = (\pi,\pi)$, $M = (\pi,0)$.

16×8 lattice with the same hole density, $\delta = \frac{1}{8}$. By increasing the system size from the 8×4 lattice to the 16×8 one, we have only a slight loss in the accuracy. Indeed, as shown in Table 4.4, our best variational energy for the largest system is only 25% worse than the one for the smallest 8×4 cluster. Therefore, we expect that the accuracy on the density-density and spin-spin structure factor is sufficient to detect possible electronic fluctuations at incommensurate wavevectors. We find that, as shown in Fig. 4.11, the structure of $N(q)$ for this large rectangular lattice is completely different from the one of the small 8×4 cluster. In particular, in the $\Gamma - M$ direction, the results of the $p = 0$ variational wavefunction are much more similar to the ones of the 8×8 lattice. This feature is preserved also within the fixed-node and the stochastic reconfiguration techniques. Moreover, the incommensurate peak in the spin-spin structure factor shifts towards the commensurate wavevector $Q = (\pi,\pi)$ at $q_s = (7\pi/8, 0)$, see Fig. 4.12, suggesting that the particular stripe-like feature of the 8×4 lattice disappears by increasing the size of the cluster. It is noticeable that the incommensurate peak of the $S(q)$ at q_s is a genuine non-perturbative feature of the most accurate techniques (fixed-node and stochastic reconfiguration), and does not appear in a simple, i.e. $p = 0$, calculation (see Fig. 4.12). It is also remarkable that, within the forward walking technique of both the fixed-node and the stochastic reconfiguration, there is a considerable enhancement of the density-density structure factor $N(q)$ for $q_c = (\pi/4, 0)$, exactly the momentum q_c related to q_s. The fact that the structure of the $S(q)$, and partially of the $N(q)$, is substantially changed

by the stochastic reconfiguration (and by the fixed-node) strongly indicates that our most accurate methods are able to detect the tendency towards stripe-formation. Therefore, these results strongly indicate that, in the large size limit, whatever the shape of the lattice is, the projected d-wave wavefunction gives an exceptionally good approximation of the true ground-state, and that the stripe-like features found within the density matrix renormalization group are size effects due to the smallness of the cluster considered, further enhanced by the fact that in one direction there are open boundary conditions.

A particular important point is that there is a very singular convergence to the thermodynamic limit. Our results suggest that, as shown in Fig. 4.13, for square lattices the size scaling is smooth and, by increasing the lattice size up to the 16×16 cluster, there are no important modifications in the structure of the charge and spin correlations. By contrast, for rectangular lattices, the size scaling is much more subtle a tricky, for example the $N(q)$ along the $\Gamma - M$ direction changes dramatically by increasing the size, even at the $p = 0$ variational level (see Fig. 4.11), indicating that for rectangular clusters there are huge size effects.

4.5 Conclusions

In this Chapter we have performed a study of the superconducting order in the $t - J$ model at $J = 0.4t$ and low hole densities. Moreover, in the last Section, we have addressed the question of charge and spin ordering, recently raised by density matrix renormalization group calculations [73, 91].

The projected d-wave wavefunction is found to be an excellent approximation of the ground-state of the $t - J$ model. Furthermore, the accuracy of the variational ansatz can be further improved by the exact application of p Lanczos steps. In this way, as demonstrated in Section 2.4.1, it is possible to extract information about the energy and the correlation functions of the exact ground-state. This method turns out to be exceptionally reliable and unbiased whenever it is possible to have an exact reference to compare with. It is noticeable that the variance extrapolation gives very accurate results even on rather large size systems and, up to $L \sim 100$ sites, it is safely possible to estimate the exact ground-state energy. Indeed, for the projected d-wave wavefunction on square lattices with $L \lesssim 100$, each Lanczos step reduces both the energy and the variance by about a factor of two, making possible a very stable linear extrapolation.

The estimate of the condensation energy, i.e. the difference in energy between the superconductor and the metal is also possible by the same method. Motivated by a finite condensation energy at doping $\delta \sim 0.15$ we calculated the superconducting order

parameter P_d for this hole density. A finite size scaling of this quantity shows that P_d is finite in the thermodynamic limit, indicating the superconducting nature of the ground-state of the $t-J$ model. For this value of the doping and on square lattices, the charge and spin structures of the variational wavefunction is found to describe very well the ones of the ground-state, and they do not qualitatively change by increasing the degree of accuracy. By contrast, on a small 8×4 rectangular cluster with periodic boundary conditions, the projected d-wave wavefunction does not contain the stripe-like ordering characteristic of the ground-state. These charge and spin correlations can be easily detected by the fixed-node and the stochastic reconfiguration approaches. However, these effects are restricted to small sizes: indeed, by considering a larger 16×8 lattice, the stripe order vanishes and the density-density structure factor becomes similar to the one of square clusters. These results suggest that the d-wave superconducting wavefunction is a very stable state for the $t-J$ model even at moderately small couplings J. However, it is possible that small anisotropies in the Hamiltonian, like different hoppings and antiferromagnetic couplings in the two directions ($t_x \neq t_y$, $J_x \neq J_y$) can drive the system towards a stripe-like instability.

Chapter 5

Ferromagnetism from strong local repulsion

5.1 Introduction

The theory of magnetic ordering in crystals is one of the oldest problems in solid state physics. A theory of magnetism based on a free electron gas is hopelessly inadequate as an approach to real metals: to explain the magnetic ordering, in the great majority of cases, it is necessary to go beyond the independent electron approximation. The development of a tractable model of magnetic metal, capable of describing both the spin correlations and the electronic transport properties, remains one of the major unsolved problem in solid state theory.

Although a theory of magnetism based on a free electron approximation does not give a satisfactory interpretation of the phenomenon, it provides a very simple model in which the magnetic structure is implied in the absence of an explicit spin-dependent interaction. Bloch [107] first pointed out that the Hartree-Fock approximation can predict ferromagnetism in a gas of electrons interacting only through the Coulomb potential. Within this approximation, if every one-electron level with a given wave vector less than k_F is occupied by two electrons of opposite spin, then the ground-state energy of N free electrons is

$$E = N\left[\frac{3}{5}(k_F a_0)^2 - \frac{3}{2\pi}(k_F a_0)\right]\frac{e^2}{2a_0}, \tag{5.1}$$

where a_0 is the Bohr radius and e is the electron charge. The first term in Eq. (5.1) is the total kinetic energy, and the second is the Hartree-Fock approximation of the electron-electron Coulomb interaction (the exchange part only). Instead of assuming that every one-electron energy level is occupied by two particles of opposite spin, a more general

possibility is to fill each one-electron level with $k < k_\uparrow$ with spin-up electrons and each level with $k < k_\downarrow$ with spin-down electrons, leading to a net spin imbalance. Since in the Hartree-Fock approximation the exchange interaction is only between particles with opposite spin, we have an equation of the form (5.1) for each spin population

$$E_\uparrow = N_\uparrow \left[\frac{3}{5}(k_\uparrow a_0)^2 - \frac{3}{2\pi}(k_\uparrow a_0)\right] \frac{e^2}{2a_0} \tag{5.2}$$

$$E_\downarrow = N_\downarrow \left[\frac{3}{5}(k_\downarrow a_0)^2 - \frac{3}{2\pi}(k_\downarrow a_0)\right] \frac{e^2}{2a_0}, \tag{5.3}$$

where the total energy and number of particles are given by

$$E = E_\uparrow + E_\downarrow \tag{5.4}$$

$$\frac{N}{V} = \frac{N_\uparrow}{V} + \frac{N_\downarrow}{V} = \frac{k_\uparrow^3}{6\pi^2} + \frac{k_\downarrow^3}{6\pi^2} \equiv \frac{k_F^3}{6\pi^2}. \tag{5.5}$$

If we take $N_\uparrow \neq N_\downarrow$ and we find an energy lower than the one of Eq. (5.1), the ground-state has a non-vanishing magnetization and the electron gas will be partially (or fully) polarized.

For simplicity, if we consider the limiting case of $N_\uparrow = N$ and $N_\downarrow = 0$, then we have that $k_\uparrow = 2^{1/3} k_F$, and the total energy is

$$E = N \left[\frac{3}{5} 2^{2/3} (k_F a_0)^2 - \frac{3}{2\pi} 2^{1/3} (k_F a_0)\right] \frac{e^2}{2a_0}. \tag{5.6}$$

If we compare the energy of the non-magnetic case, Eq. (5.1), with the one of the fully polarized case, Eq. (5.6), we have that in the former case the kinetic energy is larger by a factor $2^{2/3}$, whereas the exchange energy is smaller by a factor $2^{1/3}$. Therefore the ground-state will be fully polarized if the exchange energy dominates the kinetic energy. This situation happens for small k_F, i.e. at low densities. Therefore, as the density decreases, a transition from a non-magnetic to a fully polarized ground-state occurs within this approximation.

Unfortunately, these simple arguments for the magnetic instability are invalidated by different considerations. First, even within the Hartree-Fock approximation there are other more complicated solutions for the one-electron levels that lead to lower energies than the one of the fully polarized state [108]. Moreover if the Hartree-Fock approximation is improved by introducing a screening in the electron interaction, the scenario changes drastically. For example, in the extreme limit of a delta-function potential, ferromagnetism in the high density limit is found, whereas at low densities the non-magnetic phase is stable. Indeed, at very low electron densities, the ground-state of the electron

gas can be shown to crystallize into a *Wigner crystal*, whose description is outside the reach of the independent electron approximation.

Furthermore, although the best Hartree-Fock ground-state is by no means obvious, the correlations between electrons can drastically alter its predictions. Ferromagnetism has been observed experimentally in metals whose free ions contain partially filled d of f shells, which are well beyond a free electron description. Indeed, a simple approach to explain ferromagnetism in these compounds is obtained by combining the free electron picture of itinerant ferromagnetism with the band theory, i.e. by calculating a different self-consistent field for electrons of opposite spins. However this approach is not satisfactory at all, and a more complete theory, which takes into account correlations between itinerant electrons is needed.

In 1963 Hubbard [12] proposed a highly oversimplified model to describe the interplay between the band-like and localized behavior of these materials. In this model the vast set of bound and continuum electron levels of each ion is reduced to a single localized orbital level. The non trivial ingredient is that pairs of electrons with opposite spins that occupy the same ion pay an on-site energy U. For a large Coulomb interaction U, electrons can prefer to occupy only a single spin sector, up or down, minimizing therefore the strong Coulomb repulsion, leading to a magnetic ground-state. Indeed, as Nagaoka showed in a milestone paper [80], a single hole in the infinite-U Hubbard model on any finite bipartite cluster with periodic boundary conditions, for any dimension $d \geq 2$ has a fully polarized ferromagnetic ground-state, i.e the ground-state has a maximum spin S. Unfortunately the Nagaoka theorem refers to a single point in the phase diagram, which is not thermodynamically significant. A central point in the theory of strongly correlated electronic systems is to understand if a ferromagnetic Nagaoka ground-state can survive at finite hole densities or finite Coulomb repulsions. In the Hartree-Fock approximation of the Hubbard model [46], a large part of the phase diagram shows a ferromagnetic ground-state (see Fig. 1.3). However, in the real phase diagram, the ferromagnetic region is expected to be strongly reduced, or even completely absent.

Driven by the Nagaoka result on the infinite-U Hubbard model (or equivalently the $t - J$ model at $J = 0$), many authors have recently tried to answer the old question of the ferromagnetic stability of the two-dimensional infinite-U Hubbard model [20, 21, 22, 81, 82, 83], but the situation is still rather controversial. In particular Putikka and co-workers [20], using the high-temperature expansion, found that the ground-state has not a saturated magnetization for all hole densities, ruling out the possibility of a stable ferromagnetism at any finite hole concentration. However, because of the uncer-

tainties of their extrapolation to zero temperature, their calculation cannot be considered as a definite proof of the complete absence of a Nagaoka state at finite hole densities. By contrast, variational calculations based on a single spin flip on the saturated ferromagnetic state [21, 22] give a doping concentration $\delta_c \sim 0.25$ as the upper bound for the stability of the Nagaoka state.

Another way of tackling this problem is to evaluate the spin of the ground-state on finite small clusters, where exact diagonalizations are possible. However, on small lattices, the total spin of the ground-state is strongly dependent upon the number of holes and the chosen boundary conditions. For instance, for two holes on any finite cluster with periodic boundary conditions it is possible to show [82] that the ground-state spin is not maximum whereas for certain finite number of holes such that the ferromagnetic ground-state is non degenerate with periodic boundary conditions, the ground-state has maximum spin [109]. In general, for small clusters, there is a strong dependence of the ground-state spin on the number of holes and on boundary conditions, indicating large shell effects [84]. Definitely, these effects become less and less important by increasing the size of the system, and the hope is that they are negligible for systems that can be studied by numerical methods.

In this Chapter we study the stability of the ferromagnetism in the two-dimensional $t-J$ model at $J=0$, namely

$$H = -t \sum_{\langle i,j\rangle,\sigma} \tilde{c}^{\dagger}_{i,\sigma}\tilde{c}_{j,\sigma} \tag{5.7}$$

where the constraint of no doubly occupied sites is enforced by the fact that $\tilde{c}^{\dagger}_{i,\sigma} = c^{\dagger}_{i,\sigma},(1-n_{i,\bar{\sigma}})$, being $n_i = \sum_\sigma n_{i,\sigma}$ the electron density on site i. The method we use are quantum Monte Carlo techniques, i.e. variational with $p = 0, 1, 2$ Lanczos steps and fixed-node approximation.

5.2 Results

The wavefunction used in the variational Monte Carlo and in the Green function Monte Carlo as a guiding wavefunction is the one described in Section 3.3.1:

$$|\Psi\rangle = \mathcal{P}_N \mathcal{P} \mathcal{J} \prod_k \left(1 + f_k c^{\dagger}_{k,\uparrow} c^{\dagger}_{-k,\downarrow}\right)|0\rangle, \tag{5.8}$$

where $\mathcal{P}_N$ is the projector onto the subspace of N particles, $\mathcal{P}$ is the Gutzwiller projector, which forbids doubly occupied sites, $\mathcal{J}$ is a density-density Jastrow factor (3.33), and f_k is defined by Eq. (3.22). The variational parameters f_k of the pairing wavefunction may

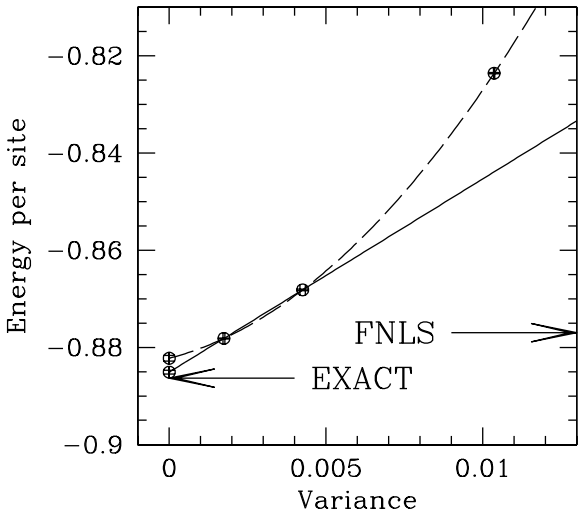

Figure 5.1: Variational energies for $p = 0, 1, 2$ Lanczos steps in the singlet subspace for 10 electrons on 18 sites. The continuous line is the linear fit of $p = 1, 2$, the dashed line is the quadratic fit of $p = 0, 1, 2$. The extrapolated points with zero-variance and the FNLS result are also shown.

also represent the Gutzwiller wavefunction in the particular case of $f_k = \Theta(\epsilon_F - \epsilon_k)$, where ϵ_F is the free Fermi energy, ϵ_k is the corresponding dispersion $\epsilon_k = -2t(\cos k_x + \cos k_y)$ and Θ is the step function. For closed shell fillings, this wavefunction is a singlet. For open shell, we take f_k with a small d-wave or s-wave symmetry in order to split the bare degeneracy, the resulting wavefunction being a singlet. Analogously, by using the particle-hole transformation on down spins, we are able to consider a number of up electrons which is different from the number of down electrons, corresponding to a finite total spin $S > 0$.

We use the 45° tilted squares with $L = l\sqrt{2} \times l\sqrt{2}$ sites with periodic boundary conditions, which possess the full spatial symmetries of the infinite lattice. We indicate with VMC the variational Monte Carlo results obtained with the wavefunction (5.8), with 1LS and 2LS the results obtained with $p = 1, 2$ Lanczos steps applied to (5.8), respectively. Moreover, the results obtained by fixed-node using (5.8) with one Lanczos step as a guiding wavefunction are indicated with FNLS.

For large doping the ground-state is believed to be a paramagnetic liquid, and in this region the Gutzwiller wavefunction, with the density-density Jastrow factor, gives a very good approximation. We report in Fig. 5.1 variational and FNLS results for 10 electrons on 18 sites in the subspace of $N_\uparrow = N_\downarrow$. Although the FNLS is rather accurate, on this small cluster the 2LS has a better energy. Moreover, using the variational results with different number of Lanczos steps, it is possible to extrapolate to the zero-variance limit,

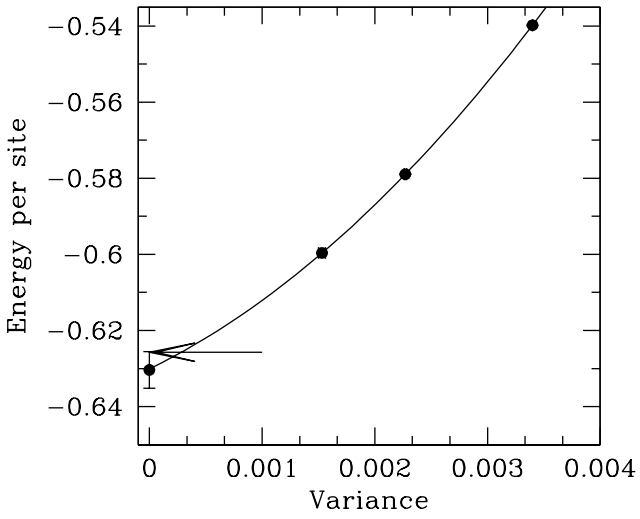

Figure 5.2: Variational energies for $p = 0, 1, 2$ Lanczos steps for 28 electrons on a one-dimensional lattice of 50 sites. The continuous line is the quadratic fit of $p = 0, 1, 2$. The extrapolated point with zero-variance is also shown.

and estimate the exact ground-state energy. For $J = 0$ the variational wavefunction (5.8) is not as accurate as in the case of finite J's, and using the $p = 0, 1, 2$ Lanczos steps, the energy as a function of the variance σ has a finite curvature and the extrapolated value slightly overestimates the exact ground-state energy. Because the linear behavior of the energy as a function of the variance is expected for $\sigma^2 \to 0$, we can use the $p = 1, 2$ points to linearly extrapolate the value of the exact energy, which actually gives a very accurate estimate. The 2LS represents our best variational result and the extrapolation our best, non-variational, estimation of the exact value. In the 18-site lattice with periodic boundary conditions, the fully polarized ferromagnet is stable only for one hole, while even for two holes the spin is not maximum. As noted by Riera and Young [84] in the 4×4 lattice, the total spin of the ground-state is strongly dependent upon the number of holes, at least in the low-doping region. This is due to the fact that, for small sizes and periodic boundary conditions, the ferromagnetic state is frustrated for a number of holes which is not a closed shell. Therefore it is crucial to consider larger systems, where shell effects, induced by boundary conditions, are weaker than for 18 sites. Indeed the difference in energy using different boundary conditions goes to zero by increasing the number of lattice sites.

The method of the variance extrapolation gives exceptionally good results also for large size systems. For example in one dimension and $J = 0$, where the exact solution is known by the Bhete ansatz [110], it is possible to obtain the exact result within

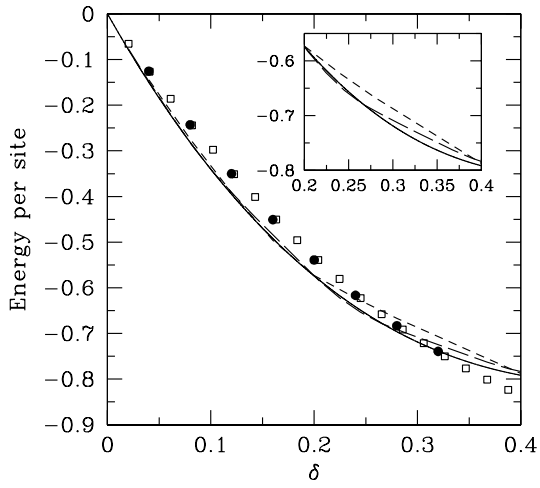

Figure 5.3: FNLS results for the 50-site(full circles) and the 98-site (empty squares) cluster in the singlet subspace. The ferromagnetic energy for 50 sites (short dashed line), 98 sites (long dashed line) and the 100×100 lattice (continuous line) are also reported.

the statistical errors, even starting from a very poor variational wavefunction, i.e. the Gutzwiller one (see Fig. 5.2). In this case the $p = 0$ variational energy is rather poor, $E/L = -0.5398(1)$, with respect to the exact one, $E_{ex}/L = -0.62575$, and it is largely improved by one and two Lanczos steps. Moreover it is worth noting that, although the energy difference between the best variational result and the exact one is still rather sizeable, the extrapolated value gives the exact value of the energy. Since the convergence of the Lanczos technique is not particularly dependent upon dimensionality and type of interaction, it is safely assumed that similar performances can be obtained even for the much more interesting and complicated problem of the two-dimensional lattice.

In order to perform a systematic study of the spin instability, we consider the 50-site and the 98-site lattices. The results in the singlet subspace for these two systems are almost in quantitative agreement, suggesting that, for $L \sim 100$, the finite size corrections are small compared to the energy difference between the singlet and the saturated ferromagnet. In Fig. 5.3 we show the energies for the fully polarized and the singlet state, by using FNLS results, for these two lattices. Contrary to the very weakly size dependent singlet energies, the ferromagnetic energies for 50 and 98 sites are sizeable different in the delicate region $0.2 < \delta < 0.3$, where there is the level crossing at the variational level between the singlet state and the fully polarized state. However the value of the ferromagnetic energy for the 98-site lattice almost coincides with the one of a 100×100 lattice, which is expected to represent the thermodynamic limit.

In Fig. 5.4 we report the difference in energy between the singlet and the fully po-

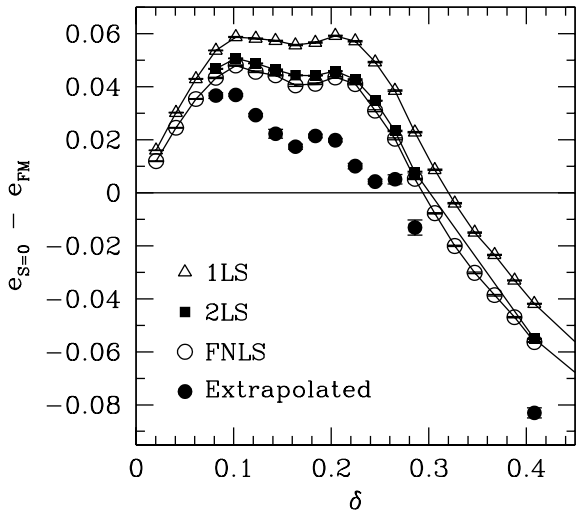

Figure 5.4: Differences between the singlet energy per site $e_{S=0}$ and the fully polarized one e_{FM} for the 98-site lattice as a function of the hole concentration for different approximations: 1LS (open triangles), 2LS (full squares), and FNLS (open circles), the extrapolated value (full circles) is also reported.

larized state for different hole densities and Monte Carlo techniques for the 98 sites. For large doping the homogeneous singlet state is well below in energy than the ferromagnet but by decreasing the number of holes there is a sharp evidence for a fully polarized ground-state in the low-doping region. All the Monte Carlo methods give a very large critical doping $\delta_c \sim 0.28 \div 0.30$ for the transition between the two states. Of course this is a variational estimate and gives an upper bound for the transition. By contrast, if we consider the extrapolated value of the energy, δ_c is strongly pushed at much lower doping. Although, in this case, the large statistical errors prevent us to extract the transition point, it is clear that at low doping the homogeneous singlet state is higher in energy than the fully polarized state. This feature is also clear in the 50-site lattice.

In Fig. 5.5 we show the variational energies for 42 electrons on 50 sites, which corresponds to $\delta = 0.16$. For this number of electrons the singlet is a closed shell. Here we consider all the possible values of the spin leading to a closed shell, i.e. $\Delta N = N_\uparrow - N_\downarrow = 0, 16, 32$. As found for the 98-site lattice, for this doping the singlet is well above in energy than the fully polarized ferromagnet, although in this case the number of holes is such that the singlet is a closed shell, and therefore the configuration is not frustrated. Instead, for this number of holes the ferromagnetic state is not a closed shell and hence its configuration is unfavorable. Moreover, from Fig. 5.5, the energy is found to be monotonically decreasing by increasing the total spin.

In the low-doping region the fully polarized state is found to be stable, implying

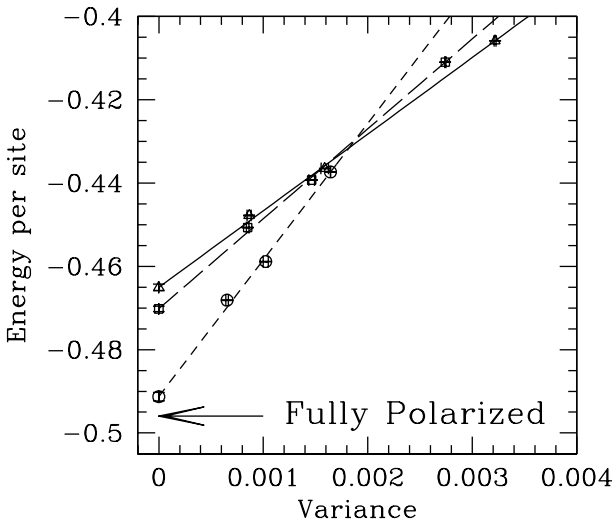

Figure 5.5: Variational energies with $p = 0, 1, 2$ Lanczos steps in different total spin sectors for 42 electrons on 50 sites: $S = 0$ (triangles, continuous line), $S = 8$ (squares, long-dashed line), and $S = 16$ (circles, short-dashed line). The fully polarized energy for the same lattice is also reported.

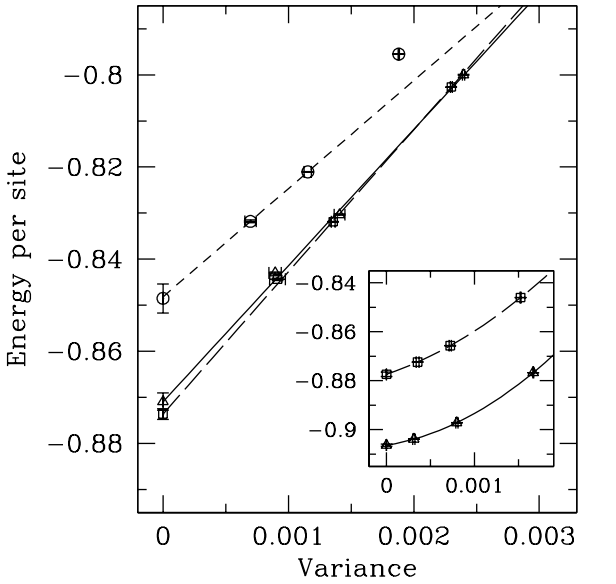

Figure 5.6: Variational energies with $p = 0, 1, 2$ Lanczos steps in different total spin sectors for 58 electrons on 98 sites: $S = 0$ (triangles, continuous line), $S = 8$ (squares, long-dashed line), and $S = 16$ (circles, short-dashed line). In the inset: the same for $S = 0$ (triangles, continuous line) and $S = 8$ (squares, long-dashed line) for 42 electrons on 98 sites.

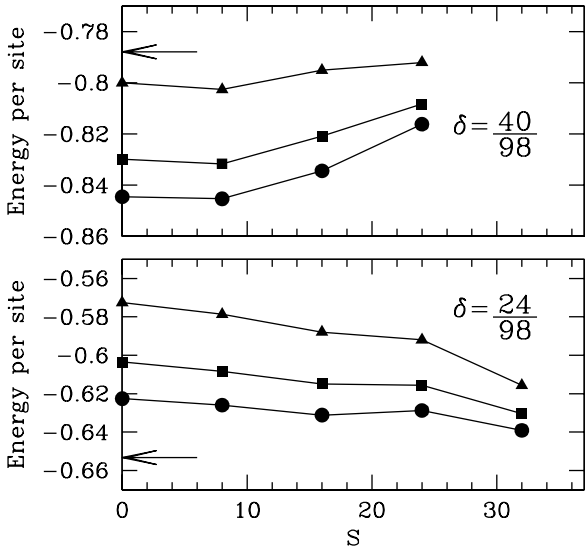

Figure 5.7: Upper panel: variational with $p = 0$ (full triangles), $p = 1$ Lanczos steps (full squares) and FNLS (full circles) results for the ground-state energy as a function of the total spin S for 58 electrons on 98 sites. The ferromagnetic energy is marked by the arrow. Lower panel: the same for 74 electrons on 98 sites.

that a partially polarized ground-state for intermediate doping can exist. For very large doping, $\delta \gtrsim 0.5$, the ground-state is found to be paramagnetic and the energy is an increasing function of the total spin, with a finite spin susceptibility. In the inset of Fig. 5.6 it is shown the case of 42 electrons on 98 sites for $S = 0$ and $S = 8$, which are both closed-shell configurations. For every variational calculation, the results are consistent with a singlet ground-state and a finite gap between these two spins. By decreasing the hole concentration, the lowest spin states collapse to the singlet and eventually becomes degenerate with it, implying a divergent spin susceptibility. For 58 electrons on 98 sites, we found that, for all the Monte Carlo techniques used, the singlet is almost degenerate with the $S = 8$ state (see Fig. 5.6). Indeed, although in the VMC calculation there is a small difference between the energy of the $S = 0$ and the $S = 8$ state, by increasing the accuracy with $p = 1, 2$ Lanczos steps, the two energies tend to become closer and closer and even the extrapolated values give a degeneracy of these two spins. By contrast the $S = 16$ state remains always well above in energy.

This scenario is consistent with a second order transition between a paramagnetic liquid and a polarized state. The spin susceptibility, related to the curvature of the energy as a function of the spin, is finite in the stable paramagnetic region and diverges at the transition, reflecting the collapse of the low-lying states with finite total spin.

Although within the fixed-node scheme the total spin is not defined, if the guiding wavefunction is a good approximation of a state with total spin S, then the ground-state

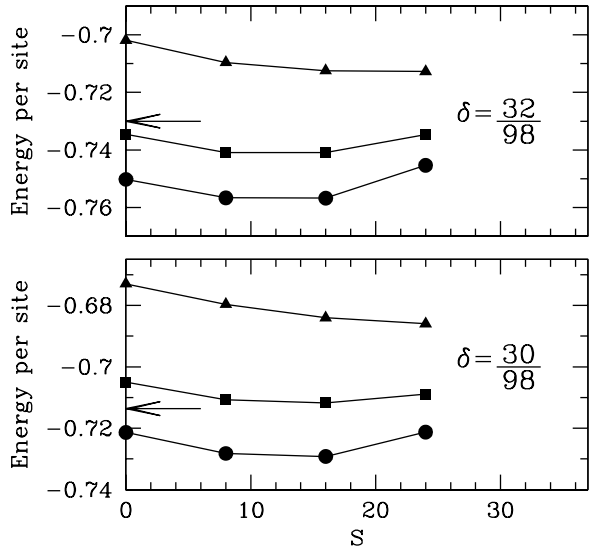

Figure 5.8: Upper panel: variational with $p = 0$ (full triangles), $p = 1$ Lanczos steps (full squares) and FNLS (full circles) results for the ground-state energy as a function of the total spin S for 66 electrons on 98 sites. The ferromagnetic energy is marked by the arrow. Lower panel: the same for 68 electrons on 98 sites.

of the effective fixed-node Hamiltonian will have a large overlap with the state of spin S. In this sense we can specify, also within the FNLS approximation, the total spin of the wavefunction. The degeneracy of the $S = 0$ and $S = 8$ states persists also within the FNLS approximation. In the upper panel of Fig. 5.7 we report the variational energies with $p = 0, 1$ and the FNLS results as a function of the spin S. For this lattice the FNLS represents the best variational result, giving an energy lower than the best $p = 2$ variational result. It is worth noting that, even within the FNLS scheme, we found that the singlet and the $S = 8$ state are almost degenerate, whereas the $S = 16$ state is well above in energy. The situation is completely different in comparison to the case of 74 electrons. Here all the variational and FNLS results are consistent with a decreasing behavior of the energy with increasing the spin S, being the minimum found for the fully polarized case.

In the region of intermediate doping, all the variational and FNLS approaches give a minimum in the energy at finite spin, in Fig. 5.8 we report the case of 66 and 68 electrons. This suggests that the total magnetization increases, varying the hole density, until saturation is reached for $\delta_c \sim 0.2 \div 0.25$.

5.3 Conclusions

In this Chapter we have addressed the problem of the ferromagnetic ordering in the $t-J$ model at $J = 0$. In this particular limit, the Hamiltonian contains only the kinetic term, and the strong correlation is given by the fact that doubly occupied sites are not allowed. Although there are no explicit magnetic interaction between the spins, Nagaoka [80] has shown that the ground-state of one hole on every lattice size is fully polarized. This astonishing result has lead to the natural question of the ferromagnetic stability at finite hole densities. This kind of problem requires large enough systems. Indeed, on small lattice, the choice of the boundary conditions plays a fundamental role in stabilizing a particular value of the ground-state spin.

We have performed Monte Carlo calculations with different approximations, i.e. variational with $p = 0, 1, 2$ Lanczos steps and fixed-node, for fairly large clusters, where the size effects are smaller than the energy scales we are interested in. At high hole doping, $\delta \gtrsim 0.5$, the ground-state is found to be a paramagnetic liquid with a finite spin susceptibility. Indeed for 42 electrons on 98 sites, all the approximations used give that the singlet has the lowest energy and states with finite total spin are well above in energy, separated by a finite spin gap. By decreasing the hole doping, the low-lying excited states with $S > 0$ collapse onto the singlet. For 58 electrons on the same cluster, we found that, for all the approximations considered, the state with $S = 8$ is almost degenerate with the singlet, and the two states become more and more degenerate by increasing the accuracy of the approximation. By contrast the state with $S = 16$ is separated by a finite energy gap. By decreasing further the doping the singlet eventually becomes higher in energy than the fully polarized state, and a clear evidence of saturated ferromagnetism at small hole doping, $\delta \lesssim 0.2$ is found. For example, in the 50-site lattice for 42 electrons, the ground-state is found to have its maximum spin value, and the energy is monotonically increasing with decreasing the total spin.

Conclusions

Motivated by the recent discovery of high-temperature superconductors, in this thesis we have investigated the ground-state properties of two-dimensional systems with strong electron-electron correlations, by using quantum Monte Carlo techniques on the lattice. The main outcome of this work is that, in the range of physically relevant antiferromagnetic couplings, $J = 0.2 \div 0.6t$, the ground-state of the $t - J$ model can be described by the d-wave superconducting state, projected in the subspace without doubly occupied sites, with a long-range density-density Jastrow factor. For small size systems, where exact results are available by Lanczos diagonalization, the energy and the correlation functions are qualitatively reproduced, the relative error being of the order of a few percent. The accuracy of the variational wavefunction can be further improved by the application of a few Lanczos steps. This can be easily done, without too much computational effort, by using the recently developed technique of the Green function Monte Carlo with stochastic reconfiguration [18, 19]. Moreover, since in a pure variational calculation it is possible to compute both the energy and the variance of a given wavefunction, and because the ground-state has the minimum energy and zero variance, an estimate of the ground-state energy can be extracted from the zero-variance extrapolation. Within the variance extrapolation method and by starting from the projected d-wave wavefunction, we obtain exact results, within the statistical errors, whenever exact diagonalization is possible, i.e. for $L \lesssim 26$, and it is plausible that the same holds up to $L \sim 100$.

This method also gives reliable results on energies down to the difficult limit of $J = 0$. Therefore, it is possible to gain insight into the possible ferromagnetic instability. The paramagnetic phase, stable at high hole doping, becomes unstable towards a partially polarized ferromagnetic metal at a relative high doping, $\delta \sim 0.4$. The results are consistent with a second-order transition, with a divergent spin susceptibility. In the low-doping region, the ground-state is found to be fully polarized, as suggested in Refs. [21, 22].

Furthermore, the variance extrapolation also allows us to estimate the condensation

energy, i.e. the difference of energy between the superconducting and the metallic phase. At finite antiferromagnetic couplings, the condensation energy is maximum for moderate hole dopings, whereas the ground-state shows a finite superconducting order parameter P_d in the thermodynamic limit, in agreement with what is found in Refs. [72, 58]. It is worth noting that, due to the local constraint, at small doping P_d is proportional to the number of holes and not to the number of electrons. On the other hand, the "bare" variational gap Δ, related to the single-particle excitations, is found to decrease by increasing the number of holes. Although it is found that the variational gap has a sizeable value $\Delta \sim J$, the local constraint strongly renormalizes the value of the true superconducting order parameter, and we obtain $P_d \sim 0.07$. These facts suggest that, while P_d could be related to the superconducting order parameter, and hence to the true superconducting gap, Δ might refer to the pseudogap observed in the underdoped metallic region of the cuprates. An interesting perspective is to find out the behavior of the charge gap as a function of the hole doping, and make a comparison with the experimental results.

The variance extrapolation scheme fails to correctly reproduce the charge and spin correlation functions when the antiferromagnetic coupling and the hole doping are such that strong electronic fluctuations are present, e.g. phase separation or stripes, and the ground-state is not uniform. In these cases more sophisticated methods, which rely on self-consistent approximations, like fixed-node or stochastic reconfiguration techniques, are needed to detect the spatial charge and spin distribution. By direct inspection of the energy per hole and the density-density structure factor, it is found that the onset for phase separation is $J \sim 0.5 \div 0.6t$, in agreement to what is found by other authors [57, 58, 59], and that for $J \sim 0.4t$ there are large charge fluctuations at small but finite wavevectors, indicating that the system is near to a charge density wave instability. The scenario is similar to what happens in the one dimensional $t - J$ model, where, near to the phase separation boundary, there is a liquid of bound pairs [111]. It is remarkable that this effect is characteristic of the $t - J$ model and it is not present in the Hubbard model, even for $U = 10t$, where the ground-state is found to be homogeneous. In this case, it turns out that the gain in energy by using the d-wave superconducting state with a Gutzwiller projector is negligible, suggesting that in the Hubbard model the condensation energy is vanishingly small. A possible way to significantly enhance the pairing correlations in the Hubbard model is by adding an effective exchange term J in addition to the Coulomb interaction U, as found in ladder systems [112]

The charge fluctuations are further enhanced if the underlying lattice breaks the rotational symmetry: we showed that for a small rectangular lattice the density-density and spin-spin structure factors have huge peaks for incommensurate wavevectors, similarly

to what is found within the density matrix renormalization group technique [73, 91], where the rotational symmetry is broken also by considering cylindrical boundary conditions. However, it turns out that the stripe-like features are an artifact of the boundary conditions, i.e. they are finite size effects due to the smallness of the cluster. Nevertheless, we expect that the $t - J$ is near to a charge density wave instability, and that small distortions of the underlying lattice or perturbations in the Hamiltonian could drive towards the same charge and spin modulations experimentally observed in $\mathrm{La_{2-x}Sr_xCuO_4}$ and $\mathrm{La_{1.6-x}Nd_{0.4}Sr_xCuO_4}$. It is likely that slight perturbations of the hopping amplitudes and of the antiferromagnetic couplings ($t_x \neq t_y$ and $J_x \neq J_y$), which introduce small anisotropies into the original model, can lead to stripe-like correlations in the ground-state. This possibility will be carefully considered in a forthcoming study.

Acknowledgments

First of all, it is a pleasure to acknowledge the stimulating collaboration with Sandro Sorella and Alberto Parola. Special thanks are due to Matteo Calandra, Massimo Capone, Luca Capriotti, with whom part of this work has been done. I am grateful to Michele Fabrizio and Giuseppe Santoro for useful suggestions and discussions (and to Giuseppe also for a careful reading of this work). I also thank Stefania de Palo, Erik Koch and Claudia Filippi for discussion on the fixed-node approximation and other numerical methods, and to Matthias Troyer on density matrix renormalization group. It is also a pleasure to gratefully acknowledge Giovanni Bachelet, for his suggestions and for his interest in this work. I would like to acknowledge the "Rome group" for enlightening insight into the physics of high-temperature superconductors: Carlo Di Castro, Claudio Castellani, Sergio Caprara, Marco Grilli and Andrea Perali. Finally, I would like to acknowledge Steve White, Elbio Dagotto and George Martins for sending me unpublished data on the $t - J$ model.

Appendix A

Implementation of symmetries in the Lanczos algorithm

In this Appendix we describe how to implement the symmetries in the Lanczos algorithm. Let $|c_m\rangle$ be the representative element of a given equivalence class labeled by m [113]. $|c_m\rangle$ represents a fixed electron configuration on the lattice. We denote by g a generic element of the symmetry group. An orthonormal basis in the symmetrized Hilbert space is

$$|m\rangle = \frac{1}{\sqrt{A_m}} \sum_g{}' e^{i\phi_g} g|c_m\rangle, \tag{A.1}$$

where the sum is over the symmetries which generate distinct states, and $A_m = N_s/\mu_m$ is the number of these states, N_s being the number of the elements of the group and μ_m the multiplicity of the state, ϕ_g are the phases defining the one dimensional representation of the group we are considering:

$$\tilde{g}|m\rangle = e^{i\phi_{\tilde{g}}}|m\rangle. \tag{A.2}$$

Because the number of elements of this sum depends on m, it is convenient to write the state $|m\rangle$ in a different way:

$$|m\rangle = \frac{1}{\sqrt{B_m}} \sum_g e^{i\phi_g} g|c_m\rangle, \tag{A.3}$$

where the sum is over all the symmetries and

$$\frac{\mu_m}{\sqrt{B_m}} = \frac{1}{\sqrt{A_m}}. \tag{A.4}$$

Using this basis, we can write a generic state as

$$|\Psi\rangle = \sum_m v_m|m\rangle, \tag{A.5}$$

where the normalization condition gives

$$\sum_m |v_m|^2 = 1. \tag{A.6}$$

In order to find the relation between the coefficients v'_m of $|\Psi'\rangle = H|\Psi\rangle$ and the v_m's of $|\Psi\rangle$, we note that

1. By applying the Hamiltonian to $|c_m\rangle$, we obtain states $|c_b\rangle$ which are not necessarily representatives: in the following $|c_n\rangle$ will identify the representative of $|c_b\rangle$

$$H|c_m\rangle = \sum_b h_{m,b} g_{n\to b}|c_n\rangle \ ,$$

   where the sum over b runs over all the configurations but $h_{m,b}$ selects only those configurations connected to $|c_m\rangle$ by a term inthe Hamiltonian.

2. Because g's are symmetries of the Hamiltonian, we have

$$[H, g] = 0 \ .$$

Therefore

$$|\Psi'\rangle = \sum_m v'_m|m\rangle = H|\Psi\rangle = \sum_m \sum_b v_m h_{m,b} \frac{1}{\sqrt{B_m}} \sum_g e^{\phi_g} g g_{n\to b}|c_n\rangle, \tag{A.7}$$

where the index m runs over the equivalence classes, whereas the index b runs over *all* the configuration connected by H to m, but not necessarily belonging to different equivalence classes. Using the group property, it turns out that

$$v'_n = \sum_m \sum_b h_{m,b} \frac{\sqrt{B_n}}{\sqrt{B_m}} e^{-i\phi_{n\to b}} v_m. \tag{A.8}$$

where now the sum over b runs over all the elements of the equivalence class identified by the representative n. The last equation is the basic one to compute the Lanczos step iteration in the reduced basis of states belonging to a given symmetric subspace.

Appendix B

An efficient calculation of the single Lanczos step

In this Appendix we describe an efficient way to find the optimal wavefunction $|\Psi_{\alpha^*}\rangle = (1 + \alpha H)|\Psi\rangle$, starting from a chosen variational state $|\Psi\rangle$, i.e. to calculate the value of α for which the energy

$$E(\alpha) = \frac{\langle\Psi|(1+\alpha H)H(1+\alpha H)|\Psi\rangle}{\langle\Psi|(1+\alpha H)^2|\Psi\rangle} \tag{B.1}$$

has a minimum. The standard method is to calculate the different powers of the Hamiltonian

$$h_n = \frac{\langle\Psi|H^n|\Psi\rangle}{\langle\Psi|\Psi\rangle}, \tag{B.2}$$

using configurations generated by the Metropolis algorithm according to $\Psi^2(x)$.

However, this methods is highly inefficient because smaller statistical fluctuations are obtained if the configurations are generated according to $\Psi^2_{\alpha^*}(x) = (1 + \alpha^* E_x)\Psi(x)$, where E_x is the local energy and α^* is the value of α which minimizes the expectation value (B.1).

Using the definition (B.2), the Eq. (B.1) can be written as

$$E(\alpha) = \frac{h_1 + 2\alpha h_2 + \alpha^2 h_3}{1 + 2\alpha h_1 + \alpha^2 h_2}. \tag{B.3}$$

In order to minimize $E(\alpha)$, it is convenient to compute the energy expectation value h_1 by generating configurations according to $\Psi^2(x)$. Then, instead of calculating h_2 and h_3, we generate configurations distributed according $\Psi^2_\alpha(x)$, with a given α and we compute

$$E(\alpha) = \frac{\langle\Psi_\alpha|H|\Psi_\alpha\rangle}{\langle\Psi_\alpha|\Psi_\alpha\rangle} \tag{B.4}$$

$$\chi(\alpha) = \frac{\langle\Psi_\alpha|(1+\alpha H)^{-1}|\Psi_\alpha\rangle}{\langle\Psi_\alpha|\Psi_\alpha\rangle}. \tag{B.5}$$

$E(\alpha)$ is obtained by averaging over the chosen configurations the local energy E^α_x corresponding to $\Psi_\alpha(x)$, whereas $\chi(\alpha)$ is obtained by averaging over the same configurations the quantity

$(1+\alpha E_x)^{-1}$. Indeed we have that

$$\begin{aligned}\chi(\alpha) &= \frac{\langle\Psi_\alpha|\Psi\rangle}{\langle\Psi_\alpha|\Psi_\alpha\rangle} = \frac{\sum_x |\langle\Psi_\alpha|x\rangle|^2 \frac{\langle x|\Psi\rangle}{\langle x|\Psi_\alpha\rangle}}{\sum_x |\langle\Psi_\alpha|x\rangle|^2} \\ &= \frac{\sum_x |\langle\Psi_\alpha|x\rangle|^2 \left(\frac{1}{1+\alpha E_x}\right)}{\sum_x |\langle\Psi_\alpha|x\rangle|^2}. \end{aligned} \tag{B.6}$$

Given $\chi(\alpha)$, it is straightforward to compute h_2

$$h_2 = \frac{\chi^{-1} - 1 + \alpha h_1(\chi^{-1} - 2)}{\alpha^2}, \tag{B.7}$$

moreover, given h_1 and h_2, the value of $E(\alpha)$ defines the highest momentum h_3

$$h_3 = \frac{E(\alpha)\left(1 + 2\alpha h_1 + \alpha^2 h_2\right) - h_1 - 2\alpha h_2}{\alpha^2}. \tag{B.8}$$

Notice that the most difficult momentum h_3 is given by sampling an energy expectation value, which is much more accurate compared to the direct determination of h_3. Therefore it is possible to minimize $E(\alpha)$, yielding

$$\alpha^* = \frac{-(h_3 - h_1 h_2) \pm \sqrt{(h_3 - h_1 h_2)^2 - 4(h_2 - h_1^2)(h_1 h_3 - h_2^2)}}{2(h_1 h_3 - h_2^2)}, \tag{B.9}$$

where the sign $\pm$ is chosen to minimize the energy $E(\alpha)$. The analytical minimization of $E(\alpha)$, given the value of h_1, $\chi(\alpha)$, and $E(\alpha)$ itself, provides the exact value of α^*, within the statistical errors, which become smaller and smaller whenever $\alpha \sim \alpha^*$. Typically two or three attempts are enough to reach a very accurate determination of α^*.

Appendix C

Variance estimate of the error on bulk correlation functions

In this Appendix we estimate the error on correlation functions assuming that the ground state $|\Phi_0\rangle$ is approximated with the wavefunction $|\Psi_p\rangle$:

$$|\Phi_0\rangle = |\Psi_p\rangle + \epsilon_p|\Psi'\rangle \tag{C.1}$$

where $\langle\Psi_p|\Psi_p\rangle = \langle\Psi'|\Psi'\rangle = 1$, and $|\Psi'\rangle$ represents a normalized wavefunction orthogonal to the exact one, $\langle\Phi_0|\Psi'\rangle = 0$. We restrict our analysis to thermodynamically averaged correlation functions O, the ones which can be written as a bulk average of local operators O_i: $O = \sum_i O_i/L$. This class of operators includes for instance the average kinetic or potential energy or the spin-spin correlation function. If we use periodic boundary conditions the expectation value of O_i on a state with given momentum does not depend on i and the bulk average does not represents an approximation

$$\frac{\langle\Phi_0|O_i|\Phi_0\rangle}{\langle\Phi_0|\Phi_0\rangle} = \frac{\langle\Phi_0|O|\Phi_0\rangle}{\langle\Phi_0|\Phi_0\rangle} = C. \tag{C.2}$$

We show here that the expectation value of bulk-averaged operators O on the approximate state $|\Psi_p\rangle$ satisfy the following relation:

$$\langle\Psi_p|O|\Psi_p\rangle = C + o(\epsilon_p^2, \epsilon_p/\sqrt{L}), \tag{C.3}$$

thus implying that for large enough size the expectation value (C.3) approaches the exact correlation function C linearly with the variance. The validity of the above statement is very simple to show under very general grounds. In fact by definition:

$$\langle\Psi_p|O|\Psi_p\rangle = C - 2\epsilon_p\langle\Psi'|O|\Phi_0\rangle + C\epsilon_p^2 + \epsilon_p^2\langle\Psi'|O|\Psi'\rangle. \tag{C.4}$$

The term proportional to ϵ_p in the above equation can be easily bounded by use of the Schwartz inequality:

$$|\langle\Psi'|O|\Phi_0\rangle|^2 = |\langle\Psi'|(O-C)|\Phi_0\rangle|^2 \leq \langle\Phi_0|(O-C)^2|\Phi_0\rangle. \tag{C.5}$$

The final term in the latter inequality can be estimated under the general assumption that correlation functions

$$C(d) = \frac{\langle \Phi_0 | (O_i - C)(O_{i+d} - C) | \Phi_0 \rangle}{\langle \Phi_0 | \Phi_0 \rangle} \tag{C.6}$$

decay sufficiently fast with the distance $|d|$, as a consequence of the cluster property:

$$\langle \Phi_0 | (O - C)^2 | \Phi_0 \rangle = (1 + \epsilon_p^2) \frac{1}{L} \sum_d C(d). \tag{C.7}$$

This concludes the proof of the statement of this Appendix, provided $\sum_d C(d)$ is finite for $L \to \infty$.

Appendix D

An important property of the projected BCS wavefunction

Let us consider the Gutzwiller projected BCS state

$$|\Psi_{RVB}\rangle = \mathcal{P}_N \mathcal{P} \prod_k \left(u_k + v_k c^\dagger_{k,\uparrow} c^\dagger_{-k,\downarrow} \right) |0\rangle. \tag{D.1}$$

where $\mathcal{P}_N$ projects onto the subspace of N particles, $\mathcal{P}$ is the Gutzwiller projector, which completely forbids doubly occupied sites, and u_k and v_k are variational parameters. The non-projected wavefunction is the exact ground-state solution of the BCS Hamiltonian

$$H = \sum_{k,\sigma} \xi_k c^\dagger_{k,\sigma} c_{k,\sigma} + \sum_k \Delta_k \left(c^\dagger_{k,\uparrow} c^\dagger_{-k,\downarrow} + h.c \right), \tag{D.2}$$

where $\xi_k = -2t\left(\cos k_x + \cos k_y\right) - \mu$, being μ the chemical potential and we assume that Δ_k is real and satisfies $\Delta_k = \Delta_{-k}$. The pair amplitude is given by

$$\frac{v_k}{u_k} = \frac{\Delta_k}{\xi_k + \sqrt{\xi_k^2 + \Delta_k^2}}. \tag{D.3}$$

The effect of particle-hole symmetry

$$d^\dagger_{k,\sigma} = c_{-k+Q,\sigma} \tag{D.4}$$

with $Q = (\pi, \pi)$, leaves the Hamiltonian and the two projectors $\mathcal{P}_N$ and $\mathcal{P}_G$ invariant, but changes the state (D.1) into

$$|\Psi_{RVB}\rangle = \mathcal{P}_N \mathcal{P} \prod_k \left(v_k - u_k d^\dagger_{k+Q,\uparrow} d^\dagger_{-k+Q,\downarrow} \right) |0\rangle \tag{D.5}$$

If the ground-state is invariant under particle-hole transformation, the proportionality between Eq. (D.1) and Eq. (D.5) implies

$$\frac{v_{k+Q}}{u_{k+Q}} = -\frac{u_k}{v_k} \tag{D.6}$$

which corresponds to $\Delta_k = -\Delta_{k+Q}$. However, on a square lattice there are spatial symmetries relating the points k and $k+Q$ *on the Fermi surface*. In particular, the reflections across the bisectors bring k into $k+Q$. Therefore *if the gap is non vanishing along the Fermi surface* Δ_k must change sign under $x \to y$ and $x \to -y$ which means d-wave symmetry.

Now we investigate the signs of the projected wavefunction (D.1) and we show that it satisfies the Marshall sign rule. We start from the BCS Hamiltonian (D.2) and perform the particle-hole transformation only on the down-spins

$$d^\dagger_{k,\downarrow} = c_{-k+Q,\downarrow} \tag{D.7}$$

$$d^\dagger_{k,\uparrow} = c_{k,\uparrow} \tag{D.8}$$

followed by the canonical transformation (spin rotation):

$$a_{k,+} = \frac{1}{\sqrt{2}}(d_{k,\uparrow} + i d_{k,\downarrow}) \tag{D.9}$$

$$a_{k,-} = -\frac{i}{\sqrt{2}}(d_{k,\uparrow} - i d_{k,\downarrow}) \tag{D.10}$$

The BCS Hamiltonian (D.2) acquires the form

$$H = \sum_k \left(h_+(k) + h_-(k)\right) \tag{D.11}$$

where

$$h_\pm(k) = \xi_k a^\dagger_{k,\pm} a_{k,\pm} \mp i\Delta_k a^\dagger_{k,\pm} a_{k+Q,\pm} \tag{D.12}$$

where we have assumed that $\Delta_k = -\Delta_{k+Q}$. The ground-state of H may be written as a tensor product of free states $a_{k,\pm}$ fermions.

If the state $\sum_R \Psi(R_1 \cdots R_N) a_{R_1,+} \cdots a_{R_N,+}|0\rangle$ is the ground-state of $\sum_k h_+(k)$, then the state $\sum_R \Psi^*(R_1 \cdots R_N) a_{R_1,-} \cdots a_{R_N,-}|0\rangle$ is the ground-state of $\sum_k h_-(k)$. Here we have chosen an arbitrary ordering of the lattice sites: $R_1, \cdots, R_N$. Therefore, the ground-state of H is

$$\sum_{R,X} \Psi(R_1 \cdots R_{N/2}) \Psi^*(X_1 \cdots X_{N/2}) a^\dagger_{R_1,+} \cdots a^\dagger_{R_{N/2},+} a^\dagger_{X_1,-} \cdots a^\dagger_{X_{N/2},-}|0\rangle \tag{D.13}$$

where we fixed the chemical potential so to have a ground state with exactly N fermions. If we write this state in terms of the original electron operators we get, apart from a proportionality factor,

$$\sum_{R,X} \Psi(R_1 \cdots R_{N/2}) \Psi^*(X_1 \cdots X_{N/2}) \prod_{m=1}^{N/2} \left[c^\dagger_{R_m,\uparrow} - i(-)^{R_m} c_{R_m,\downarrow}\right]$$
$$\prod_{n=1}^{N/2} \left[c^\dagger_{X_n,\uparrow} + i(-)^{X_n} c_{X_n,\downarrow}\right] c^\dagger_{1,\downarrow} \cdots c^\dagger_{N,\downarrow}|0\rangle \tag{D.14}$$

When we project over the state at fixed number of particles, equal to the number of sites, we must chose the same number of creators and annihilators in the $N/2$ factors of the product. But if we do not want double occupancies (due to the Gutzwiller projector) we must create an up spin on the same site where a down spin has been annihilated. Therefore, the only terms which survive are those with $R_i = X_i$:

$$\sum_R |\Psi(R_1 \cdots R_{N/2})|^2 (-1)^{\sum_j R_j} c^\dagger_{R_1,\uparrow} c_{R_1,\downarrow} \cdots c^\dagger_{R_N,\uparrow} c_{R_N,\downarrow} c^\dagger_{1,\downarrow} \cdots c^\dagger_{N,\downarrow} |0\rangle \tag{D.15}$$

Finally, by moving the down spin creators to the left, we can order the operators according to the specified ordering of sites in the lattice, independently of the spin, without introducing any further phase factor. Therefore, on this basis, the wavefunction has exactly the Marshall sign. In fact the Heisenberg hamiltonian does not move particles thereby leaving invariant the ordering of fermion operators on the lattice.

Bibliography

[1] H. Kamerlingh Onnes, *Leiden Comm.* **120b**, **122b**, **124c** (1911).

[2] J.G. Bednorz and K.A. Müller, Z. Phys. **64**, 189 (1986).

[3] G.M. Eliashberg, Sov. Phys. JETP **11**, 696 (1960).

[4] L.D. Landau, Sov. Phys. JETP **3**, 920 (1957); L.D. Landau, Sov. Phys. JETP **5**, 101 (1957); L.D. Landau, Sov. Phys. JETP **8**, 70 (1959).

[5] C. Castellani, C. Di Castro, and W. Metzner, Phys. Rev. Lett. **72**, 316 (1994).

[6] A.G. Loeser, Z.X. Shen, D.S. Dessau, D.S. Marshall, C.H. Park, P. Fournier, and A. Kapitulnik, Science **273**, 325 (1996).

[7] H. Ding, T. Yokoya, J.C. Campuzano, T. Takahashi, M. Randeria, M.R. Norman, T. Mochiku, K. Kadowaki, and J. Giapintzakis, Nature **382**, 51 (1996).

[8] M.R. Norman, H. Ding, M. Randeria, J.C. Campuzano, T. Yokoya, T. Takeuchi, T. Takahashi, T. Mochiku, K. Kadowaki, P. Guptasarma, and D.G. Hinks, Nature **392**, 1587 (1998).

[9] J.M. Tranquada, B.J. Sternlieb, J.D. Axe, Y. Nakamura, and S. Uchida, Nature **375**, 561 (1995).

[10] K. Yamada, C.H. Lee, Y. Endoh, G. Shirane, R.J. Birgeneau, and M.A. Kastner, Physica C **282-287**, 85 (1997).

[11] P.W. Anderson, Science **235**, 1196 (1987).

[12] J. Hubbard, Proc. R. Soc. London, Ser. A **276**, 238 (1963); M.C. Gutzwiller, Phys. Rev. Lett. **10**, 159 (1963); J. Kanamori, Prog. Theor. Phys. **30**, 275 (1963).

[13] G. Kotliar and A.E. Ruckenstein, Phys. Rev. Lett. **57**, 1362 (1986).

[14] A. Georges, G. Kotliar, W. Krauth, and M.J. Rozenberg, Rev. Mod. Phys. **68**, 13 (1996).

[15] N. Metropolis, A.W. Rosenbluth, M.N. Rosenbluth, A.H. Teller, and E. Teller, J. Chem. Phys. **21** 1087 (1953).

[16] N. Trivedi and D.M. Ceperley, Phys. Rev. B **41**, 4552 (1990).

[17] D.F.B. ten Haaf, H.J.M. van Bemmel, J.M.J. van Leeuwen, W. van Saarloos, and D.M. Ceperley, Phys. Rev. B **51**, 13039 (1995).

[18] S. Sorella, Phys. Rev. Lett. **80**, 4558 (1998).

[19] S. Sorella and L. Capriotti, Phys. Rev. B **61**, 2599 (2000).

[20] W.O. Putikka, M.U. Luchini, and M. Ogata, Phys. Rev. Lett. **69**, 2288 (1992).

[21] W. von der Linden and D.M. Edwards, J. Phys. Cond. Matter **3**, 4917 (1991).

[22] P. Wurth, G. Uhrig, and E. Müller-Hartmann, Ann. Physik **5**, 148 (1996).

[23] T.M. Rice, Physica C **282-287**, xix (1997).

[24] J. Bardeen, L.N. Cooper, and J.R. Schrieffer, Phys. Rev. **108**, 1175 (1957).

[25] For a review on the BCS theory see: J.R. Schrieffer, *Theory of superconductivity*, Benjamin, New York (1964).

[26] M. Randeria and J.C. Campuzano, Cond-mat 9709107.

[27] J.R. Schrieffer, X.G. Wen, and S.C. Zhang, Phys. Rev. B **39**, 11663 (1989).

[28] P. Monthoux, A.V. Balatsky, and D. Pines, Phys. Rev. Lett. **67**, 3448 (1991).

[29] N.E. Bickers, D.J. Scalapino, and S.R. White, Phys. Rev. Lett. **62**, 961 (1989).

[30] V.J. Emery and S.A. Kivelson, Physica C **209**, 597 (1993).

[31] C. Castellani, C. Di Castro, and M. Grilli, Phys. Rev. Lett. **75**, 4650 (1995).

[32] J.D. Jorgensen, B. Dabrowski, S. Pei, D.G. Hinks, L. Soderholm, B. Morosin, J.E. Schirber, E.L. Venturini, and D.S. Ginley, Phys. Rev. B **38**, 11337 (1988).

[33] Y. Nakamura and S. Uchida, Phys. Rev. B **47**, 8369 (1993).

[34] P.W. Anderson and Z. Zou, Phys. Rev. Lett. **60**, 132 (1988); P.W. Anderson, Phys. Rev. Lett. **64**, 1839 (1990).

[35] For a recent review see: T. Timusk and B. Statt, Rep. Prog. Phys. **62**, 61 (1999).

[36] A.R. Moodenbaugh, Y. Xu, M. Suenaga, T.J. Folkerts, and R.N. Shelton, Phys. Rev. B **38**, 4596 (1988).

[37] J.D. Axe, A.H. Moudden, D. Hohlwein, D.E. Cox, K.M. Mohanty, A.R. Moodenbaugh, and Y. Xu, Phys. Rev. Lett. **62**, 2751 (1989).

[38] M.K. Crawford, R.L. Harlow, E.M. McCarron, W.E. Farneth, J.D. Axe, H. Chou, and Q. Huang, Phys. Rev. B **44**, 7749 (1991).

[39] J.M. Tranquada, J.D. Axe, N. Ichikawa, A.R. Moodenbaugh, Y. Nakamura, and S. Ucida, Phys. Rev. Lett. **78**, 338 (1997).

[40] H.A. Mook, P. Dai, S.M. Hayden, G. Aeppli, T.G. Perring, and F. Dogan, Nature **395**, 580 (1998).

[41] H.F. Fong, P. Bourges, Y. Sidis, L.P. Regnault, A. Ivanov, G.D. Gu, N. Koshizuka, and B. Keimer, Nature **398**, 588 (1999).

[42] S. Jin, T.H. Tiefel, M. McCormack, R.A. Fastnacht, R. Ramesh, and L.H. Chen, Science **264**, 413 (1994).

[43] H.W. Kroto, J.R. Heath, S.C. O'Brien, R.F. Curl, and R.E. Smalley, Nature **318**, 162 (1985).

[44] For a review see: *Highly Conducting One-dimensional Solids*, edited by J.T. Devreese, R.P. Evrard, and V.E. van Doren, Plenum Press, New York and London (1979).

[45] E.H. Lieb and F.Y. Wu, Phys. Rev. Lett. **20**, 1445 (1968).

[46] J.E. Hirsch, Phys. Rev. B **31**, 4403 (1985).

[47] S. Zhang, J. Carlson, and J.E. Gubernatis, Phys. Rev. Lett. **78**, 4486 (1997).

[48] M. Guerrero, J.E. Gubernatis, and S. Zhang, Phys. Rev. B **57**, 11980 (1998).

[49] C.J. Halboth and W. Metzner, Phys. Rev. B **61**, 7364 (2000).

[50] For a review on the $t-J$ model see: T.M. Rice, *Strongly Interacting Fermions and High T_c Superconductivity*, Les Houches, edited by B. Doucot and J. Zinn-Justin, Elsevier, North Holland (1991).

[51] F.C. Zhang and T.M. Rice, Phys. Rev. B **37**, 3759 (1988).

[52] F. Mila, Phys. Rev. B **38**, 11358 (1988).

[53] M. Calandra and S. Sorella, Phys. Rev. B **57**, 11446 (1998).

[54] V.J. Emery, S.A. Kivelson, and H.Q. Lin, Phys. Rev. Lett. **64**, 475 (1990).

[55] W.O. Putikka, M.U. Luchini, and T.M. Rice, Phys. Rev. Lett. **68**, 538 (1992).

[56] W.O. Putikka and M.U. Luchini, Phys. Rev. B **62**, 1684 (2000).

[57] M. Kohno, Phys. Rev. B **55**, 1435 (1997).

[58] E.S. Heeb and T.M. Rice, Europhys. Lett. **27**, 673 (1994).

[59] C.T. Shih, Y.C. Chen, and T.K. Lee, Phys. Rev. B **57**, 627 (1998).

[60] M. Calandra, F. Becca, and S. Sorella, Phys. Rev. Lett. **81**, 5185 (1998).

[61] C.S. Hellberg and E. Manousakis, Phys. Rev. Lett. **78**, 4609 (1997).

[62] C.S. Hellberg and E. Manousakis, Phys. Rev. B **61**, 11787 (2000).

[63] S. Rommer, S.R. White, and D.J. Scalapino, Phys. Rev. B **61**, 13424 (2000).

[64] M. Imada and Y. Hatsugai, J. Phys. Soc. Jpn. **58**, 3752 (1989).

[65] M. Imada, J. Phys. Soc. Jpn. **60**, 2740 (1991).

[66] A. Moreo, Phys. Rev. B **45**, 5059 (1992).

[67] E. Dagotto and J. Riera, Phys. Rev. Lett. **70**, 682 (1993).

[68] C. Gros, Phys. Rev. B **38**, 931 (1988).

[69] T. Giamarchi and C. Lhuillier, Phys. Rev. B **43**, 12943 (1991).

[70] Y.C. Chen and T.K. Lee, Phys. Rev. B **51**, 6723 (1995).

[71] C.T. Shih, Y.L. Chen, H.Q. Lin, and T.K. Lee, Phys. Rev. Lett. **81**, 1294 (1998).

[72] M. Calandra and S. Sorella, Phys. Rev. B **61**, 11894 (2000).

[73] S.R. White and D.J. Scalapino, Phys. Rev. B **60**, 753 (1999).

[74] T. Maier, M. Jarrell, T. Pruschke, and J. Keller, Phys. Rev. Lett. **85**, 1524 (2000).

[75] A.I. Lichtenstein and M.I. Katsnelson, Cond-mat 9911320.

[76] T.K. Lee and S. Feng, Phys. Rev. B **38**, 11809 (1988).

[77] R.R.P. Singh and R.L. Glenister, Phys. Rev. B **46**, 11871 (1992).

[78] H.J. Schultz, Phys. Rev. Lett. **64**, 1445 (1990).

[79] N. Furukawa and M. Imada, J. Phys. Soc. Jpn. **61**, 3331 (1992).

[80] Y. Nagaoka, Phys. Rev. **147**, 392 (1966).

[81] X.Y. Zhang, E. Abrahams, and G. Kotliar, Phys. Rev. Lett. **66**, 1236 (1991).

[82] B. Doucot and X.G. Wen, Phys. Rev. B **40**, 2719 (1989).

[83] B. Doucot and R. Rammal, Phys. Rev. B **41**, 9617 (1990).

[84] J.A. Riera and A.P. Young, Phys. Rev. B **40**, 5285 (1989).

[85] F. Becca, A. Parola, and S. Sorella, Phys. Rev. B **61**, 16287 (2000).

[86] D.M. Ceperley and M.H. Kalos, *Monte Carlo Method in Statistical Physics*, edited by K. Binder, Springer-Verlag, Heidelberg (1992).

[87] S. Sorella, Cond-mat 0009149.

[88] A.C. Cosentini, M. Capone, L. Guidoni, and G.B. Bachelet, Phys. Rev. B **58**, 14685 (1998).

[89] F. Becca, M. Capone, and S. Sorella, to be published.

[90] A. Tandon, Z. Wang, and G. Kotliar, Phys. Rev. Lett. **83**, 2046 (1999).

[91] S.R. White and D.J. Scalapino, Phys. Rev. Lett. **80**, 1272 (1998); S.R. White and D.J. Scalapino, Phys. Rev. Lett. **81**, 3227 (1998).

[92] S. Sorella, S. Baroni, R. Car, and M. Parrinello, Europhys. Lett. **8**, 663 (1989).

[93] F. Franjic and S. Sorella, Prog. Theor. Phys. **97**, 399 (1997).

[94] F. Franjic and S. Sorella, Mod. Phys. Lett. B **10**, 873 (1996).

[95] D. Bohm and D. Pines, Phys. Rev. **92**, 609 (1953).

[96] H. Fröhlich, Phys. Rev. **79**, 845 (1950).

[97] L.N. Cooper, Phys. Rev. **104**, 1189 (1956).

[98] W. Weber, Phys. Rev. Lett. **58**, 1371 (1987).

[99] V.J. Emery, S.A. Kivelson, and O. Zachar, Phys. Rev. B **56**, 6120 (1997).

[100] C. Castellani, C. Di Castro, and M. Grilli, Z. Phys. B **103**, 137 (1997).

[101] H.J. Schulz, J. Phys. **50**, 2833 (1989).

[102] D.A. Ivanov, P.A. Lee, and X.G. Wen, Phys. Rev. Lett. **84**, 3958 (2000).

[103] F. Becca, L. Capriotti and S. Sorella, to be published in the Proceedings of Advanced Research Workshop on ”Open Problems in Strongly Correlated Electron Systems”, Bled (2000). Cond-mat 0006353.

[104] J.W. Loram, K.A. Mirza, and P.F. Freeman, Physica C **171**, 243 (1990).

[105] E. Dagotto, private communication.

[106] M. Calandra and S. Sorella, private communication.

[107] F. Bloch, Z. Physik **57**, 545 (1929).

[108] A.W. Overhauser, Phys. Rev. Lett. **4**, 462 (1960).

[109] A. Barbieri, J.A. Riera, and A.P. Young, Phys. Rev. B **41**, 11697 (1990).

[110] M. Ogata and H. Shiba, Phys. Rev. B **41**, 2326 (1990); S. Sorella and A. Parola, J. of Phys. Condens. Matter **4**, 3589 (1992).

[111] M. Ogata, M.U. Luchini, S. Sorella, and F.F. Assaad, Phys. Rev. Lett. **66**, 2388 (1991).

[112] S. Daul, D.J. Scalapino, and S.R. White, Phys. Rev. Lett. **84**, 4188 (2000).

[113] G. Fano, F. Ortolani, and A. Parola, Phys. Rev. B **46**, 1048 (1992).